Directional dark matter search with a low-background gaseous detector

Ikeda, Tomonori

(Degree)
博士（理学）

(Date of Degree)
2020-03-25

(Date of Publication)
2021-03-01

(Resource Type)
doctoral thesis

(Report Number)
甲第7698号

(URL)
https://hdl.handle.net/20.500.14094/D1007698

Doctoral Dissertation

Directional dark matter search with a low-background gaseous detector

(低バックグラウンドガス検出器を用いた方向に感度を持った暗黒物質探索実験)

Tomonori IKEDA

Department of Physics, Graduate School of Science
Kobe University

January, 2020

Abstract

Cosmological observations indicate the existence of dark matter in the universe. In spite of a considerable number of experimental efforts for the direct detection of the dark matter, no experiment has reached a widely agreed discovery. Directional dark matter searches are sensitive to the direction of the nuclear recoils scattering with dark matter. The forward-backward asymmetry of the recoil angular distribution, due to the circular motion of the solar system around the galaxy center, is said to provide strong evidence for the dark matter detection. NEWAGE (NEw generation WIMP search with an Advanced Gaseous tracker Experiment) is one of the directional dark matter search experiments. The low background gaseous tracking detector NEWAGE-0.3b" was developed at Kamioka Observatory in Japan and a directional dark matter search was conducted from June 2018 to November 2018. We obtained a total exposure of 1.1 kg·days and a directional analysis was carried out. No significant excess was found and exclusion limits on Spin-Dependent WIMP-proton cross section with a minimum of 50 pb for 100 GeV/c^2 WIMPs at 90% confidence level was derived. This result marked the best direction-sensitive limit.

Contents

Chapter 1

Introduction

The universe is known to consist of only about 5% ordinary baryonic matter and 70% of dark energy which accelerates the expansion of the universe. The remaining 25% is the so-called dark matter expected to be a particle in new physics beyond the Standard Model. A number of the dark matter candidates have been proposed over the years. Researches aimed at finding them through direct search experiments which observe the scatterings of the dark matter and nuclei, and indirect search experiments which observe the decay and pair annihilation of the dark matter have been carried out. However, the dark matter has not yet been discovered in any way. It is one of the biggest puzzles of the modern cosmology and the particle physics.

In this chapter, we discuss the observational evidence of the dark matter (Section 1.1), its particle nature (Section 1.2) and the WIMP dark matter which is the most promising candidate (Section 1.3). In addition, the principle of the dark matter search is discussed and the event rate is calculated in Section 1.4. Its experimental review is described in Section 1.5. Finally, the NEWAGE experiment is introduced with its history in Section 1.6.

1.1 Observational evidence of dark matter

In the 1930, Fritz Zwicky claimed that the total mass of the Coma cluster would be a hundred times larger than that of optically observable stars in the individual galaxies [1]. When it became possible to measure the rotational velocity of spiral galaxies, it was observed that stars and the hydrogen gas in the galaxy were moving at an almost constant orbital speed despite the different distance from the center of the galaxy [2]. The rotation velocity curves for seven galaxies by Rubin's observation [3] are shown in Figure 1.1.1. Generally, the rotational velocity v at a distance from the center of galaxy r follows Kepler's law and is expected to decrease in outside the center of the galaxy; the rotation velocity is expected to be proportion to $1/\sqrt{r}$. However, the observations showed the constant-velocity distributions. These Results indicate that the contained mass must increase with the radius of the galaxy beyond a few kpc from the galactic center. The total mass is generally considered to be about five times more than the baryon mass which can be optically observed.

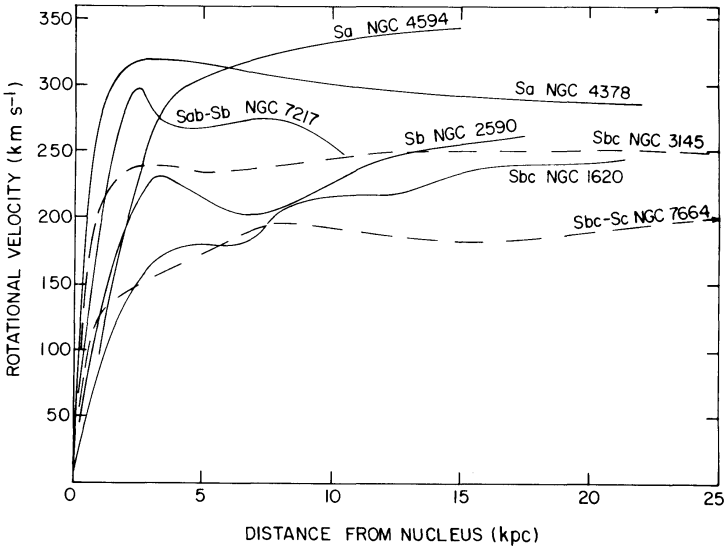

Figure 1.1.1: Rotation velocity curves for seven galaxies. It can be seen that the rotation velocity is constant out to large distance from the galaxy center.
Source: Taken from Rubin et al. [3]

The gravitational lensing effect is a phenomenon in which gravitational fields deflect the light path by a strong gravity source such as an astronomical object. The gravitational lensing effect can be classified into two types: strong gravitational lensing effects and weak gravitational lensing effects. In the strong gravitational lensing effect, the influence of the gravitational source is very strong, and multiple images of a background galaxy are observed. With the weak gravitational lensing effect, it is only possible to statistically detect a background galaxy distortion [4]. The gravitational lensing effect enables to determine the mass distribution and provides that galaxy clusters contain more than five times as much dark matter as baryons such as hot gases.

The most direct evidence of the dark matter in observations using the gravitational lensing effect is the observation of colliding galaxy clusters, "Bullet cluster" [5; 6]. Figure 1.1.2 shows the observation of the bullet cluster IE0657-56 [6]. The most of the mass, reconstructed the joined weak and strong lensing, is located in individual clusters (the green contour map) whereas the intensity distribution of the thermal X-ray emission, observed by Chandra, concentrates in the collision region (the gradation map or the blue cross points). The high temperature plasma gas has the coulomb interaction and cannot pass through the galaxy cluster without resistance while the dark matter is collisionless. This observation indicates that the dark matter components of the two clusters can pass through the galaxy cluster.

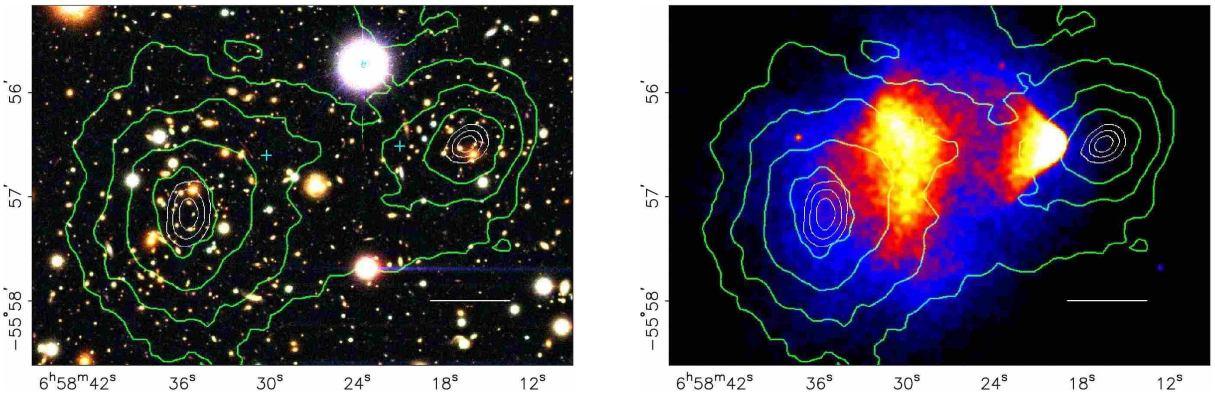

Figure 1.1.2: Observation of the bullet cluster IE0657-56. The green contours show the distribution of individual clusters from the weak lensing. The gradation map shows the intensity distribution of thermal X-ray emission. The blue cross points indicate the location of the center of masses of the plasma clouds.
Source: Taken from D. Clowe et al. [6]

We focus on cosmological scales then one finds that the dark matter played an important role for the growth of the density fluctuations. In the early universe, the number density of photons and matters were large enough in a thermal equilibrium. Therefore, photons and matters exchanged their energy through interactions and photons could not go straight. As the universe expansion, photons and matters lost energy and also the number density decreased. When the temperature dropped to around 3000 K, protons and helium nuclei captured free electrons and matters were not to be in an ionized state and photons were enabled to go straight. This phenomenon is called "recombination". Photons and matters stoped the interaction and the universe was no longer in the thermal equilibrium, while the spectrum of photons remained in the blackbody radiation. The current temperature of remaining photons is 2.725 K. Since the brightness of the blackbody radiation with 2.725 K is maximum at a wavelength of about 2 mm, a measurement with microwaves is required. Thus this blackbody radiation is called "Cosmic Microwave Background (CMB)".

The COBE satellite was launched in 1989 and observed CMB [7]. The COBE discovered that CMB does not have the same temperature in the whole sky and slightly differs depending on the direction. This fluctuation indicated that there had already been a slight inhomogeneity of matters in the early universe. The WMAP satellite was launched in 2001 in order to observe the fluctuations seen by COBE with more sensitivity [8]. In recent years, the Planck satellite have observed CMB [9].

The observed temperature distribution of CMB radiation is uniform; the temperature variation looks the same regardless of the direction. In order to statistically interpret such a distribution, a two-point correlation function was used. The assumption, which there is no special position or direction on the celestial sphere, leads to the fact that the two-point correlation function is only a function of the angle θ between two directions. The spatial distribution of the temperature $T(\theta, \phi)$ is given as a function of the spherical harmonics Y_{lm} by

$$T(\theta, \phi) = \sum_{l=0}^{\infty} \sum_{m=-l}^{l} a_{lm} Y_{lm}(\theta, \phi), \tag{1.1.1}$$

$$C_l = \frac{l}{2l+1} \sum_{m=-l}^{l} |a_{lm}|^2. \tag{1.1.2}$$

Here C_l is called the angular power spectrum and represents the amplitude of the fluctuation at the scale of l $(= \pi/\theta)$. For example, $l = 0$ is the monopole and corresponds to the average temperature and $l = 1$ represents a bipolar anisotropy which divides the celestial sphere into two regions; hot and cold, due to the motion of the earth.

Figure 1.1.3 shows the angular power spectrum observed by the Planck satellite. There are only 6 free parameters in the theoretical curve of the cosmological model to explain the power spectrum. The total mass density of matters determines the first peak height, while the mass density of the ordinary matters contributes to the ratio of the odd and even peak heights. Since the first peak height can not be explained by the mass density of the ordinary matters only, the observed angular spectrum indicated the existence of additional matters which give a gravity potential without interacting photons; the dark matters. The data of the Planck mission yielded the dark matter and the baryonic contents of $\Omega_c h^2 = 0.120 \pm 0.001$ and $\Omega_b h^2 = 0.0224 \pm 0.0001$, respectively [9]. The mass density of dark matters is about five times larger than that of ordinary baryonic matters.

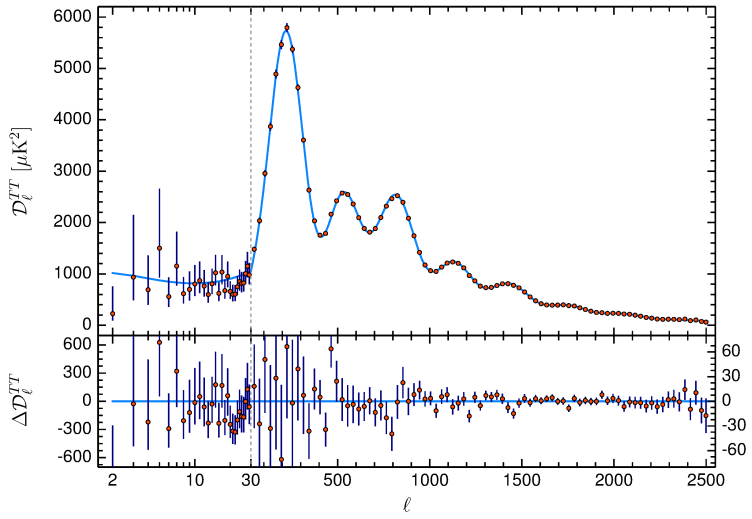

Figure 1.1.3: Planck 2018 temperature power spectrum. The base-ΛCDM theoretical spectrum best fit is plotted with light blue curve in the upper panel. Residuals with respect to this model are shown in the lower panel.
Source: Taken from Planck Collaboration [9]

As mentioned above, astrophysical observations have compelled the evidence of the dark matter and it is one of the funcdations of the standard cosmological model. However, its nature remains unknown. The dark matter is one of the most important problems in modern cosmology and particle physics.

1.2 Particle nature of dark matter

Generally, the dark matter is thought to have been generated during the thermal equilibrium state in the early universe. The relativistic dark matter which preserves the velocity of the recombination time is called HDM (hot dark matter). If the dark matter is relativistic, small-scale structures such as galaxies were hard to be formed because the density fluctuation would have been smeared out. On the other hand, the non-relativistic dark matter is called CDM (cold dark matter) and could have grown small-scale density fluctuations, therefore it could have formed small-scale structures. At present, it is possible to study the structure evolution after the recombination by numerical simulations. These simulations indicate that the structure formation was hierarchical, meaning that small structures such as galaxies formed first and larger structures formed later [10]. Since the observations also strongly favor this scenario, CDM is a favorable candidate.

Non-relativistic and very massive objects, for example planets, brown dwarfs and primordial black holes, are called MACHOs (Massive Compact Objects). They were widely searched by using microlensing and were not found to be the main component of the dark matter because too few of them have been observed [11; 12; 13]. In addition, baryons cannot be the dark matter due to Big Bang Nuclear synthesis and CMB results. Thus they do not have strong interaction. Since the dark matter is not observed optically, they don't have electromagnetic interaction either. Although the possibility of weak interaction remains, the coupling to $W^{\pm}$ and Z gauge boson needs to be smaller than the Standard Model particles, since it has not been found in direct search experiments. From the observations of galaxy cluster collisions like IE0657-56, the dark matter needs to be stable and the self-interactions are rather weak. The upper limit of cross section for self-interaction was calculated by Randall *et al.* [14] and Bradac *et al.* [15]. These constraints are the order of $\sigma_{\mathrm{s}}/m_{\chi} \leq 1\ \mathrm{cm}^2/\mathrm{g}$.

There is no particle satisfying these properties in the Standard Model. Therefore various candidates of the dark matter were proposed as extensions of the Standard Model. Three candidates are discussed in the following.

Lightest Supersymmetric Particle: LSP The supersymmetric (SUSY) model introduces particles called super-partners whose spins are only 1/2 different from their Standard Model counterparts [16]. One of its main motivation was the fact that the radiative corrections of the Higgs mass is canceled and the scale of the electroweak is naturally explained. The lightest SUSY particle, called LSP (the lightest supersymmetric particle), is stable and can be a dark matter candidate. In particular, the super-partners of the neutral electroweak gauge bosons, the photon and Z^0, and of the two neutral Higgs-boson states or linear combinations of these four states are promising WIMP candidates. They are called neutralino.

Axion Axion was introduced as a pseudo-scalar boson in order to solve the CP violation problem of the strong interaction [17]. The axion mass is given in terms of the Peccei-Quinn energy scale f_a by $m_{\mathrm{a}} \sim (10^7\ \mathrm{GeV}/f_a) \times 0.6\ \mathrm{eV}$. Ranges of $10^{-3}\ \mathrm{eV} < m_a < 3\ \mathrm{eV}$ [18] and $10^{-2}\ \mathrm{eV} < m_a < 0.2\ \mathrm{MeV}$ [19; 20] were ruled out by Supernova 1987A and the evolution of red giants, respectively. A lighter mass region remains as the window for the cold dark matter. In spite of the light mass, axions are considered to a dark matter

candidate because they were produced at the phase transition of a vacuum around the inflation era and were not in the thermal equilibrium with other particles in the early universe.

Sterile neutrino There are three kinds of neutrinos ν_e, ν_μ and ν_τ in the Standard Model. The neutrino oscillation was discovered by solar neutrinos, atmospheric neutrinos and the artificial neutrino beams and verified that neutrinos have finite masses and are mixed with themselves [21]. These neutrinos cannot constitute a significant part of the dark matter because they are hot and wash out the density fluctuations observed at scales of many Mpc. However the fourth neutrino named sterile neutrino is proposed as the final state of the neutrino mixing in order to explain the result of LSND experiment. If the mass of the heaviest neutrino state is on the order of the Grand-Unification scale, the mass of active neutrinos can be in the sub-eV mass scale. This concept is called "seesaw mechanism". If the sterile neutrino has a keV mass, it can be the candidate of the warm dark matter [22]. Although the couplings of the sterile neutrinos are too small to have been in thermal equilibrium in the early universe, they can be produced through oscillations with active neutrinos.

1.3 WIMP dark matter

General candidates of the non-baryonic cold dark matter is weakly interacting massive particles (WIMPs). The interest point of WIMPs is that the appropriate abundance of dark matter via self-interaction in chemical equilibrium requires a new particle on the order of 100 GeV mass. Some theories beyond Standard Model of particle physics also predict new particles with similar masses.

In a general model, the WIMPs are generated by pair annihilation of the Standard Model particles in the early universe. An important generation process is the one shown bellow.

$$\chi\bar{\chi} \leftrightarrow e^+e^-,\ \mu^+\mu^-,\ q\bar{q},\ W^+W^-,\ ZZ,\ HH,\ \ldots \tag{1.3.1}$$

When the temperature of the universe was sufficiently larger than the WIMP mass ($T \gg m_\chi$), particle-antiparticle annihilations in the plasma had enough energy to generate the WIMP pairs. In addition, the reverse process also occurs and the annihilation rate is written by,

$$\Gamma_{\rm ann} = \langle\sigma_{\rm ann} v\rangle n_{\rm eq}, \tag{1.3.2}$$

where $\sigma_{\rm ann}$ is the WIMP annihilation cross-section, v is the velocity of the WIMPs and $n_{\rm eq}$ is the number density of the WIMPs in the chemical equilibrium. As the universe expanded, the temperature of the plasma became less than the mass of the dark matter. At this time, although the pair creation of WIMPs continued, these particles and antiparticles, sufficient kinetic energy to generate dark matter, were only the higher tail part of the Boltzmann distribution; the WIMP production decreased exponentially $e^{-m_\chi/T}$. At the same time, since the expansion of the universe decreased the number density of the particles, the WIMP production rate decreased in proportion to the number density. When the production rate fell below the expansion rate of the universe (the mean free path to create WIMPs was longer than Hubble radius), the WIMP production stoped. This process is called "freeze-out". After this, the number density of the WIMPs has

been approximately constant in a comoving volume. The current amount of WIMPs is approximately expressed by,

$$\Omega_\chi h^2 \simeq 0.1 \times \left(\frac{10^{-9}\ \mathrm{GeV}^{-2}}{\langle \sigma v \rangle} \right). \tag{1.3.3}$$

Typical annihilation cross section is given by

$$\langle \sigma v \rangle \sim \frac{\pi \alpha^2}{m_\chi^2}. \tag{1.3.4}$$

In order to explain the observed dark matter density, the WIMP mass should be typically 100 GeV $\leq m_\chi \leq$ 1000 GeV with the mass scale of the electroweak interaction. These properties are corresponding to a new particle produced by theories beyond Standard Model such as the SUSY model.

So far, we discussed the WIMP model from a theoretical point of view. In addition, the WIMP is a good candidate from the experimental aspect, since we can detect by using three search methods, direct, indirect and collider searches. Figure 1.3.1 shows the diagram of these WIMP searches. The direct search seeks for the WIMP-nucleus elastic scatterings, and is expected to provide the direct evidence of the dark matter. Indirect searches are to find the evidence of WIMPs by detecting gamma-rays, neutrinos and anti-particles emitted from the annihilation of WIMPs. The collider experiment aims to produce WIMPs directly by the collision of accelerated particles. These three methods are complement to the others and have an advantage to test the WIMP hypothesis. In this paper, we discuss the direct dark matter search for WIMPs.

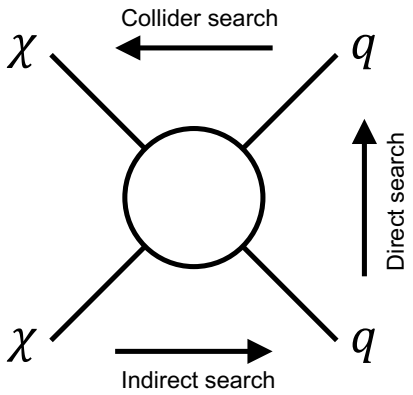

Figure 1.3.1: Diagram of the direct, indirect and collider WIMP searches. The symbol of χ and q represent WIMPs and quarks, respectively.

1.4 Principle of direct dark matter search

In the direct dark matter search, recoil nuclei by a scattering of the dark matter in the Milky Way galaxy halo are observed by a detector on the Earth. Since it is a very rare event, experiments are performed in underground sites such as Gran Sasso in Italy,

Sudbury in Canada, and Kamioka in Japan in order to reduce cosmic ray backgrounds. The nuclear recoil energy is converted into light, heat or charge and detected. Recently, the mainstream method is to detect more than two of these three signals simultaneously in order to distinguish electron recoil backgrounds from nuclear recoil events. In addition, if the reaction position in the detector can be specified, only the volume with less backgrounds (fiducial volume) can be used for the analysis. Thus the detection sensitivity of the dark matter depends on the detector design.

In the direct search, the annual modulation and the directional signature were advocated. The annual modulation is due to the orbital motion of the Earth around the Sun. On the other hand, the directional signature is due to the circular motion of the solar system around the galaxy center. The forward-backward asymmetry in recoil angular distribution enables to distinguish the dark matter signals from isotropic background signals. Therefore the directional signals is said to provide a smoking gun signature. In this section, these dark matter signatures are discussed.

In Section 1.4.1, we calculate the expected event rate of the recoil nucleus scattering with dark matter. In Section 1.4.2, we introduce the WIMP-nucleus cross section which depends on the particle physics model. In Section 1.4.3, the nuclear form factor which depends on the nuclear physics is discussed. In Section 1.4.4, the expected energy spectrum of the ^{19}F nucleus is calculated. In Section 1.4.5, we describe the annual-modulation signature. Finally, the directional signature is derived in Section 1.4.6.

1.4.1 Event rate

A target nucleus is elastically scattered off by the dark matter and the recoil energy and momentum are detected. The expected energy spectrum can be calculated by considering the motion of the Earth and the dark matter in the galaxy. It is discussed in Refs [23; 24]. The Sun is orbiting the galactic center and traveling toward the constellation Cygnus. If the WIMP distribution is in the thermal equilibrium, the solar speed and the velocity dispersion of WIMP are expected to be in the similar magnitude. Hence the WIMP flux is enhanced in the direction of the solar motion.

We assume that the WIMP velocity distribution has the Standard Halo Model (SHM) where and isotropic Milky Way (MW) halo is assumed. In this simple model, the velocity distribution $f_{\rm gal}(\boldsymbol{v})$ in the rest frame of the galaxy takes the form of a Maxwellian distribution,

$$f_{\rm gal}(\boldsymbol{v}) = \begin{cases} \frac{1}{N_{\rm esc}(2\pi\sigma_v^2)^{3/2}} \exp\left[-\frac{|\boldsymbol{v}|^2}{2\sigma_v^2}\right] , & |\boldsymbol{v}| < v_{\rm esc} \\ 0 , & |\boldsymbol{v}| > v_{\rm esc} \end{cases} \tag{1.4.1}$$

where $N_{\rm esc}$ is normalization factor, σ_v is the velocity dispersion and $v_{\rm esc}$ is the local escape velocity. In the SHM, the velocity dispersion $v_{\rm esc}$ is independent of the distance from the galactic center and related to the local circular velocity v_c, via $\sigma_v = v_c/\sqrt{2}$. The canonical value of the local circular velocity v_c is 220 kms^{-1} [25]. Since it depends on the model of the MW halo, it has a significant systematic uncertainty. For instance, various models of MW halo indicate the local circular velocity from (220 ± 20) km s^{-1} to (279 ± 33) km s^{-1} [26]. Recently the RAVE survey has found the escape velocity to be $v_{esc} = 533^{+54}_{-41}$ km s^{-1}(90% confidence level) assuming a smooth halo in equilibrium [27]. However the canonical value of $v_{esc} = 650$ km s^{-1} is often used in order to compare results

of various direct detection calculations.

The local WIMP density $\rho_{\rm DM}$ is also an important parameter to calculate the nuclear recoil spectrum. The canonical value $\rho_{\rm DM} = 0.3$ GeV cm^{-3} is used in most of the direct detection calculations. The calculation of the local WIMP density also depends on the halo profile model. Recent analyses leads to the local densities in the range of $\rho_{\rm DM} = (0.2 - 0.5)$ GeV cm^{-3} [28; 29; 30; 31].

Let us consider an elastic collision between the WIMP and a nucleus (Figure 1.4.1). The WIMP and nuclear masses are represented by m_χ and $m_{\rm A}$, respectively. The WIMP velocity in the laboratory rest frame is expressed as $\boldsymbol{v}$ and the initial velocity of the nucleus is negligible. The nuclear recoil with momentum $\boldsymbol{q}$ and energy E_q are given by the non-relativistic expression,

$$q = 2\mu v \cos\theta, \tag{1.4.2}$$

$$E_q = 2v^2 \frac{\mu^2}{m_{\rm A}} \cos^2\theta, \tag{1.4.3}$$

where

$$\mu = \frac{m_\chi m_{\rm A}}{m_\chi + m_{\rm A}}, \tag{1.4.4}$$

is the WIMP-nucleus reduced mass. The angle between the initial WIMP velocity $\hat{\boldsymbol{v}}$[1] and the direction of the nuclear recoil $\hat{\boldsymbol{q}}$ is denoted by θ.

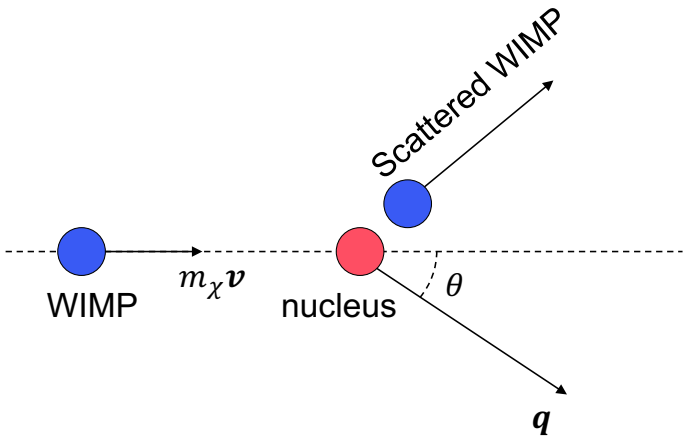

Figure 1.4.1: Scheme of the kinematics of the elastic collision between a WIMP and a nucleus.

We define the double differential event rate with respect to the nuclear recoil energy E_q and the nuclear recoil direction $\hat{\boldsymbol{q}}$ as

$$\frac{\mathrm{dR}}{dE_q d\Omega_q}, \tag{1.4.5}$$

[1]The hat symbol indicates a unit vector.

where Ω_q denotes solid angle around the direction $\hat{\boldsymbol{q}}$. The differential WIMP-nucleus scattering cross section is written by,

$$\frac{d\sigma}{dq^2} = \frac{\sigma_{\chi-\mathrm{N}}}{4\mu^2 v^2} S(q), \tag{1.4.6}$$

where $\sigma_{\chi-\mathrm{N}}$ is the total scattering cross section of the WIMP-nucleus with a point-like nucleus, $S(q) = |F(q)|^2$ is a nuclear form factor and $dq^2 = 2m_A dE_q$. The total scattering cross section $\sigma_{\chi-\mathrm{N}}$ depends on the particle physics model and the detail expression is described in Section 1.4.2. On the other hand, the nuclear form factor $S(q)$ depends on the nuclear physics and the the detail expression is described in Section 1.4.3.

The double differential cross section is defined as

$$\frac{d\sigma}{dq^2 d\Omega_q}. \tag{1.4.7}$$

Azimuthal symmetry of the scattering around the WIMP arrival direction gives $d\Omega_q = 2\pi d\cos\theta$. The relation between $\cos\theta$ and q in Equation 1.4.2 can be imposed through a Dirac δ function, $\delta(\cos\theta - q/2\mu v)$. Thus

$$\frac{d\sigma}{dq^2 d\Omega_q} = \frac{d\sigma}{dq^2}\frac{1}{2\pi}\delta\left(\cos\theta - \frac{q}{2\mu v}\right) = \frac{\sigma_{\chi-\mathrm{N}} S(q)}{8\pi\mu^2 v}\delta(\boldsymbol{v}\cdot\hat{\boldsymbol{q}} - v_{\min}), \tag{1.4.8}$$

where

$$v_{\min} = \sqrt{E_q m_{\mathrm{A}}/2\mu^2}, \tag{1.4.9}$$

is the minimum WIMP velocity required to produce a recoil of energy E_q in an elastic scattering.

The flux of WIMPs with velocity v in the velocity space element d^3v is defined as

$$\frac{\rho_{\mathrm{DM}}}{m_\chi} v f(\boldsymbol{v}) d^3 v, \tag{1.4.10}$$

where $f(\boldsymbol{v})$ is the WIMP velocity distribution in the laboratory frame.

Summarizing these equations, the double differential event rate per unit time per unit target mass is written using the number of nuclei in the detector N_A as

$$\frac{dR}{dE d\Omega_q} = \frac{N_{\mathrm{A}}}{m_{\mathrm{A}} N_{\mathrm{A}}}\int 2m_{\mathrm{A}}\frac{d\sigma}{dq^2 d\Omega_q}\frac{\rho_{\mathrm{DM}}}{m_\chi} v f(v) d^3 v = \frac{\rho_{\mathrm{DM}}\sigma_{\chi-\mathrm{N}} S(q)}{4\pi m_\chi \mu^2}\int \delta(\boldsymbol{v}\cdot\hat{\boldsymbol{q}} - v_{\min}) f(v) d^3 v. \tag{1.4.11}$$

In addition, we introduce the three-dimensional Radon transform of the WIMP velocity distribution $f(\boldsymbol{v})$ given by

$$\hat{f}(v_{\min}, \hat{\boldsymbol{q}}) = \int \delta(\boldsymbol{v}\cdot\hat{\boldsymbol{q}} - v_{\min}) f(\boldsymbol{v}) d^3 v. \tag{1.4.12}$$

Geometrically, $\hat{f}(v_{\min}, \hat{\boldsymbol{q}})$ is the integral of the function $f(\boldsymbol{v})$ on a plane orthogonal to the direction $\hat{\boldsymbol{q}}$ at a distance q from the origin. Especially the radon transform in the laboratory frame for the truncated Maxwellian WIMP velocity distribution is written

by [32]

$$\hat{f}(v_{\rm min},\hat{\boldsymbol{q}}) = \begin{cases} \frac{1}{N_{\rm esc}(2\pi\sigma_v^2)^{1/2}}\left\{\exp\left[-\frac{(v_{\rm min}+\hat{\boldsymbol{q}}\cdot\boldsymbol{V}_{\rm lab})^2}{2\sigma_v^2}\right]-\exp\left[-\frac{v_{\rm esc}^2}{2\sigma_v^2}\right]\right\}, & v_{\rm min}+\hat{\boldsymbol{r}}\cdot\boldsymbol{V}_{\rm lab} < v_{\rm esc} \\ 0\ , & v_{\rm min}+\hat{\boldsymbol{r}}\cdot\boldsymbol{V}_{\rm lab} > v_{\rm esc} \end{cases} \tag{1.4.13}$$

where $\boldsymbol{V}_{\rm lab}$ is the velocity of the laboratory with respect to the Galaxy and $N_{\rm esc}$ is a normalized factor defined as

$$N_{\rm esc} = {\rm erf}\left(\frac{v_{\rm esc}}{\sqrt{2}\sigma_v}\right) - \sqrt{\frac{2}{\pi}}\frac{v_{\rm esc}}{\sigma_v}\exp\left[-\frac{v_{\rm esc}^2}{2\sigma_v^2}\right]. \tag{1.4.14}$$

Finally, Equation 1.4.11 can be rewritten as

$$\frac{dR}{dE\,d\Omega_q} = \frac{\rho_{\rm DM}\sigma_{\chi-{\rm N}}S(q)}{4\pi m_\chi \mu^2}\hat{f}(v_{\rm min},\hat{\boldsymbol{q}}). \tag{1.4.15}$$

The expected event rate is derived by inputs from the total scattering cross section of the WIMP-nucleus $\sigma_{\chi-N}$ and the nuclear form factor $S(q)$. Detailed expressions will be discussed in the following sections.

1.4.2 Cross section

The WIMP-nucleus cross section depends on the particle physics model. The cross section can be calculated by assuming certain sets of parameters in the MSSM model [16; 33]. The Spin-Independent (SI) cross section is written as

$$\sigma^{\rm SI}_{\chi-{\rm N}} = \frac{4\mu^2}{\pi}[Zf_{\rm p} + (A-Z)f_{\rm n}]^2, \tag{1.4.16}$$

where Z and A are the atomic number and the mass number of a target, respectively. The $f_{\rm p}$ and $f_{\rm n}$ are the WIMP-proton and WIMP-neutron SI coupling constant and often considered to be equal, with an assumption that scattering on sea quarks dominates. Thus the SI cross section is written in terms of the WIMP-proton SI cross section $\sigma^{\rm SI}_{\chi-{\rm p}}$ by,

$$\sigma^{\rm SI}_{\chi-{\rm N}} = \sigma^{\rm SI}_{\chi-{\rm p}}\frac{\mu^2}{\mu^2_{\chi-{\rm p}}}A^2. \tag{1.4.17}$$

Equation 1.4.17 indicates that a heavy target is effective for SI interaction due to the enhancement of A^2.

The Spin-Dependent (SD) cross section is given by,

$$\sigma^{\rm SD}_{\chi-{\rm N}} = \frac{32}{\pi}G_{\rm F}^2\mu^2\frac{J+1}{J}[a_{\rm p}\langle S_{\rm p}\rangle + a_{\rm n}\langle S_{\rm n}\rangle]^2, \tag{1.4.18}$$

where $G_{\rm F}$ is the Fermi coupling constant, $\langle S_{\rm p}\rangle$ and $\langle S_{\rm n}\rangle$ are the spin content of the proton and neutron and J is the total spin of the nucleus. The $a_{\rm p}$ and $a_{\rm n}$ are the WIMP-proton and -neutron SD coupling constants. The SD interaction can only occur for nuclei with an odd number of either protons or neutrons. The SD cross section is rewritten in terms

of the WIMP-proton SD cross section $\sigma^{\rm SD}_{\chi-{\rm p}}$ by,

$$\sigma^{\rm SD}_{\chi-{\rm N}} = \sigma^{\rm SD}_{\chi-{\rm p}} \frac{\mu^2}{\mu^2_{\chi-p}} \frac{\lambda^2 J(J+1)}{0.75}. \tag{1.4.19}$$

The value of $\lambda^2 J(J+1)$ depends on the nucleus. The calculated values for various nuclei are described in Ref [23] and listed in Table 1.4.1. The DM experiments using various target nuclei are compared with the WIMP-proton (or neutron) cross section $\sigma^{\rm SI}_{\chi-{\rm p}}$ and $\sigma^{\rm SD}_{\chi-{\rm p}}$. It requires model-dependent assumptions or a dedicated framework.

Table 1.4.1: Total spin, the natural abundance, the calculated $\lambda^2 J(J+1)$ and the unpaired nucleon of various nuclear targets.

Isotope	J	Abundance(%)	$\lambda^2 J(J+1)$	Unpaired nucleon
^{1}H	1/2	100	0.750	proton
^{7}Li	3/2	92.5	0.244	proton
^{11}B	3/2	80.1	0.112	proton
^{15}N	1/2	0.4	0.087	proton
^{19}F	1/2	100	0.647	proton
^{23}Na	3/2	100	0.041	proton
^{127}I	5/2	100	0.007	proton
^{133}Cs	7/2	100	0.052	proton
^{3}He	1/2	1.0×10^{-4}	0.928	neutron
^{17}O	5/2	0.0	0.342	neutron
^{29}Si	1/2	4.7	0.063	neutron
^{73}Ge	9/2	7.8	0.065	neutron
^{129}Xe	1/2	26.4	0.124	neutron
^{131}Xe	3/2	21.2	0.055	neutron
^{183}W	1/2	14.3	0.003	neutron

1.4.3 Nuclear form factor

The nuclear form factor depends on the nuclear physics. It is introduced to account for the spatial extent of the nuclear. When the de Broglie wavelength h/q with the momentum transfer q ($= \sqrt{2m_A E_q}$) is no longer large compared to the nuclear radius, the effective cross section begins to fall. This effect is strong for a heavy nuclear or a heavy WIMP. In the first Born (plane wave) approximation, the form factor is given by Fourier

transformation of the density distribution of the scattering center, $\rho(r)$, by [23]

$$\begin{aligned} F(qr_{\mathrm{n}}) &= \int \rho(r)\exp(i\mathbf{q}\cdot\mathbf{r})\mathbf{dr} \\ &= \frac{4\pi}{q}\int_0^\infty r\sin(qr)\rho(r)dr. \end{aligned}$$

In the SI interaction, since WIMP would interact with any of the nucleon, the nuclei can be approximated as a solid sphere. In this case, the nuclear form factor is written using the Bessel function $j_1(x) = (\sin x - x\cos x)/x^2$ by

$$F(qr_{\mathrm{n}}) = 3\frac{j_1(qr_{\mathrm{n}})}{qr_{\mathrm{n}}}\exp\left(-\frac{(qs)^2}{2}\right), \tag{1.4.20}$$

where $r_{\mathrm{n}} \simeq 1.14A^{1/3}$ fm is an effective nuclear radius and $s \simeq 0.9$ fm is the nuclear skin thickness.

In the SD interaction, since WIMP would interact with the surplus nucleon, the nuclei can be approximated as thin shell, and this assumption is called the odd-group model. In this case, the form factor is written using Bessel function $j_0 = \sin x/x$ by

$$F(qr_{\mathrm{n}}) = j_0(qr_{\mathrm{n}}), \tag{1.4.21}$$

where $r_{\mathrm{n}} \simeq 1.0A^{1/3}$ fm. There are several evaluations of the nuclear form factor such as the Helm form factor [34] or Hartree-Fock calculations [35], but the differences are small. The calculated nuclear form factors are shown in Figure 1.4.2.

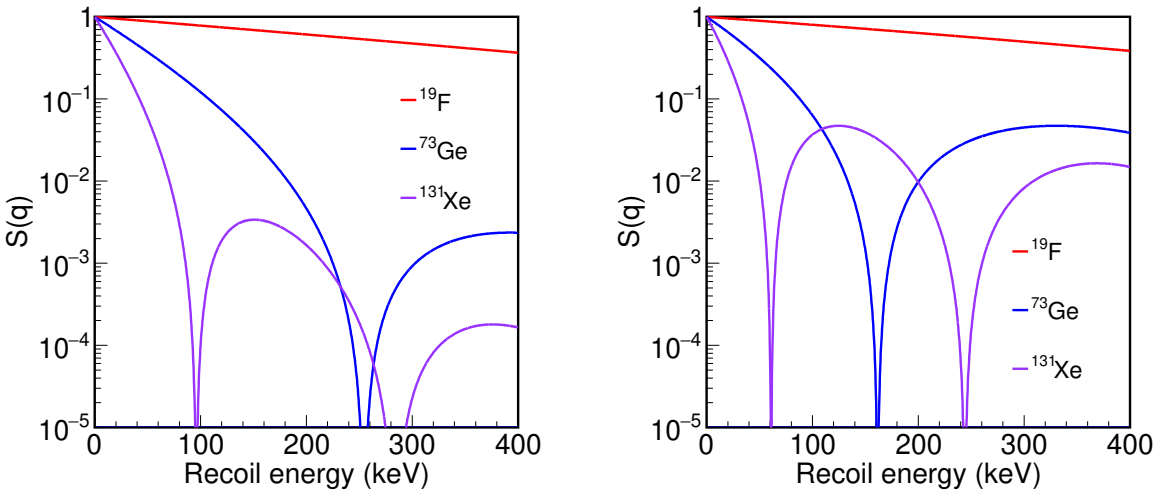

(a) Spin-Independent form factors.

(b) Spin-Dependent form factors.

Figure 1.4.2: Spin-Independent (a) and Spin-Dependent (b) nuclear form factor of several isotopes as a function of the recoil energy. The red, blue and purple lines show the target isotopes of ^{19}F, ^{73}Ge and ^{131}Xe, respectively.

1.4.4 Energy spectrum

The expected energy spectrum of a nucleus is obtained by integrating the solid angle of Equation 1.4.15. Here we assume the target nucleus as ^{19}F. The Spin-Dependent cross section $\sigma^{\mathrm{SD}}_{\chi-N}$ is obtained from Equation 1.4.19. The nuclear form factor $S(q)$ of the Spin-Dependent interaction is obtained from Equation 1.4.21 and described in Figure 1.4.2b. We input these parameters into Equation 1.4.15 and obtained the expected energy spectrum where the WIMP mass is 50, 100 or 200 GeV/c^2 and the WIMP-proton SD cross section $\sigma^{\mathrm{SD}}_{\chi-\mathrm{p}}$ is 1 pb. The calculated energy spectra are shown in Figure 1.4.3. When the dark matter mass is heavier (or the target mass is lighter), the high energy recoil events increase because of the large momentum transfer.

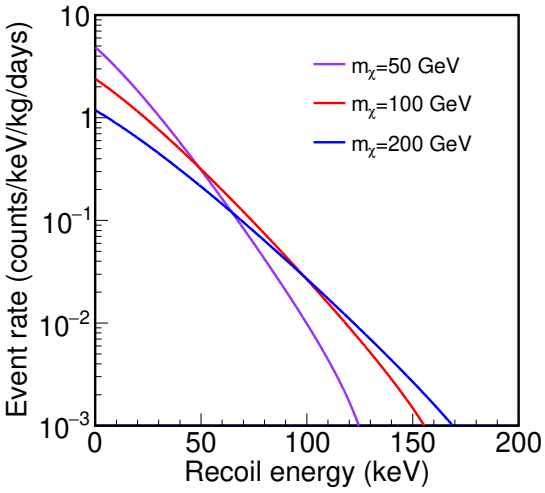

Figure 1.4.3: Expected energy spectra for the ^{19}F nucleus. The WIMP mass of m_χ =50, 100 or 200 GeV and the WIMP-proton SD cross section of $\sigma^{\mathrm{SD}}_{\chi-p}$ = 1 pb are assumed.

1.4.5 Direct searches with conventional detectors

The Earth's velocity V_{lab} with respect to the galaxy modulates annually because of the orbital motion around the Sun. Hence the WIMP velocity distribution in the laboratory frame and the event rate also modulate. This signature is called "annual modulation". The velocity of the Earth become maximum in June 2nd and minimum in December 4th. Using the similar method in Section 1.4.4 with $V^{\mathrm{Jun}}_{\mathrm{lab}}$ and $V^{\mathrm{Dec}}_{\mathrm{lab}}$, the expected energy spectrums of each season were calculated where the target nucleus of ^{19}F, the WIMP-proton SD cross section of $\sigma^{\mathrm{SD}}_{\chi-p}$ = 1 pb and the WIMP mass of m_χ = 100 GeV are assumed. The obtained energy spectra are shown in Figure 1.4.4. The order of modulation is $O(v_{\mathrm{orb}}/v_{\mathrm{sun}}) \sim 5\%$.

1.4.6 Direct searches with directional detectors

The directional signature is due to the circular motion of the solar system around the galaxy center. Since the constellation Cygnus is in the forward direction of the solar

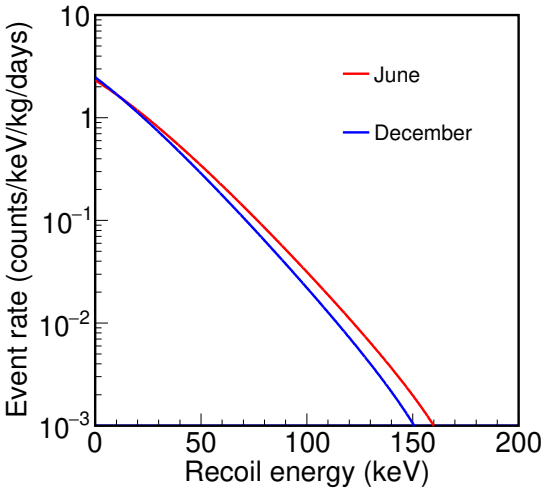

Figure 1.4.4: Difference of the energy spectra between June and December, where the target is ^{19}F for the SD interaction, $m_\chi = 100$ GeV, and $\sigma^{\mathrm{SD}}_{\chi-\mathrm{p}} = 1$ pb

system's motion, WIMPs would seem to be coming from the direction of the constellation Cygnus. Hence the nuclear recoil distribution is biased in the opposite direction of the constellation Cygnus. This dipole signature was first described by Spergel [36], who indicated that the event rate ratio of the forward to backward direction could be an order of 10. Moreover since the Cygnus direction is varying per hour and per day in the laboratory frame, this signature is easily discriminated from environmental backgrounds.

Integrating the azimuth angle of the recoil nucleus, the double differential event rate of Equation 1.4.15 is rewritten by

$$\frac{dR}{dE\,d\cos\theta} = \frac{\rho_{\mathrm{DM}}\sigma_{\chi-\mathrm{N}}S(q)}{2m_\chi\mu^2}\hat{f}(v_{\mathrm{min}},\hat{\boldsymbol{q}}). \tag{1.4.22}$$

Here we assume that the target nucleus is ^{19}F, the Spin-Dependent cross section is $\sigma^{\mathrm{SD}}_{\chi-\mathrm{p}} = 1$ pb and WIMP mass is $m_\chi = 100$ GeV. The cosθ-energy distribution is derived by substituting Equation 1.4.19 and 1.4.21 into Equation 1.4.22. The expected distribution is shown in Figure 1.4.5. Since a detector has an energy threshold, often we focus on an certain energy region. We obtained the expected angular distribution in the energy region of 50 keV $\leq E \leq$ 60 keV by extracting from Figure 1.4.5. The angular distribution is shown in Figure 1.4.6a. In the case of not recognizing the head-tail of the nuclear track, the absolute angular distribution is also calculated and shown in Figure 1.4.6b.

The expected ratio of the forward ($0.0 \leq \cos\theta \leq 0.5$) to the backward ($0.5 \leq \cos\theta \leq 1.0$) is about 4.0. This forward-backward ratio is about 100 times greater than the annual modulation. Hence the directional signal provides a strong evidence for the dark matter.

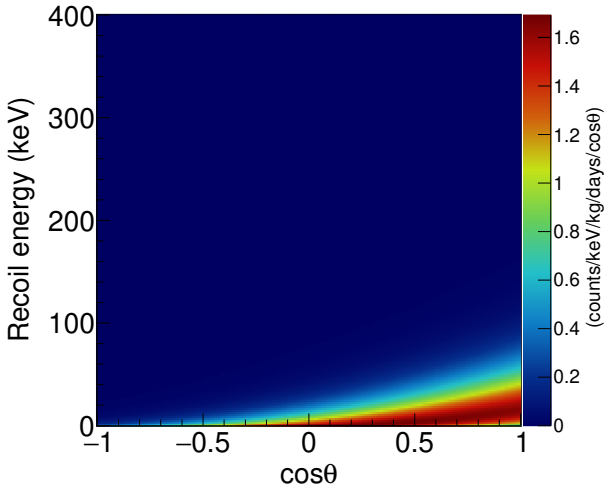

Figure 1.4.5: Expected cosθ-energy distribution where the target ^{19}F for the SD interaction, the SD cross section of $\sigma^{\mathrm{SD}}_{\chi-\mathrm{p}} = 1$ pb and WIMP mass of $m_\chi = 100$ GeV are assumed. The θ is defined as the angle between the direction of the constellation Cygnus and the nuclear recoil.

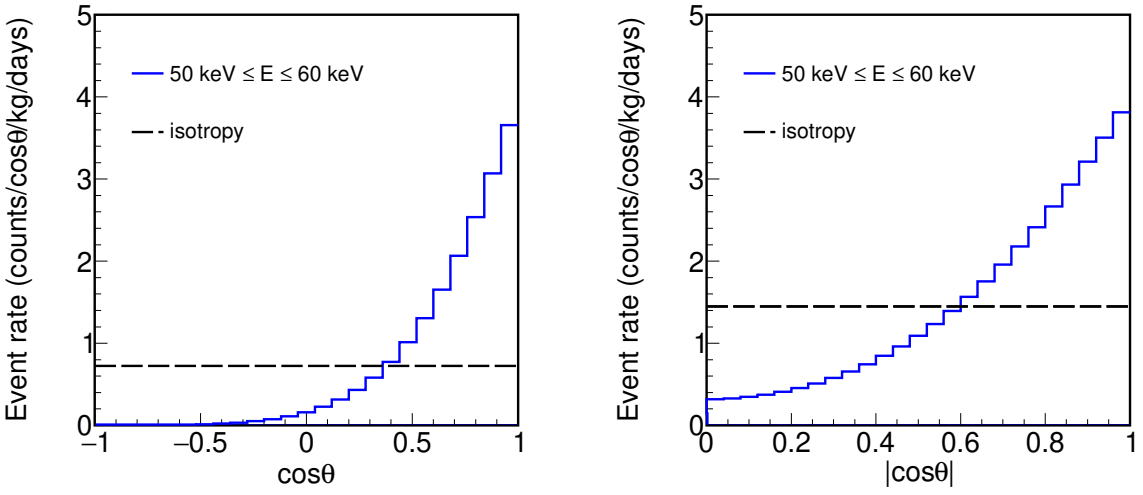

(a) cosθ (b) absolute cosθ

Figure 1.4.6: Angular distributions in energy range of $50 \leq E \leq 60$ keV, where the target ^{19}F for the SD interaction, the SD cross section of $\sigma^{\mathrm{SD}}_{\chi-\mathrm{p}} = 1$ pb and WIMP mass of $m_\chi = 100$ GeV are assumed. The θ is defined as the angle between the direction of the constellation Cygnus and the nuclear recoil. Two cases where head-tail of nuclear track can be recognized (a) or not (b) are calculated. Isotropic backgrounds are drawn in same figure with the black dashed lines.

1.5 Review of direct search experiments

1.5.1 Annual modulation searches

Experiments aiming at observing annual modulation in the past or present are summarized in Table 1.5.1. Currently, DAMA/LIBRA experiment using NaI scintillator crystal claims the evidence of the dark matter. An annual modulation in the energy region of 2-6 keV with a total exposure of 2.46 ton·yr was observed with a 12.9 σ confidence level. The modulation amplitude and the period are (0.0103 ± 0.0008) cpd/kg/keV and (0.999 ± 0.001) yr, respectively. However other direct detection searches did not find such signal claimed DAMA/LIBRA in spite of sufficient sensitivities and set exclusion limits on the SI dark matter-nucleus cross section. Exclusion limits of SI cross section are shown in Fig 1.5.1. In order to solve this tension, several experiments with the same target material as DAMA/LIBRA, NaI, are planned as COSINE [37] in Yangyang, PICO-LON [38] in Japan, SABRE [39] in Italy and Australia, and ANAIS [40] in Spain. First result of COSINE-100 [37] and ANAIS-112 [40; 41] testing an annual modulation did not lead to either a discovery or a rejection with a sufficient statistical significance.

Table 1.5.1: Direct dark matter search experiments

Experiments	Detector	Target materials	Signals
DAMA/LIBRA(NaI) [42]	Solid scintillator	NaI	light
COSINE [37]	Solid scintillator	NaI	light
PICO-LON [38]	Solid scintillator	NaI	light
SABRE [39]	Solid scintillator	NaI	light
ANAIS [40]	Solid scintillator	NaI	light
SuperCDMS [43; 44]	Bolometer	Si and Ge	phonon and charge
CoGeNT [45]	Bolometer	Ge	phonon and charge
EDELWEISS [46]	Bolometer	Ge	phonon and charge
CRESST [47]	Bolometer	$CaWO_4$	phonon and light
DEAP-3600 [48]	Single-phase liquid scintillator	Ar	light
DarkSide [49]	Dual-phase liquid scintillator	Ar	light and charge
XMASS [50]	Single-phase liquid scintillator	Xe	light
XENON1T [51]	Dual-phase liquid scintillator	Xe	light and charge
LUX [52]	Dual-phase liquid scintillator	Xe	light and charge
PANDAX-II [53]	Dual-phase liquid scintillator	Xe	light and charge
XENONnT	Dual-phase liquid scintillator	Xe	light and charge
LZ [54]	Dual-phase liquid scintillator	Xe	light and charge

Experiments using a dual-phase liquid xenon detector (LXe), XENON1T [51], LUX [52] and PANDAX-II [53], obtained the highest sensitivity (Figure 1.5.1). Liquid xenon is good detection medium for the SI cross section; large atomic number, high density and high radio purity. In addition, liquid xenon has high stopping power for ambient radiations and makes a good self shielding. The dual-phase detector detects not only the prompt scintillation light but also the ionization signal. The ionized electrons drift upwards to the xenon gas phase above the liquid and a secondary scintillation light is yielded by the

strong electric field. The ionization signal is obtained as the secondary scintillation signal. The ratio of the ionization signal and the prompt scintillation signal provides a powerful electron discrimination. Also the difference of detection time between them provides the interaction site. These advantages dramatically improved the sensitivities.

In the low mass range below 10 GeV, experiments using bolometers, CRESST [47], SuperCDMS [43; 44], have shown sensitivities. The deposit energy on the detector is converted to not only ionization or light but also heat. The heat capacity of a dielectric crystal is proportional to temperature to the third power T^3 at the low temperature. Thus the bolometer enables to measure at the smaller energy deposition of a nuclear recoil and decrease the energy threshold of a detector.

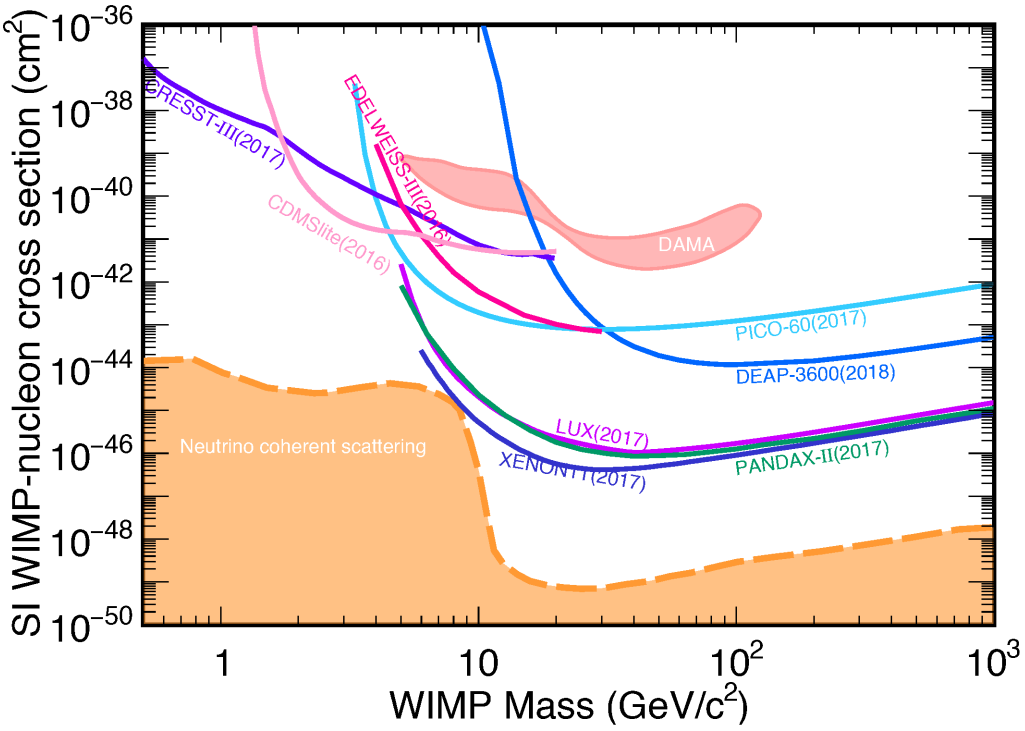

Figure 1.5.1: Upper limits (90% confidence level) of the WIMP-nucleon SI scattering from CRESST [47], CDMSlite [44], EDELWEISS [46], XENON1T [51], LUX [52], PANDAX-II [53], DEAP-3600 [48] and PICO-60 [55]. The DAMA/LIBRA claims the existence of dark matter in the pink shaded region. The orange shaded region shows backgrounds from the coherent neutrino scattering with a Xe target.

For Spin-Dependent cross section, PICO-60 [55] achieved the highest sensitivity using a superheated bubble chamber (Figure 1.5.2). The detection medium is fluorine-rich liquids C_3F_8; ^{19}F has large $\lambda^2 J(J+1)$. The superheated detector can be operated at a condition where the detector can be insensitive to gamma or beta radiations. A further background suppression is achieved through the measurement of the bubble's acoustic emission allowing for discrimination between the fluorine recoil from alpha-ray backgrounds.

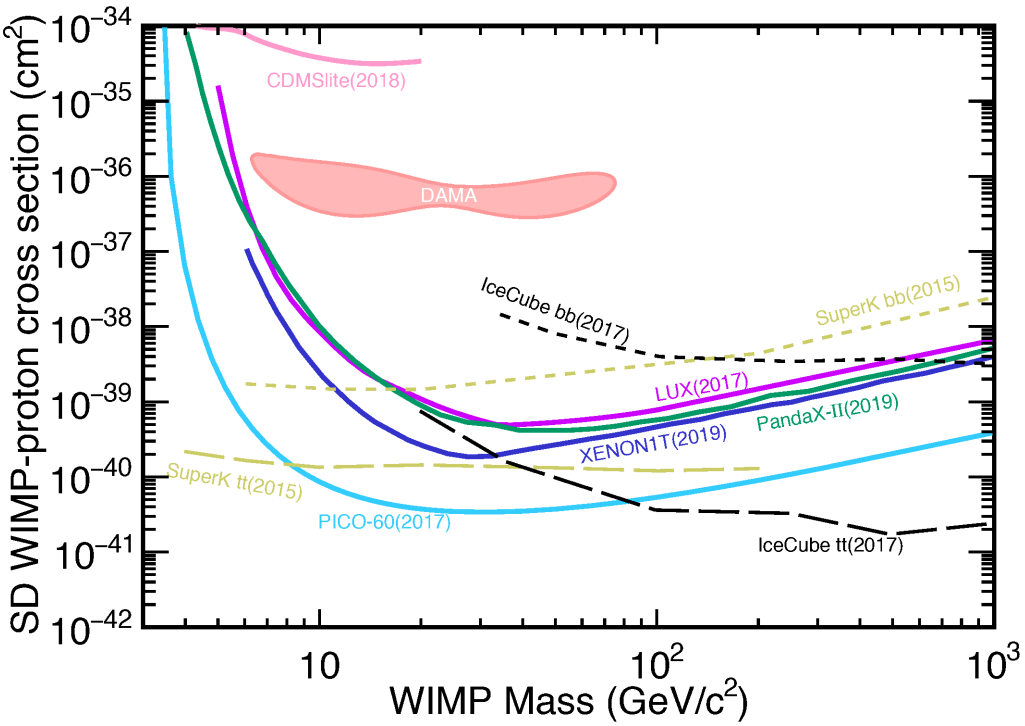

Figure 1.5.2: Upper limits (90% confidence level) of the WIMP-proton SD scattering from PICO-60 [55], LUX [56], PANDAX-II [57], XENON1T [58], and CDMSlite [59]. The dashed and dotted line are results from indirect search, SuperK [60] and IceCube [61]. The DAMA/LIBRA claims the existence of dark matter shown as the pink shaded region [62].

1.5.2 Directional signature searches

Here we review the directional dark matter experiments and current R&D effort. Results of exclusion limit by directional experiments are summarized in Figure 1.5.3.

DRIFT The DRIFT collaboration is the pioneer of the directional dark matter experiments utilizing the low pressure gas Time Projection Chamber (TPC). The readout device is constructed by Multi-Wire Proportional Counters (MWPCs) with a readout pitch of 2 mm. A 1 m^3 detector was demonstrated at the Boulby mine. They use a gas mixture of 73% CS_2 + 25% CF_4 + 2% O_2 at 55 mbar. The CS_2 molecules capture primary ionized electrons and form negative ions. The negative ions are transported to the readout plane instead of the electrons. The negative-ion drift enables to reduce the diffusion effect and thus develop a large size detector with a long drift distance. In addition, a small component of O_2 enables to measure the absolute position along the drift direction. The DRIFT collaboration demonstrated the first background-free operation using this technique and achieved the sensitivity of 0.28 pb at 100 GeV/c^2 without directional information [63].

MIMAC The MIMAC collaboration is developing a matrix of micro-Time Projection Chambers (μTPC). The detector is base on a Micromegas [64] with strip readouts. The

gas mixture is 70% CF_4 + 28% CHF_3 + 2% C_4H_{10} at a pressure of 50 mbar which enables a high gain and the three-dimensional reconstruction of a few keV nuclear recoil tracks. The prototype detector is operated at Modane underground laboratory with an active volume of 5.8 L [65]. In the recent R&D the MIMAC collaboration achieved the angular resolution of 14° and 2° for the fluorine kinetic energy of 6.3 keV and 26.3 keV, respectively [66].

DMTPC The DMTPC collaboration developed a gaseous detector read by a CCDs. The gas mixture is 100% CF_4 at 40-100 mbar. The DMTPC collaboration demonstrated the first measurement of the vector track direction utilizing the head-tail recognition. A 10 L prototype detector demonstrated 40° recoil angle resolution at 80 keV threshold and set an exclusion limit as the result of a dark matter search at surface laboratory [67].

NEWSdm The NEWSdm collaboration is developing a nano imaging tracker by using a novel emulsion technology [68]. The solid detector has an advantage of the large mass. However since the emulsion detector cannot obtain time information, it always needs to point in the direction of the constellation Cygnus. Recently, a technical test with a 10 g emulsion sample was performed in the Laboratori Nazionali del Gran Sasso (LNGS).

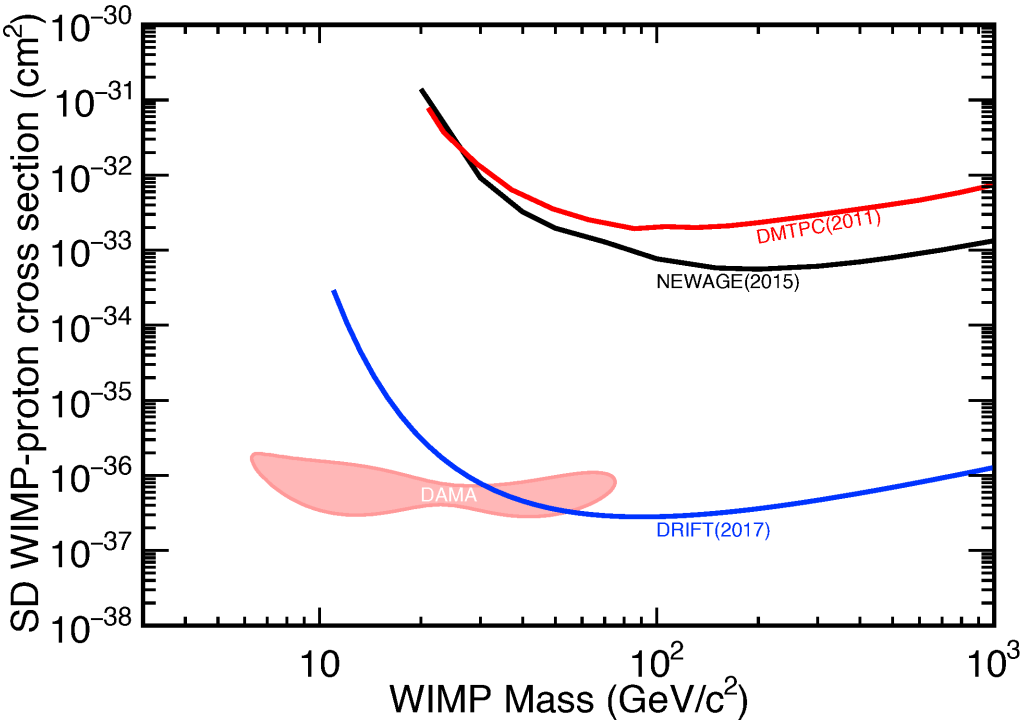

Figure 1.5.3: Upper limits (90% confidence level) of the WIMP-proton SD scattering from DRIFT [63], NEWAGE [69] and DMTPC [67] experiments. The claim of DAMA/LIBRA is shown as the pink shaded region [62].

1.6 NEWAGE

NEWAGE (NEw generation WIMP search with an Advanced Gaseous tracker Experiment) is a directional dark matter experiment using a low pressure gas μTPC. The direction-sensitive experiment needs to detect the direction of recoil nuclei. Hence a time projection chamber (TPC) at low pressure gas and a readout device, μ-PIC, which is one variation of micro pattern gaseous detectors (MPGDs), are used. The gas medium CF_4 is chosen for the dark matter search since fluorine has an advantage of the Spin-Dependent WIMP-proton scattering.

In 2007, a direction-sensitive dark matter search was performed in a surface laboratory [70]. The fiducial volume was 21.5×22×31 cm^3 (15 L) with 150 Torr and the exposure was 0.15 kg·days. In 2010, an underground measurement at Kamioka Observatory was performed with the NEWAGE-0.3a detector. The fiducial volume was $20 \times 25 \times 31$ cm^3 (16 L) with 152 Torr and the exposure was 0.52 kg·days. A μTPC was then developed as the NEWAGE-0.3b' detector in order to enhance the sensitivity. The energy threshold decreased by reducing the gas pressure to 76 Torr. In addition, a gas circulation system with a cooled charcoal was installed in order to reduce radon backgrounds. In 2015, the underground measurement using the NEWAGE-0.3b' detector was performed and the best directional sensitivity was achieved [69]. These results are the only published limit from a directional experiment which uses the measured direction. However, a certain amount of radioactivity, which potentially contributed to the background, was later found inside the μ-PIC. Therefore the surface material of μ-PIC, which is the dominant background source, was replaced with the less radioactive material. This new developed low-background μ-PIC was called LAμ-PIC [71]. In 2017, the detector at Kamioka Observatory was upgraded to NEWAGE-0.3b" by installing a LAμ-PIC and a directional dark matter search started. In this thesis, the first physics results using NEWAGE-0.3b" are reported.

Chapter 2

Detector

NEWAGE-0.3b" detector was designed for the directional dark matter search and installed in Kamioka underground laboratory. In this section, we introduce the concept of NEWAGE experiment, details of the NEWAGE-0.3b" detector and its performance. In Section 2.1, the principle of the nuclear detection by using μ-TPC is explained and the NEWAGE-0.3b" structure is introduced. In Section 2.2, the detector components are introduced. In Section 2.3, the data acquisition system is described. Finally the detector performance of the nuclear event reconstruction, the energy calibration, the detection efficiency, the gamma rejection power and the angular resolution is discussed in Section 2.4

2.1 NEWAGE-0.3b" detector

The NEWAGE-0.3b" detector is a low-pressure gas μTPC that is comprised of a Low Alpha-ray emitting μ-PIC (LAμ-PIC), a Gas Electron Multiplier (GEM) and a TPC cage. A schematic concept of the WIMP detection in NEWAGE-0.3b" is shown in Figure 2.1.1. A WIMP dark matter (purple) induces a nuclear recoil (red) which passes through the gas volume and ionizes the gas molecules (blue). Ionized electrons drift to the two-dimensional tracking detector, LAμ-PIC, by the uniform electric field and their position and charge information are measured. The three-dimensional track of charged particle is reconstructed by two-dimensional track information taken by the LAμ-PIC and the arrival time of ionized electrons in each strips. Also, the deposit energy of charged particle is reconstructed by charge information taken by the LAμ-PIC. The detection volume is 31 $\times$ 31 $\times$ 41 cm^3 (40 L). The photograph of the inside of μ-TPC is shown in Figure 2.1.2. The detector coordinate is defined in Figure 2.1.3. The photograph of whole system of the NEWAGE-0.3b" detector is shown in Figure 2.1.4.

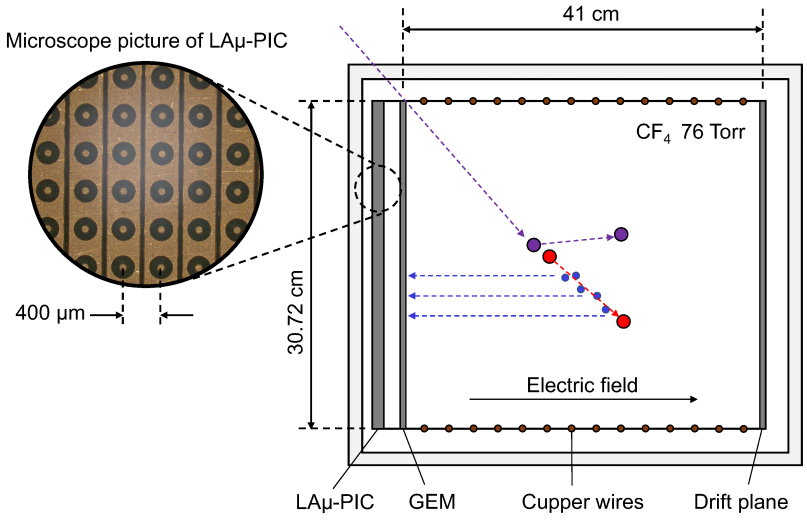

Figure 2.1.1: Schematic concept of the WIMP detection in the NEWAGE-0.3b" detector. A WIMP dark matter (purple) induces a nuclear recoil (red) which passes through the gas volume and ionizes gas molecules (blue). Ionized electrons are detected by the LAμ-PIC with tracking and energy information. The top-left images shows the pixel electrode structure of the LAμ-PIC, on which there are 768 $\times$ 768 pixels with a pitch of 400 μm.

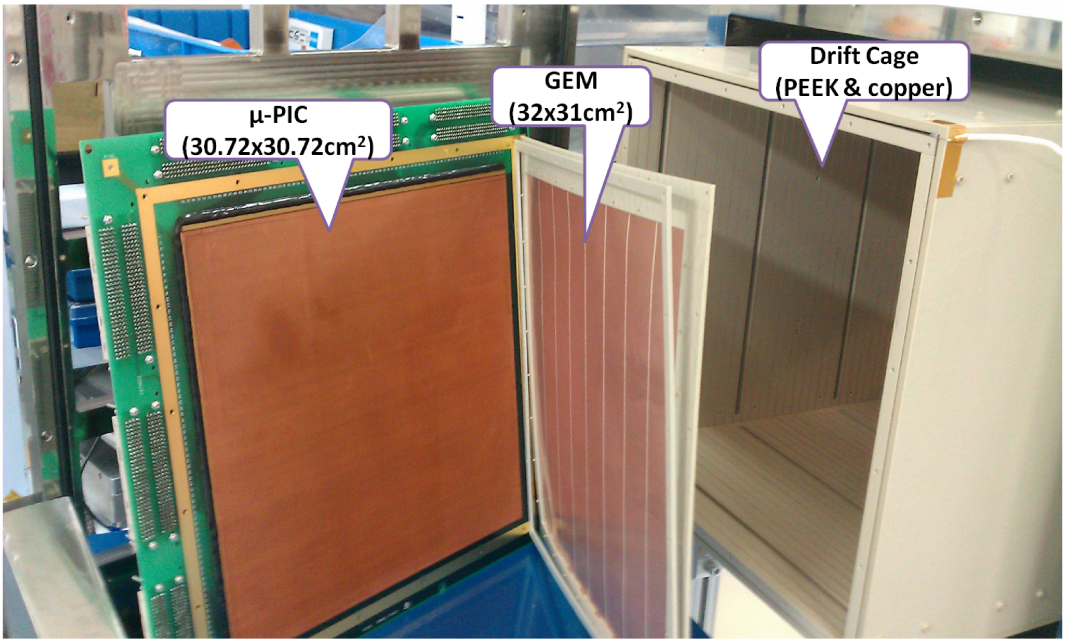

Figure 2.1.2: Photograph of the inside of μTPC. The two-dimensional tracking detector of the μ-PIC and the intermediate amplifier of the GEM are seen. The detection area of the μ-PIC and the GEM are 31×31 cm^2 and 32×31 cm^2, respectively. The drift cage is made of PEEK. The cooper wires with a spacing of 1 cm are placed on the side walls. *Source:* Taken from K. Nakamura [72].

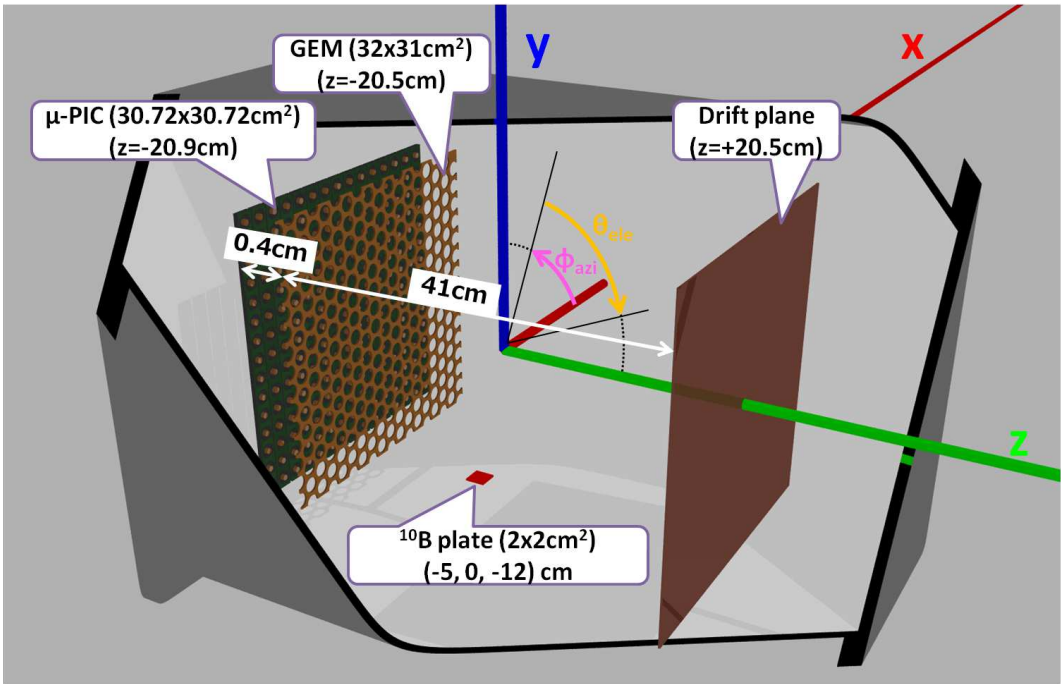

Figure 2.1.3: Schematic image of the μ-TPC and the definition of the detector coordinate. The red, blue and green lines show the x, y and z axis. A ^{10}B glass plate is placed for an energy calibration.
Source: Taken from K. Nakamura [72].

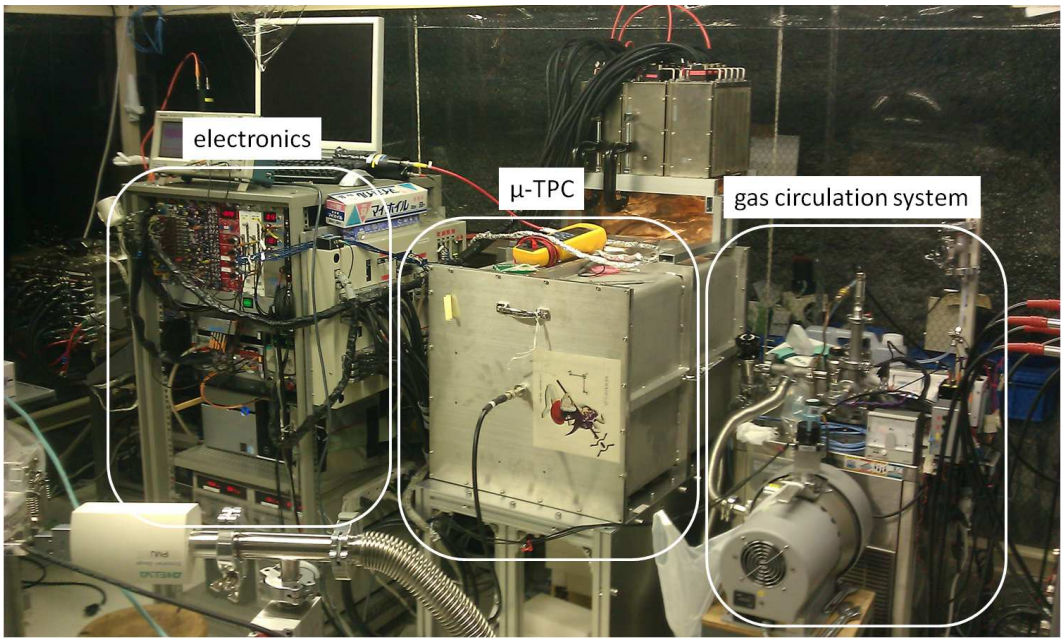

Figure 2.1.4: Photograph of the whole system of NEWAGE-0.3b" detector in Kamioka Observatory. The three components of the electronics (power modules and a data acquisition system), the μTPC and the gas circulation system constitute the whole system.
Source: Taken from K. Nakamura [72].

2.2 Detector components

2.2.1 μTPC

The main background source of the previous dark matter search published in Ref. [69] was alpha particles from the uranium (U) and thorium (Th) series contaminated in the material of the μ-PIC [72]. Since alpha particles are helium nuclei, it was difficult to discriminate from the target nuclear recoils induced by dark matter analytically. Hence it was necessary to reduce these background sources at a hardware level. Low Alpha-ray emitting μ-PIC (LAμ-PIC) was developed for solving this problem [71]. The structure of the pixel electrode is shown in Figure 2.2.1. The photograph of the LAμ-PIC with a detection area of 30.7×30.7 cm^2 is shown in Figure 2.2.2. The LAμ-PIC has 768 × 768 pixels with a pitch of 400 μm. These electrodes are connected by 768 anode strips and 768 cathode strips. The anode and cathode strips are orthogonally formed and thus a two-dimensional position of a hit pixel can be obtained. The structure of the pixel electrode is same as that of a conventional μ-PIC [73], while the material facing the detection volume was changed. The new material is a combination of polyimide (PI) without the glass fiber and epoxy, which is a factor of hundred times less contaminated by isotopes of ^{238}U and ^{232}Th. The contamination of radioactivity is summarized in Table 2.2.1. A performance comparable to the conventional μ-PIC was reported in Ref. [71].

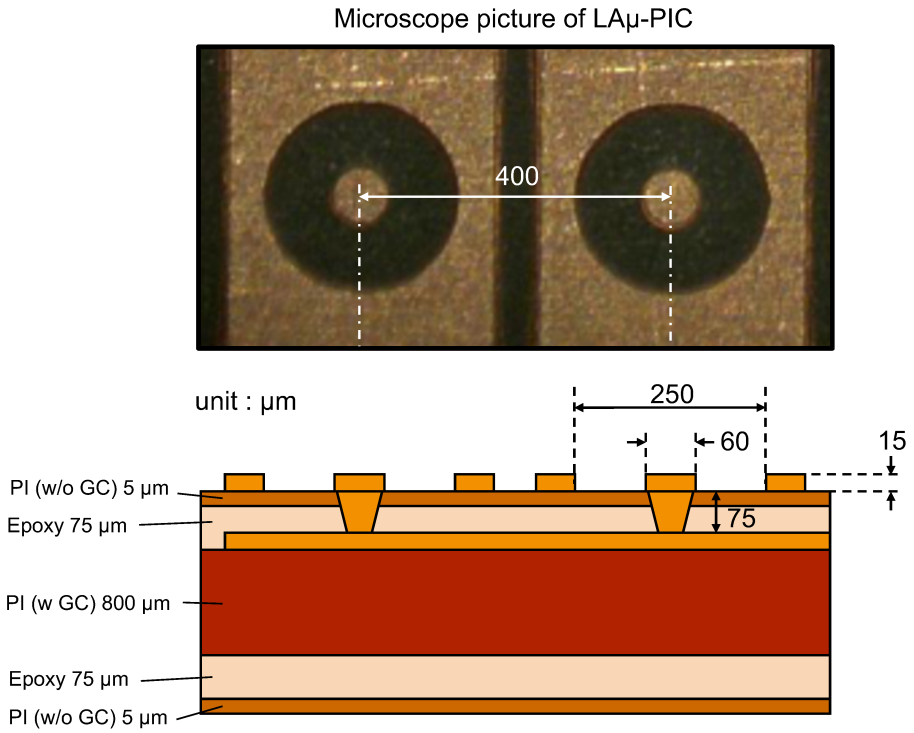

Figure 2.2.1: Microscope picture of a LAμ-PIC (top) and the designed structure of the pixel electrode of a LAμ-PIC (bottom). The surface material is polyimide without the glass fiber (5 μm) and epoxy (75 μm) which is a factor of hundred times less contaminated than that used for a conventional μ-PIC [71].

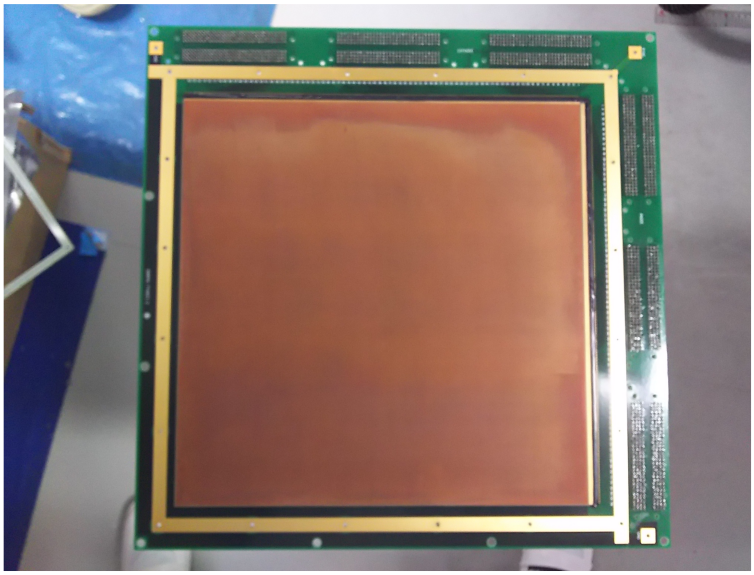

Figure 2.2.2: Photograph of a LAμ-PIC. The detection area is 31×31 cm^2. The 768 × 768 pixels with a pitch of 400 μm are formed.
Source: Taken from T. Hashimoto [71].

Table 2.2.1: Uranium and thorium contamination in the surface materials of the LAμ-PIC [71]. The surface material of the conventional μ-PIC and the LAμ-PIC are PI(w/GC) 100 μm and PI(w/o GC) 5 μm + epoxy 75 μm, respectively.

Sample	^{238}U middle stream (ppm)	^{238}U upper stream (ppm)	^{232}Th (ppm)
PI(w/GC) 100 μm	$(3.9 \pm 0.1) \times 10^{-1}$	$(3.8 \pm 0.1) \times 10^{-1}$	1.81 ± 0.04
PI(w/o GC) 5 μm + epoxy 75 μm	$< 2.98 \times 10^{-3}$	$< 2.86 \times 10^{-2}$	$< 6.77 \times 10^{-3}$

A Gas Electron Multiplier (GEM) [74] was used in order to obtain a sufficient gas gain while keeping a stable operation. Copper electrodes of 5 μm thick are formed on both sides of a 100 μm thick liquid crystal polymer (LCP). Holes with a diameter of 70 μm are made with a pitch of 140 μm. The effective area is 32.0×31.0 cm^2 covering the whole detection area of the LAμ-PIC. The GEM was installed at a distance of 4 mm from the LAμ-PIC and used as a first stage gas amplifier.

A TPC field cage was installed in order to make a uniform electric field. The field cage was made of four plates of polyether ether ketone (PEEK) plastic plates. PEEK is known to emit less out-gas and to be less contamination of uranium and thorium. Wires with a spacing of 1 cm were placed on the side walls of the TPC cage and chained by resistors.

2.2.2 Gas medium

The target gas should have a large cross section of WIMP-nucleus scattering. Also the diffusion effect during the electron-drift needs be small not to smear the track information. Carbon tetrafluoride (CF_4) contains fluoride which has a large cross section for the Spin-Dependent interaction. Moreover the electron diffusion is small because the electron

drift velocity in CF_4 gas is large. The simulated electron drift velocity and diffusion by MAGBOLTZ [75] are shown in Figures 2.2.3 and 2.2.4, respectively. Low pressure gas is preferred so that the recoil nucleus has a long track. The simulated track-lengths of helium, carbon and fluorine nuclei by SRIM [76] are shown in Figure 2.2.5. Therefore CF_4 gas at low pressure is used in NEWAGE-0.3b" detector. The vacuum vessel was filled with CF_4 gas at 76 Torr (0.1 bar). The properties of CF_4 gas are summarized in Table 2.2.2.

Table 2.2.2: Properties of carbon tetrafluoride (CF_4) gas.

Molecular weight	88.01 g/mol
Density	3.76 g/L (15°C, 1 atom)
Melting / Boiling point	89.55 K / 143.35 K
W value	34 eV [77]

Since the deposit energy of the nuclear recoil goes into not only ionization but also heat, the ionization signal is quenched. It is known as a quenching factor and defined by the ratio between the energy used for ionization $E_{\mathrm{ionization}}$ and the total energy loss E_{total}; $F_{\mathrm{q}} = E_{\mathrm{ionization}}/E_{\mathrm{total}}$. The calculated quenching factors of helium, carbon and fluorine by SRIM are shown in Figure 2.2.6. The measured energy of the nuclear events can be unfolded to the recoil energy using this quenching factor.

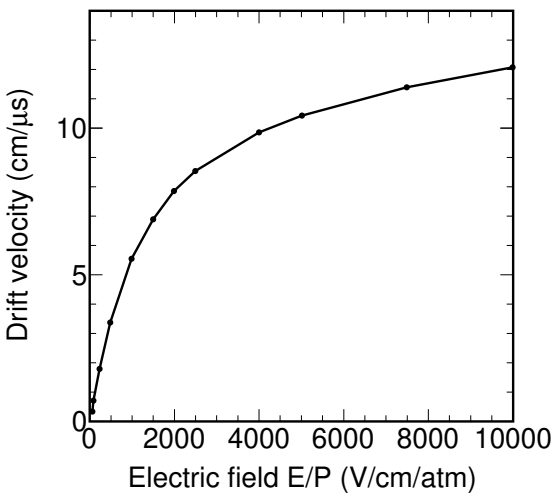

Figure 2.2.3: Drift Velocity of the electron in CF_4 gas calculated by MAGBOLTZ simulation.

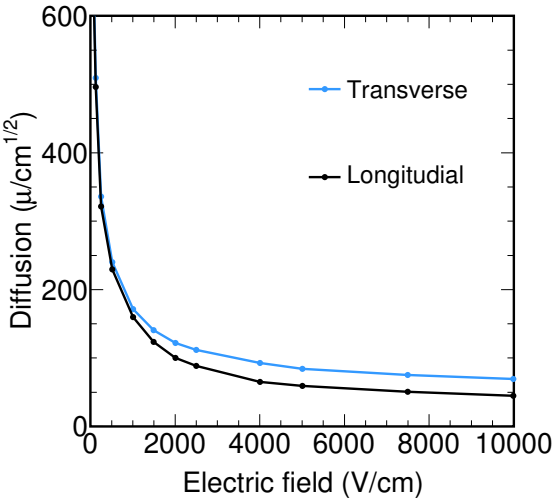

Figure 2.2.4: Transverse and longitudinal diffusions of the electron in the CF_4 gas simulated by MAGBOLTZ.

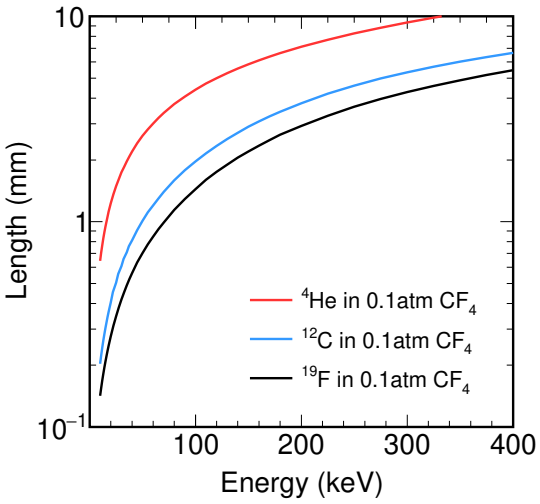

Figure 2.2.5: Track-lengths of helium, carbon and fluorine nuclei in CF_4 gas at 76 Torr (0.1 bar) simulated by SRIM.

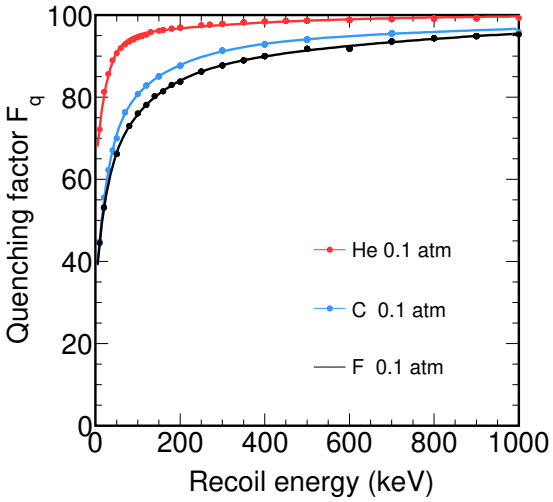

Figure 2.2.6: Quenching factors of helium, carbon and fluorine nuclei in CF_4 gas at 76 Torr (0.1 bar) simulated by SRIM.

2.2.3 Gas circulation system

The natural radioactive isotopes ^{238}U, ^{232}Th would be contaminated in most of the material in the detector components such as metal, plastic and glass-fiber. ^{222}Rn and ^{220}Rn in U-chain and Th-chain emanate from the materials into the gas. These radon nuclei decay in the gas volume and alpha- and beta-rays, potential backgrounds, are emitted. The number of radon nuclei N_{Rn} in the vessel is written as

$$N_{\mathrm{Rn}} = \frac{R_0}{\lambda_{\mathrm{Rn}}}\left(1 - e^{-\lambda_{\mathrm{Rn}} t}\right), \tag{2.2.1}$$

where R_0 is a generation rate of the radon and $\lambda_{\mathrm{Rn}}(= \ln 2/\mathrm{T}_{\mathrm{Rn}})$ is the time constant of the radon life time T_{Rn}. Since the half life of ^{220}Rn is 55.6 sec, the number of ^{220}Rn reaches an equilibrium within several minutes. On the other hand, since the half life of ^{222}Rn is 3.82 days, the number of ^{222}Rn gradually increases with a time constant of several days. If the gas circulation system could be installed with a material which traps radon effectively, the number of radon nuclei is rewritten by

$$N_{\mathrm{Rn}} = \frac{R_0}{\lambda_{\mathrm{Rn}} + FP/V}\left(1 - e^{(-\lambda_{\mathrm{Rn}} + FP/V)t}\right), \tag{2.2.2}$$

where V is the volume of vessel, F is the flow rate and P is the absorption probability of the charcoal. Since it takes a lot of time to circulate the gas in the vessel, it is difficult to reduce ^{220}Rn. Therefore, a material selection is required for a fundamental reduction. Only ^{222}Rn can be removed using the gas circulation system effectively.

In order to remove radons, we installed a gas circulation system with a cooled charcoal.

Figure 2.2.7 shows a schematic view of the gas circulation system. The CF_4 gas passes through the charcoal (TSURUMICOAL 2GS) of 100 g and radons in the gas are absorbed. The circulation pump is a dry scroll pump (XDS5 scroll pump (EDWARDS)). The flow rate of 1000 ml/min is controlled by a needle valve and monitored by a mass flow meter. A refrigerator and a heater keep a stable cooling at 230 K.

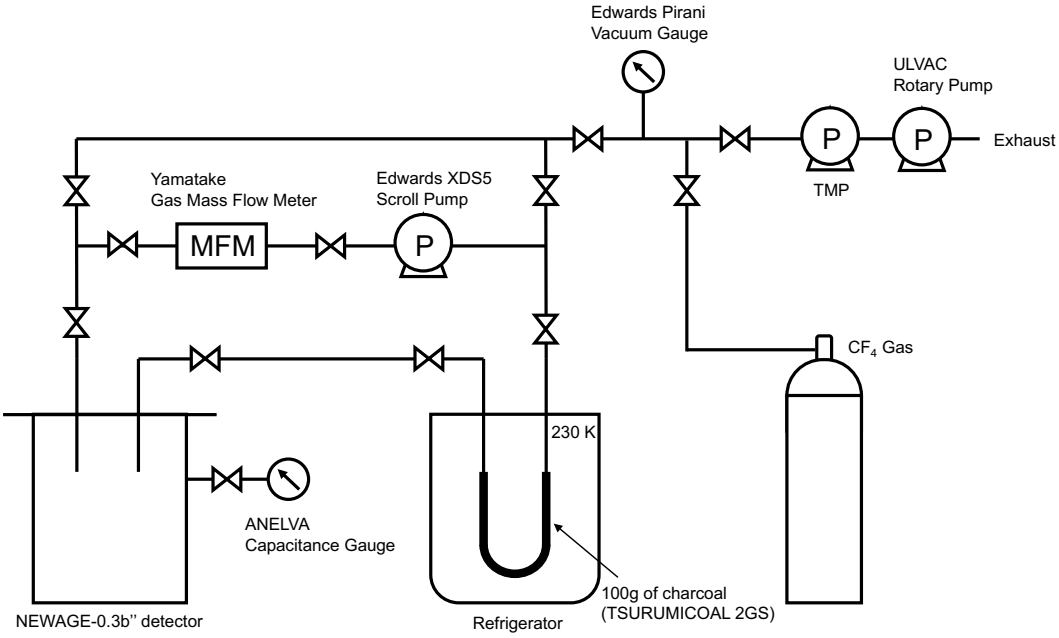

Figure 2.2.7: Schematic view of the gas circulation system of NEWAGE-0.3b".

2.3 Data acquisition system

The schematic structure of the data acquisition system (DAQ) is shown in Figure 2.3.1. The anode and cathode signals of the LAμ-PIC were processed by an Amplifier-Shaper-Discriminator (ASD) chip (SONY CXA3653Q) [78]. One chip can process four channels. The specification is summarized in Table 2.3.1. The 768 cathode signals were grouped into four channels. Each of these signals was divided into two. One of the divided signals was attenuated by a factor of three to make a dynamic range of detected energy wider while the other is directly recorded. Each signal was sent to a 100 MHz flash ADC and the waveforms were recorded.

The DAQ has two trigger modes. One is a self-trigger mode. In this mode, anode signals were grouped into 16 channels and any one hit of these signals was used as trigger (self TRIG in Figure 2.3.1). As the position information, the addresses of all hit strips are recorded. The time-over-threshold (TOT) which is correlated to the energy deposit of one strip is also recorded. The self-trigger mode was used for the dark matter search.

The other DAQ is the external-trigger mode. This mode was mainly used for the

measurement of the drift velocity using a ^{252}Cf fission source. A plastic scintillator set nearby the fission source detects a prompt gamma-ray and makes a trigger (ext TRIG in Figure 2.3.1). Since a signal of the prompt gamma-ray provides the reaction time of the neutron-nucleus elastic scattering, the drift time can be determined. In this mode, coincidences of the anode and cathode address were taken and minimum/maximum address are recorded in order to reduce the data size.

Table 2.3.1: ASD chip (SONY CXA3653Q) characteristics [78]

Gain of preamplifier	0.8 V/pC
Integration time	16 ns
Gain of main-amplifier	7
ENC at C_d = 150pF	~7500
Other specifications	4 channels in a QFP48 plastic package
	threshold voltage common for all 4 channels
	comparator with LVDS outputs
	required voltage : +/- 3V, GND

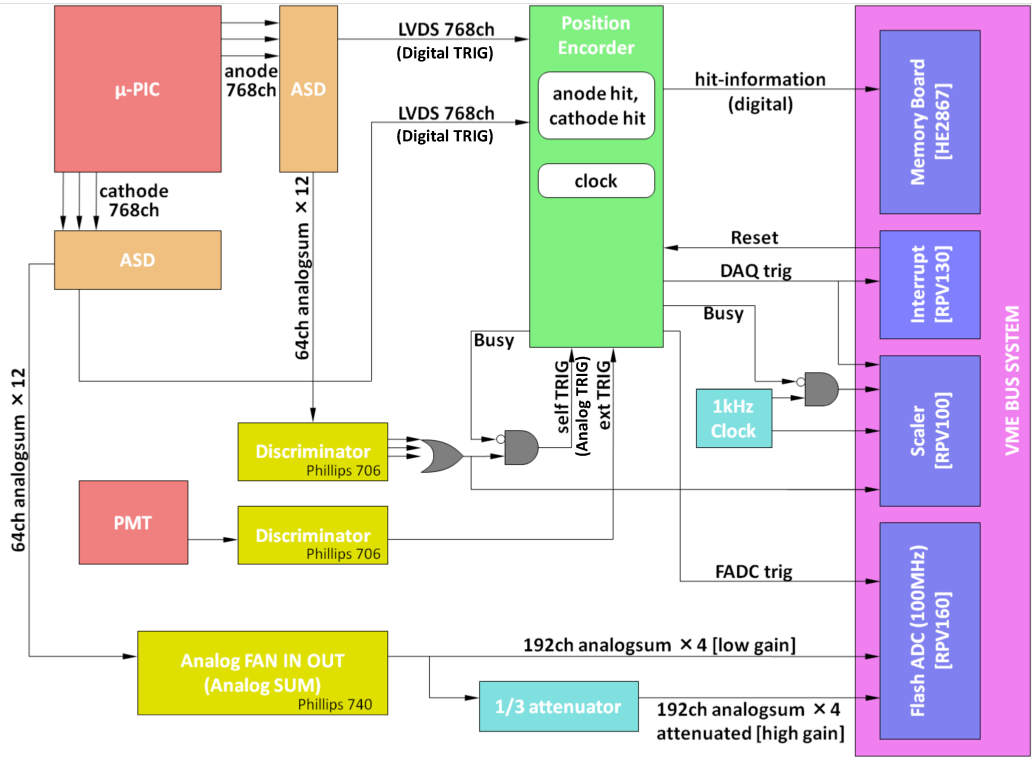

Figure 2.3.1: Schematic of the Data Acquisition system (DAQ) of NEWAGE-0.3b". *Source:* Taken from K. Nakamura [72].

2.4 Performance

In this section, we discuss the performance of the NEWAGE-0.3b" detector. The energy scale was calibrated using alpha particles generated by a neutron capture reaction of ^{10}B. The drift velocity, the detection efficiency was measured by irradiating with neutrons from a ^{252}Cf fission source. In addition, the gamma rejection power is measured by using a ^{137}Cs source.

First, we describe the event reconstruction in Section 2.4.1. Here some parameters which enable to remove background events are defined. In Section 2.4.2, we introduce the method of the energy calibration. In Section 2.4.3, we discuss how to measure the drift velocity which is needed to determine the relative z coordinate. In Section 2.4.4, we introduce the event selection. Accordingly, the detection efficiency of the nuclear recoil events and the gamma rejection power are discussed in Section 2.4.5, 2.4.6 and 2.4.7. Finally, the angular resolution is discussed in Section 2.4.8.

2.4.1 Event reconstruction

As mentioned in the previous section, information in the self-trigger mode is strip-addresses of anode and cathode, TOTs of hit strips, and waveforms which are grouped down to 4 channels of cathode. The energy, the track-length and the direction are reconstructed from these information. Some more effective parameters for removing backgrounds are also calculated.

Figure 2.4.1 shows an event sample measured with a ^{252}Cf fission source. The energy is calculated using obtained waveforms by a 100 MHz flash ADC. After the pedestal was estimated from the first 100 clock, the peak position was searched. The integrated value in the time range over the threshold $\mathrm{S_{ADC}}$ (blue area in the top pannel) corresponds to the charge deposit. The $\mathrm{S_{ADC}}$ is converted to the electron equivalent energy by an energy calibration described in Section 2.4.2. Also TOT is correlated to the deposit energy on each strip. Total amount of TOTs is defined as TOT-sum (total number of gray squares in the bottom pannels).

The TOT includes the rising time $\mathrm{T_{rise}}$ (red squares in the bottom pannels) and the falling time $\mathrm{T_{fall}}$ (black squares in the bottom panels) information. The position of z_x and z_y in each plane is obtained by multiplying $\mathrm{T^{x,y}_{rise}}$ by the drift velocity. The method of determining the drift velocity will be discussed in Section 2.4.3. The coordinates of (x, z_x) and (y, z_y) have track-shape information. They are fitted by linear functions (red dotted lines in the bottom panels) and the direction and track-length are obtained.

A parameter describing the shape of a track, roundness, is defined as,

$$\mathrm{roundness}_x = \frac{\sum^{N_x}(z_x - a_x x - b_x)^2}{N_x}, \tag{2.4.1}$$

$$\mathrm{roundness}_y = \frac{\sum^{N_y}(z_y - a_y y - b_y)^2}{N_y}, \tag{2.4.2}$$

$$\mathrm{roundness} = \min(\mathrm{roundness}_x, \mathrm{roundness}_y) \tag{2.4.3}$$

where N_x and N_y are the numbers of hits of x and y strips, respectively. Values of

(a_x, b_x) and (a_y, b_y) are best-fit parameters fitting (x, z_x) and (y, z_y) with a linear function, respectively.

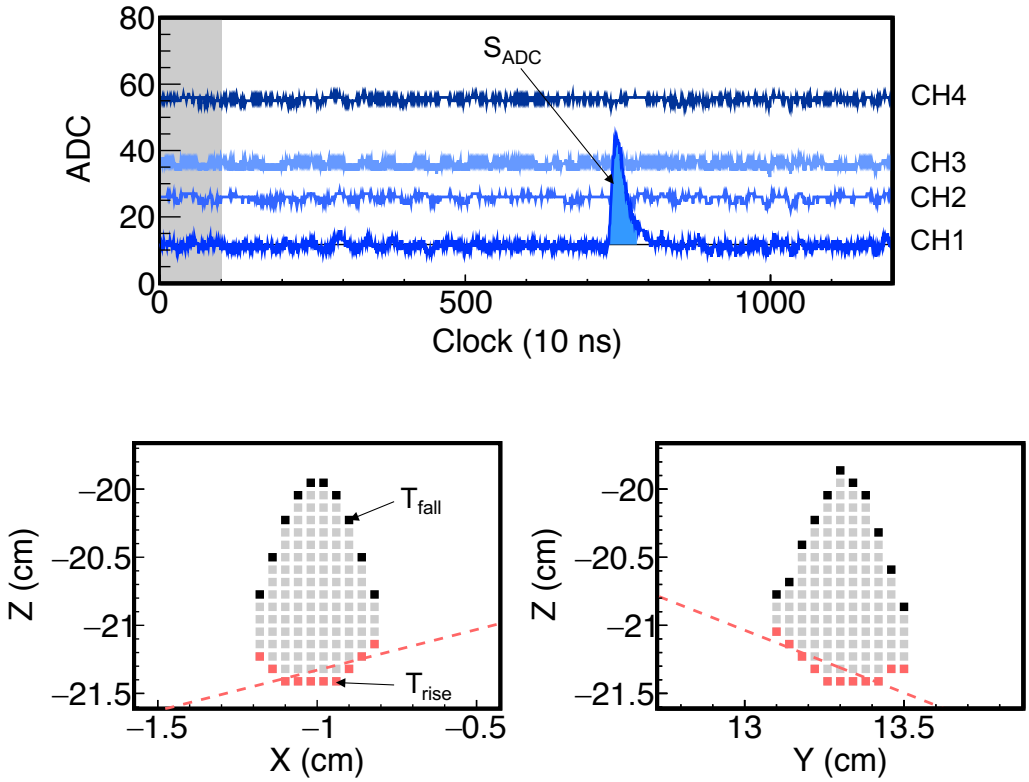

Figure 2.4.1: Obtained event sample with a ^{252}Cf fission source. The upper figure shows the waveforms of cathode signal, which are grouped down to 4 channels, recorded with a 100 MHz flash ADC. The blue shaded area indicates the calculated S_{ADC} as the charge deposit. The lower left (right) figure shows the anode (cathode) TOT information. The red and black squares show rising time and falling time, respectively. The red dotted lines indicate fitted linear functions. The total number of gray squares is defined as TOT-sum. In this event case, the energy is reconstructed as 160 keV. The TOT-sum and roundness are 251 and 0.078, respectively.

2.4.2 Energy calibration

The energy calibration was performed with a glass plate of a ^{10}B layer installed at a position of $(-5, -12, 0)$ cm. The size of the ^{10}B layer was 2×2 cm and the designed thickness was 0.6 μm. The photograph of the glass plate is shown in Figure 2.4.2. The detector was irradiated with neutrons from a ^{252}Cf fission source placed outside of the vessel and the neutrons were thermalized by polyethylene blocks. Thermal neutrons were captured by ^{10}B and alpha particles were emitted. The reactions are written as

$$^{10}\mathrm{B} + \mathrm{n} \rightarrow ^{4}\mathrm{He} + ^{7}\mathrm{Li} + 2.79\ \mathrm{MeV}(6\%)\ , \tag{2.4.4}$$

$$^{10}\mathrm{B} + \mathrm{n} \rightarrow ^{4}\mathrm{He} + ^{7}\mathrm{Li} + 2.31\ \mathrm{MeV} + \gamma(0.48\ \mathrm{MeV})(94\%)\ . \tag{2.4.5}$$

Since the cross section of Equation 2.4.5 is 15 times larger than that of Equation 2.4.4, neutron capture reaction of ^{10}B emits prompt gamma-rays with 0.48 MeV in most of the cases, and the ^{7}Li nuclei and alpha particle share 2.31 (= 2.79 − 0.48) MeV. As a consequence, the generated alpha particle has 1.5 MeV of kinetic energy. Because of the thickness of the ^{10}B layer, the 1.5 MeV alpha particles make a continuous spectrum with an edge at 1.5 MeV, rather than a peak.

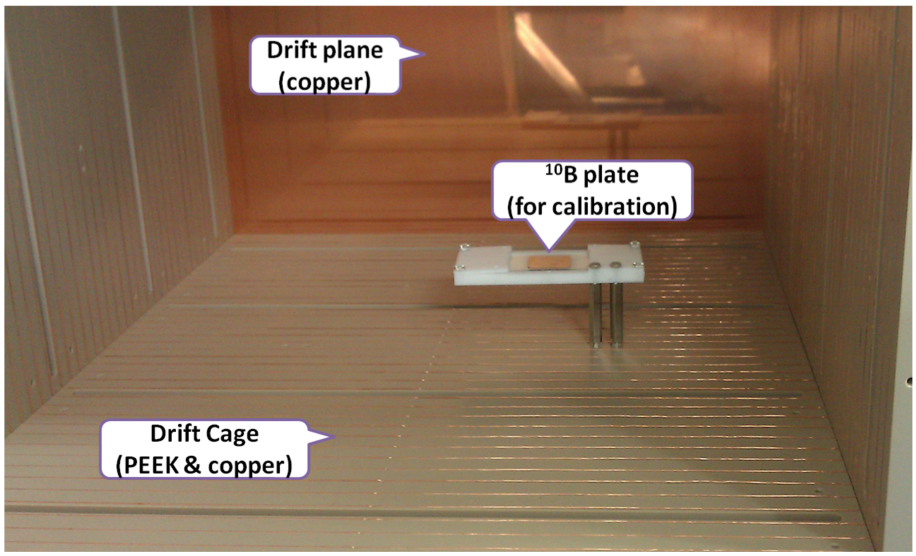

Figure 2.4.2: Photograph of the glass plate on which ^{10}B is deposited. The glass plate was installed at the position of $(-5, -12, 0)$ cm inside the μTPC.
Source: Taken from K. Nakamura [72].

Figure 2.4.3 shows the two-dimensional image of the calibration run. High radiation intensity can clearly be seen around the glass plate. We can effectively select alpha events generated by above reactions utilizing the position information. The measured energy spectrum around the glass plate is shown in Figure 2.4.4. This spectrum contains not only the thermal neutron capture events but also elastic scattering events of fast neutron and nucleus. We simulated these spectrum by using the Geant4 simulation. The measured spectrum was fitted with simulated ones changing the ratio of thermal neutron capture and fast neutron scattering spectrum, the energy scale and the energy resolution. The most likely value of the energy scale, or the calibration factor, was selected.

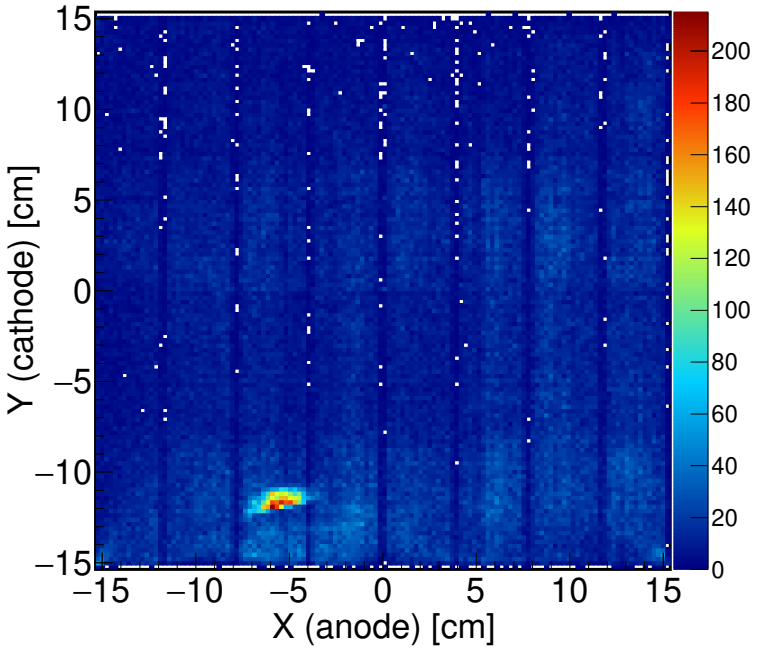

Figure 2.4.3: Two-dimensional image of the calibration run. The high radiation intensity of alpha particles generated by the thermal neutron capture can be seen at the glass plate of $(-5, -12, 0)$ cm.

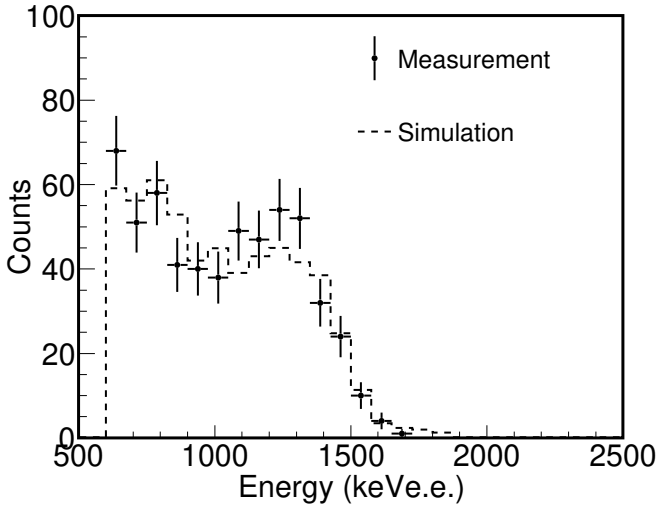

Figure 2.4.4: The energy spectrum of alpha particles emitted by the thermal neutron capture of ^{10}B. The solid and dotted lines are the measurement data and the fitted simulation data, respectively.

High energy (>2 MeV) spectrum was used to check the energy linearity. The measured spectrum above 2 MeV is shown in Figure 2.4.5. Radon background events which make

peak around 6 MeV were used. The detector materials contain some amount of ^{238}U and ^{232}Th. The radioactive noble gas ^{222}Rn and ^{220}Rn are generated in the ^{238}U and ^{232}Th decay series, respectively. ^{220}Rn generates alpha particles with energy of 6.05 MeV, 6.29 MeV, 6.78 MeV and 8.79 MeV. ^{222}Rn also generates alpha particles with energy of 5.49 MeV, 6.00 MeV and 7.69 MeV. We simulated the spectrum of radon in the fiducial volume by a Geant4 simulation. Simulated spectrums of ^{220}Rn and ^{222}Rn are shown in Figures 2.4.6 and 2.4.7, respectively. Both spectrums have peaks around 6 MeV. The mean value of the peak energy of ^{220}Rn and ^{222}Rn are 6.2 MeV and 5.6 MeV, respectively. However the measured peak energy can change by the abundance ratio of the ^{220}Rn and ^{222}Rn in the gas volume. The measured spectrum was fitted with simulated spectrums changing the ratio of ^{220}Rn and ^{222}Rn and the energy scale. The best-fit energy scale was consistent with the one obtained with the ^{10}B calibration within 1 % systematic error.

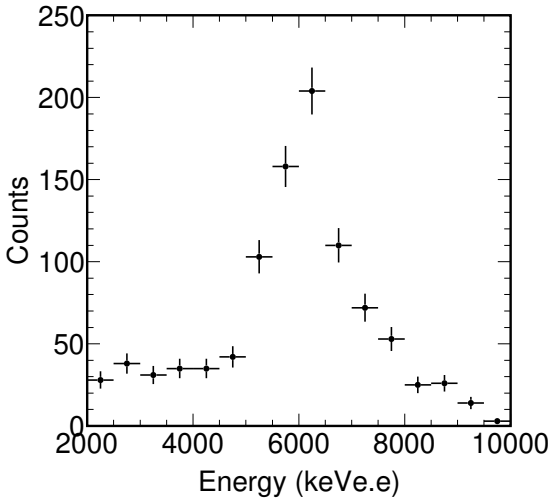

Figure 2.4.5: Measured high energy spectrum of radon backgrounds.

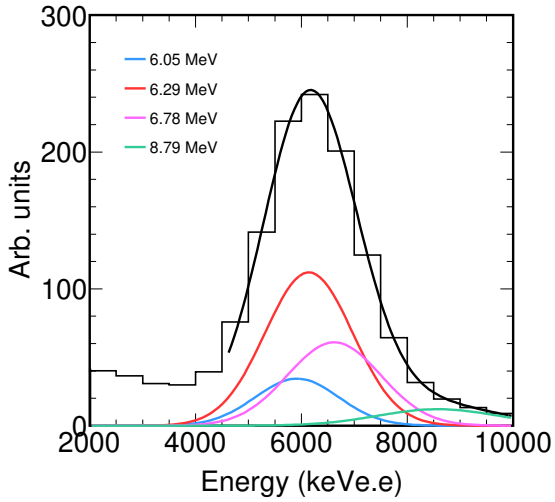

Figure 2.4.6: Simulated spectra of the ^{220}Rn background in the fiducial volume. The black histogram is the total energy spectrum. The blue, red, pink and green lines are contribution from alpha particles with the energy of 6.05 MeV, 6.29 MeV, 6.78 MeV and 8.79 MeV, respectively.

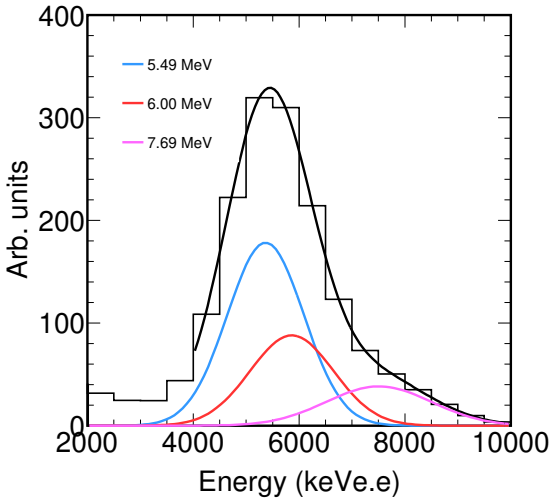

Figure 2.4.7: Simulated spectra of the ^{222}Rn background in the fiducial volume. The black histogram is the total energy spectrum. The blue, red and pink lines are contribution from alpha particles with the energy of 5.49 MeV, 6.00 MeV and 7.69 MeV, respectively.

2.4.3 Drift velocity

The electron drift velocity in the μ-TPC is needed to convert the arrival time (T_{rise}) to the z position. We used the external-trigger mode with a ^{252}Cf fission source triggered by a plastic scintillator placed nearby. Several neutrons and gamma-rays are yielded by the spontaneous fission of ^{252}Cf. The reaction time of the neutron-nucleus elastic scattering was known by using prompt gamma-rays as a trigger and the drift time of the ionized electron was calculated. Figure 2.4.8 shows the measured drift time distribution. The edge structure around 400 clocks corresponds to the maximum drift time where ionized electrons travel the maximum distance of the TPC volume (L_{max} =41 cm). The maximum drift time T_{max} was obtained by fitting the edge structure with an error function. The drift velocity V_D is calculated by $V_D = L_{max}/T_{max}$.

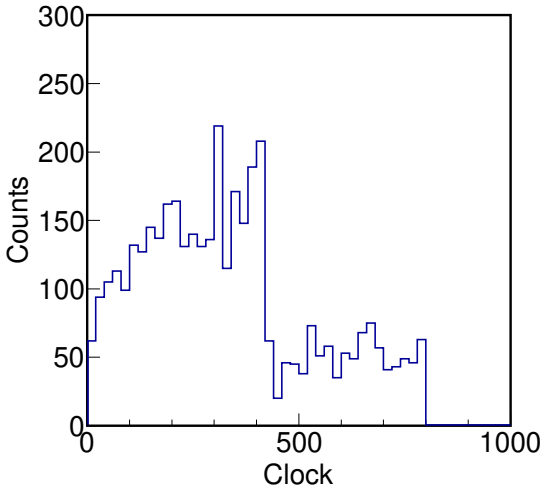

Figure 2.4.8: Distribution of the drift time obtained by the external-trigger mode with a ^{252}Cf source. The edge structure corresponds to the time in which electrons travel a drift distance of 41 cm.

2.4.4 Event selection

The following event selections were applied in order to select nuclear recoil events.

Fiducial cut

The fiducial volume was defined as $28 \times 24 \times 41$ cm^3 in the detection volume $31 \times 31 \times 41$ cm^3. This cut was useful for removing the charged particles from the wall and the ^{10}B plate.

Length-Energy cut

Since charged particles have different energy losses per track length, the track-length with a certain energy is also different. Hence we can identify the nuclear track from the track-length vs. energy distribution. Figure 2.4.9 shows the track-length vs. energy distributions for the ^{252}Cf calibration (black points) and the ^{137}Cs calibration (blue points). From the ^{252}Cf calibration data, we determined nuclear band by fitting with Gaussian function for every energy bin with a width of 10 keV. This cut was useful for removing electron events and alpha particles above 300 keV.

TOT-Energy cut

Energy deposition on a single strip was stored as TOT. Since nuclear events have larger energy losses than electron events, sum of TOT (TOT-sum) for a given energy tends to be large. In addition, since TOT-sum was expected to be linear with respect to the total energy deposit, a parameter defined by dividing the TOT-sum by energy was suitable for this purpose. Figure 2.4.10 shows TOT-sum/energy vs. energy distributions for the ^{252}Cf calibration (black points) and the ^{137}Cs calibration (blue points). From the ^{252}Cf calibration data, we determined the nuclear band by fitting with gaussian function every energy bin with a width of 10 keV. This cut rejected electron events.

Roundness cut

The roundness tends to be small for an event traveling short drift length, since the effect of electron diffusion is small and the track is fitted by straight line well. Hence this parameter was found to have a correlation to the absolute z position. Especially, this parameter was useful to remove "gap events". The gap events are defined as events depositing their all energy in the gas volume between the LAμ-PIC and GEM. These gap events were not amplified by the GEM detector and thus the measured charge was smaller by a factor of the GEM gain than those in the detection volume. In order to reproduce the gap events, we irradiated neutrons from a ^{252}Cf fission source without a drift electric field. Figure 2.4.11 shows the roundness vs. energy distribution for the gap events. The roundness of gap events (red points) were found to be small. The events with roundness > 0.05 were selected in order to remove gap events.

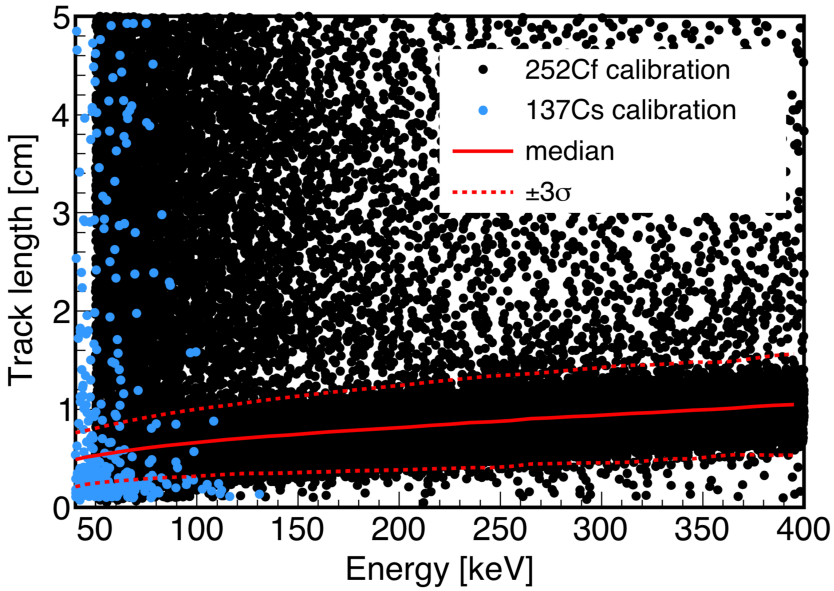

Figure 2.4.9: Track-length vs. energy distributions. The black and blue points represent the ^{252}Cf neutron calibration data and the ^{137}Cs electron calibration data, respectively. The red solid and dotted lines indicate the median and $\pm 3\sigma$ quantiles of the neutron calibration.

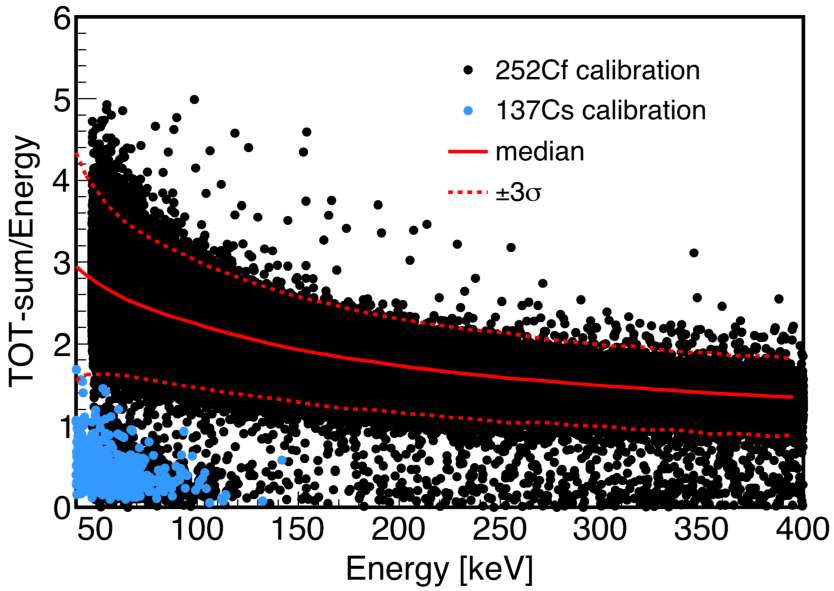

Figure 2.4.10: TOT-sum/energy vs. energy distribution. The black and blue points represent ^{252}Cf neutron calibration data and ^{137}Cs electron calibration data, respectively. The red solid and dotted lines indicate the median and $\pm 3\sigma$ quantiles of neutron calibration.

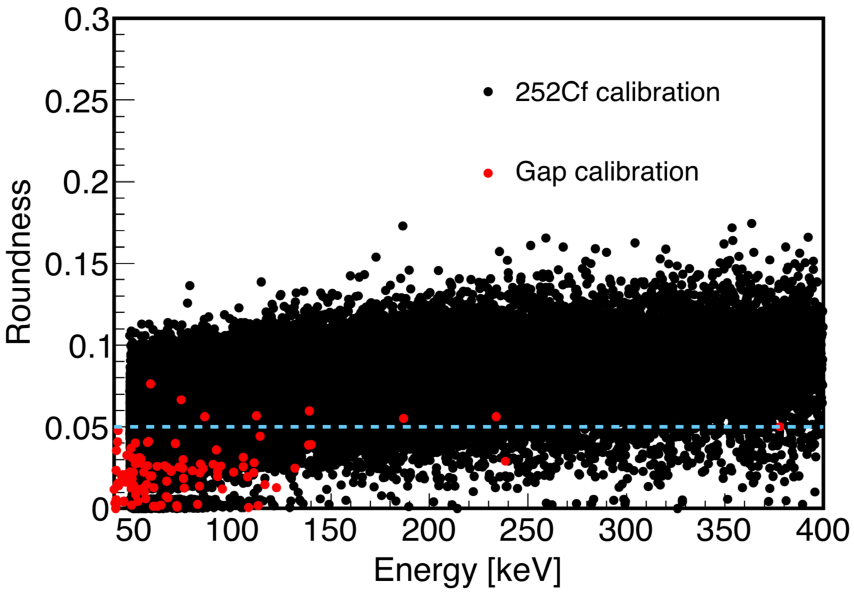

Figure 2.4.11: Roundness vs. energy distribution. The black and red points represent the ^{252}Cf neutron calibration with a drift electric field and without a drift electric field, respectively. The events above cyan dotted line (roundness= 0.05) were selected.

2.4.5 Detection efficiency

The detection efficiency for the nuclear events was evaluated after the event selections described above. We defined the detection efficiency as dividing the measured energy spectrum after all cuts by that representing the number of nuclear recoil interaction estimated by the Geant4 simulation. In order to cancel the position dependence and measure an overall response of the detector, neutrons from a ^{252}Cf fission source were irradiated from six directions and the combined spectrum was used. The source position is summarized in Table 2.4.1. The measured combined spectrum and simulated one is shown in Figure 2.4.12.

The measured detection efficiency of the nuclear recoil events is shown in Figure 2.4.13. The black fit line indicates the detection efficiency when we applied only the fiducial cut. Since the energy deposition of nuclear events (^{19}F and ^{12}C) are sufficiently large , intrinsic detection efficiency of nuclear recoil events should in principle be one. The reason why the efficiency does not reach this intrinsic value, was the low trigger efficiency due to the low gas gain. The plateau trigger efficiency was checked by waveform simulations for the fluorine nuclear recoils. The energy deposit of the fluorine nucleus on each μ-PIC strip was calculated by the Geant4 simulation and converted to charge considering the W value and the gas gain. The waveforms were simulated using the ASD chip characteristics described in Table 2.3.1. The trigger was generated when at least one of the anode signals grouped into 16 channels was over the analog threshold (Analog TRIG in Figure 2.3.1) and any one of anode and cathode signals was over a digital threshold (Digital TRIG in Figure 2.3.1). This trigger system emulated the self-trigger mode. The obtained trigger efficiencies for the fluorine nuclear recoil are shown in Figure 2.4.14. It was confirmed that the plateau trigger efficiency became low with small gas gain. This was a good agreement with the obtained experimental results. In Figure 2.4.13, the red fit line indicates the selection efficiency when all cuts introduced in the previous section were applied. Obtained detection+selection efficiency of nuclear events was 14% at 50 keV.

Table 2.4.1: Coordinates of the ^{252}Cf fission source.

Direction	Coordinates		
	x	y	z
+x	25.5	0	0
+y	0	25.5	0
+z	0	0	47.5
-x	-25.5	0	0
-y	0	-25.5	0
-z	0	0	-47.5

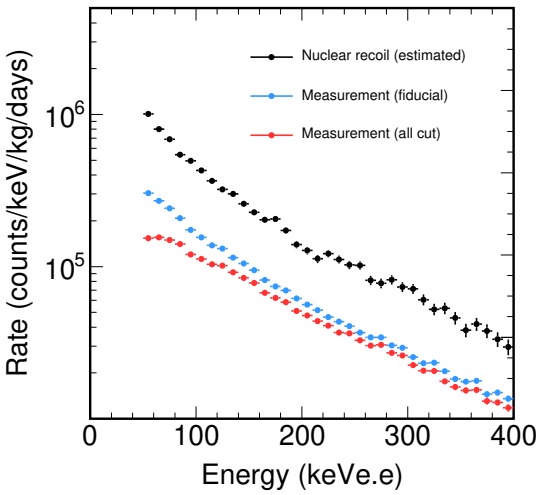

Figure 2.4.12: Combined spectrum at 6 source positions and simulated spectrum. The black points with error bars are estimated interaction spectrum by a Geant4 simulation. The blue points with error bars are measured spectrum after only the fiducial cut. The red points with error bars are measured spectrum after all cuts.

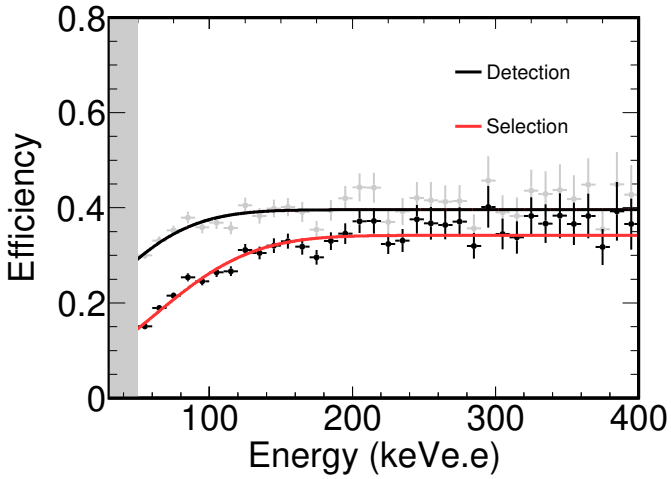

Figure 2.4.13: Typical detection efficiency for the nuclear events. The black solid line is detection efficiency in the fiducial volume. The red solid line is detection efficiency after the event selection.

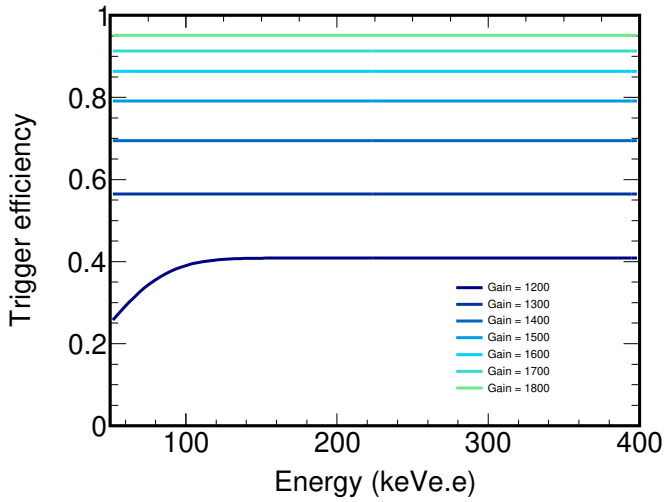

Figure 2.4.14: Trigger efficiency of various gas gains for the fluorine nuclear recoils. The measured gas gain corresponds to about 1200.

2.4.6 Gamma rejection power

We evaluated the gamma rejection power, or the detection efficiency of electrons, by irradiating the detector with gamma-rays from a ^{137}Cs source. The source was placed at a position of $(0, 0, 47.5)$ and the data with a total live time of 5.3 days were taken. Figure 2.4.15 shows the measured spectrum along with the simulated one. Here, the simulated energy spectrum of the detected energy in the fiducial area is plotted as the "Simulation". The number of measured events in 50-60 keV and 60-400 keV energy range are one and zero, respectively. The gamma rejection power was defined by dividing the measured energy spectrum after all cuts by the simulated one. Figure 2.4.16 shows the obtained gamma rejection power. The gamma rejection power or the electron detection efficiency for the energy range of 50-60 keV was $(1.3^{+3.0}_{-1.1}) \times 10^{-6}$. Since the measured number of event in 60-400 keV was zero, an upper limit was set for that energy range. The obtained values are summarized in Table 2.4.2.

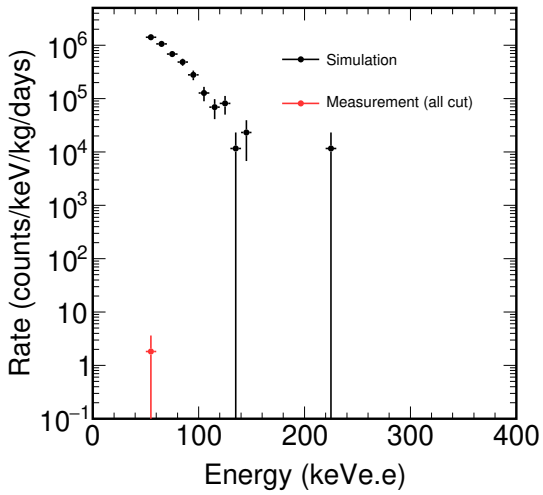

Figure 2.4.15: Measured and simulated spectra with a ^{137}Cs source. The black points indicate the expected rate reacted in fiducial volume. The red point shows the measured spectrum after all cuts.

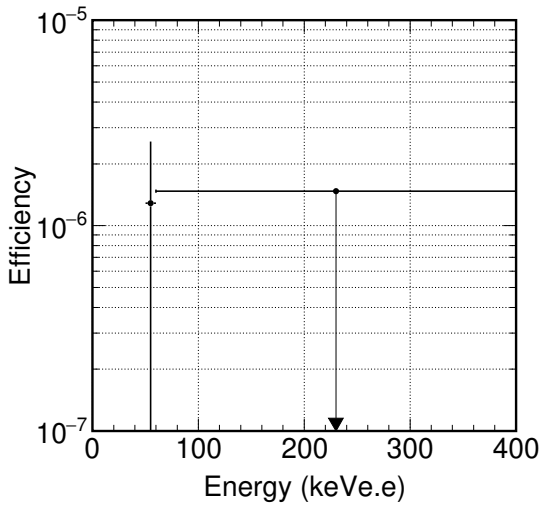

Figure 2.4.16: Calculated gamma rejection efficiency. A finite value was obtained for the 50-60 keV, while an upper limit was set in 60-400 keV.

Table 2.4.2: Summary of the obtained gamma rejection power.

	50-60 keV	60-400 keV
Gamma rejection power	$(1.3^{+3.0}_{-1.1}) \times 10^{-6}$	$< 1.5 \times 10^{-6}$

2.4.7 Direction dependent efficiency

We measured the relative direction-dependent efficiency of nuclear recoil in the energy range of 50-100 keV. The detector was irradiated with neutrons from a ^{252}Cf fission source placed at six positions (Table 2.4.1). We confirmed that we can emulate isotropic recoil (standard deviation was 13%) with a weighted sum of these six measurements by Geant4 simulations. Figure 2.4.17 shows the measured distribution of the elevation angle θ_{ele} and the azimuth angle ϕ_{azi} in the detector coordinate. The definition of the detector coordinate is shown in Figure 2.1.3. We can see that the efficiency is low around XY plane, XZ plane and YZ plane. This is due to the poor track reconstruction along anode/cathode strips. Also, there are higher efficiency areas along the diagonal lines from the direction of the anode and the cathode strips. This is because the current tracking algorithm tends to recognize the diffused tracks to such directions.

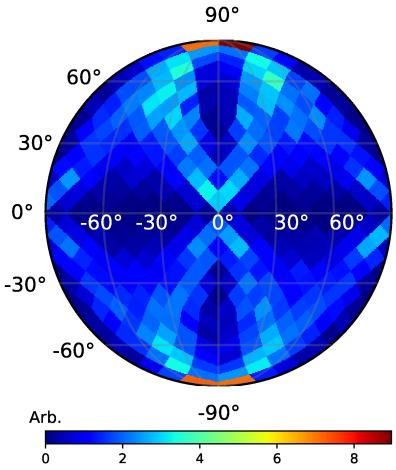

(a) 50-60 keV

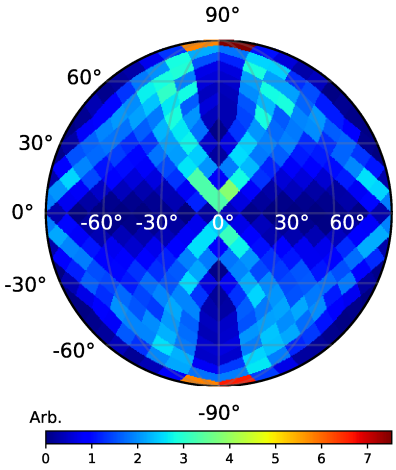

(b) 60-70 keV

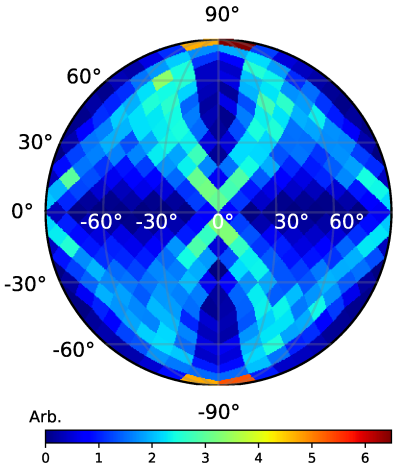

(c) 70-80 keV

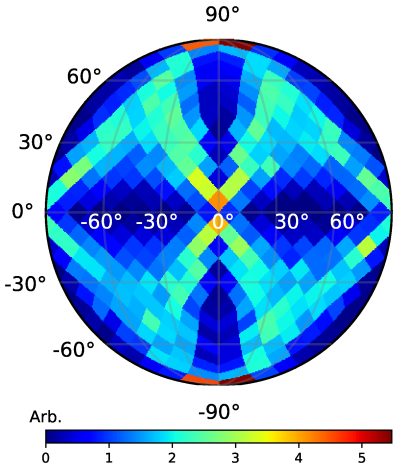

(d) 80-90 keV

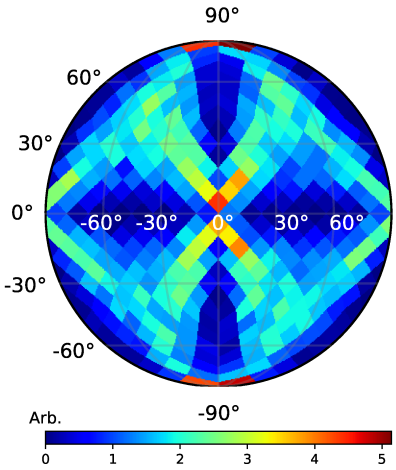

(e) 90-100 keV

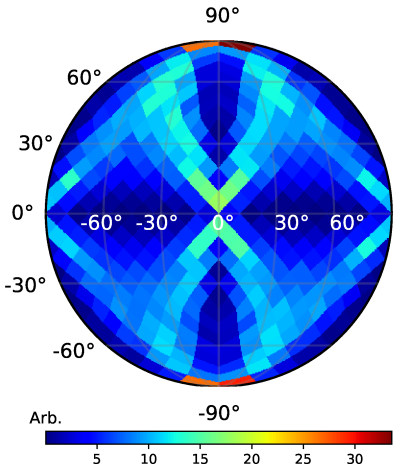

(f) 50-100 keV

Figure 2.4.17: Relative direction-dependent efficiencies. The axis with white and black label is the azimuth angle ϕ_{azi} and the elevation angle θ_{ele} in the detector coordinate, respectively.

2.4.8 Angular resolution

We measured the angular resolution of the nuclear tracks using the fast neutrons from a ^{252}Cf fission source. We evaluated the angular resolution by the comparison of measured and simulated distributions of the recoil angle cosγ. The recoil angle γ is defined in Figure 2.4.18.

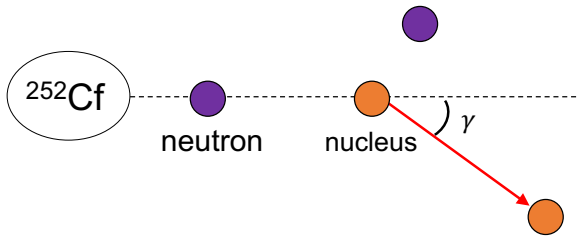

Figure 2.4.18: Definition of the nuclear recoil angle γ.

The detector was irradiated with fast neutrons from a ^{252}Cf fission source placed at six positions (see Table 2.4.1) in order to measure an overall response of the detector. Since we do not recognize head-tail of the tracks in this study, only absolute cosγ distribution was evaluated. Simulated |cosγ| distributions with various angular resolutions in the energy range of 50-100 keV, 100-200 keV and 200-400 keV are shown in Figure 2.4.19(a), (b) and (c), respectively.

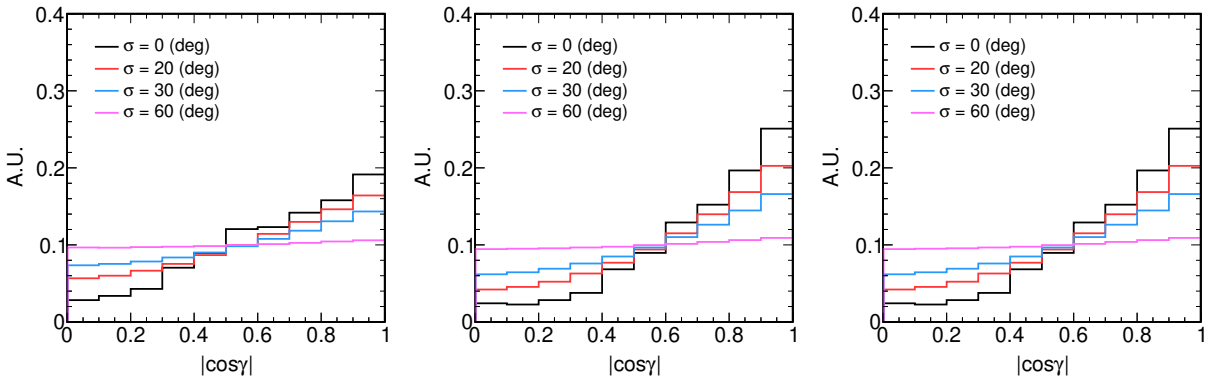

(a) 50-100 keV (b) 100-200 keV (c) 200-400 keV

Figure 2.4.19: Simulated absolute cosγ distributions in the energy range of 50-100 keV (a), 100-200 keV (b) and 200-400 keV (c) along with several angular resolutions.

Measured directions were weighted by the direction-dependent efficiency and thus corrected |cosγ| was obtained. The observed |cosγ| distribution in each energy range is shown

in Figure 2.4.20. In order to determine the angular resolution, we compared simulated $|\cos\gamma|$ distribution with various angular resolutions to the measured distributions. In the energy range of 50-100 keV, we obtained the angular resolutions of $48^{+6.8}_{-2.2}$ degree where the obtained least χ^2/d.o.f was 7.9/9. The chi-square distributions in the energy range of 50-100 keV, 100-200 keV and 200-400 keV are shown in Figure 2.4.22(a), (b) and (c), respectively. The result of obtained angular resolutions is shown in Figure 2.4.21. The expected forward-backward ratio of $|\cos\theta_{\rm cygnus}|$ from the dark matter signal is 30%.

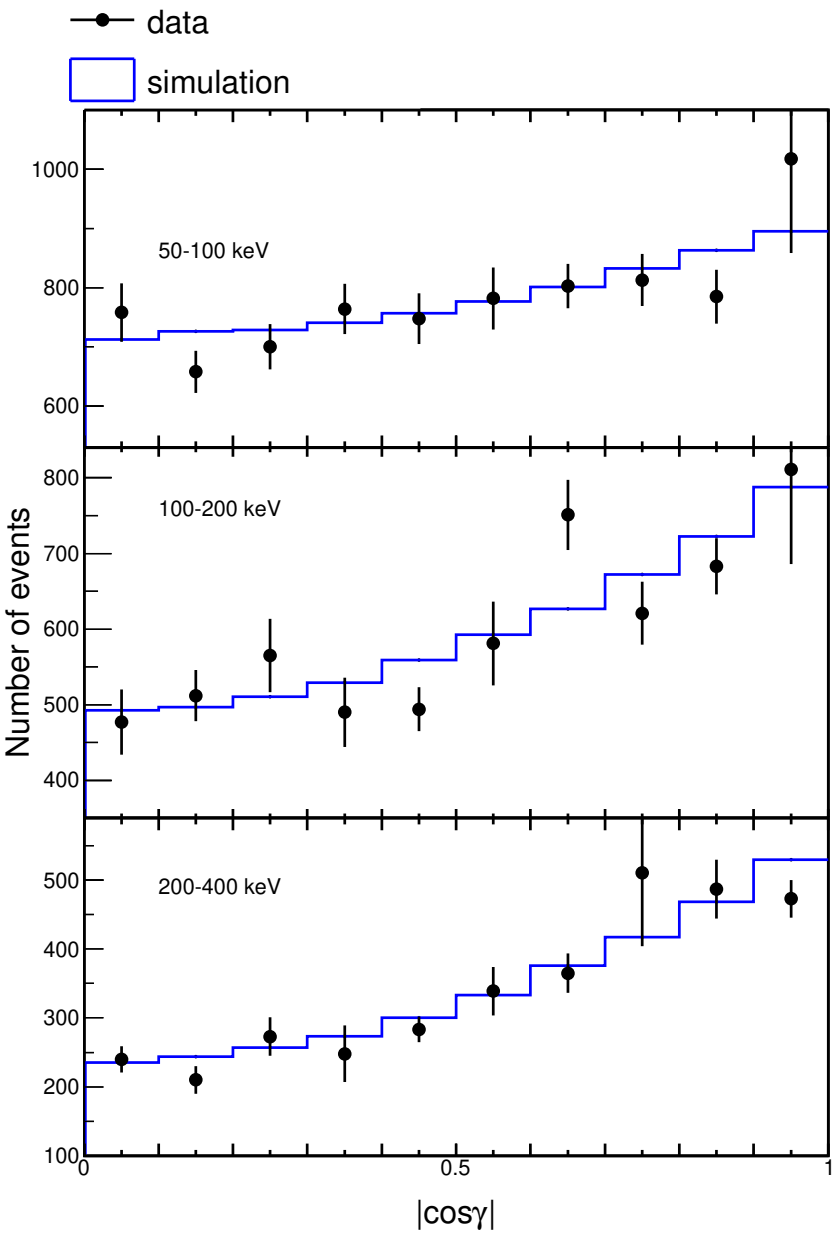

Figure 2.4.20: Observed $|\cos\gamma|$ distributions in each energy range. The black dots and blue line are measurement data and simulation, respectively.

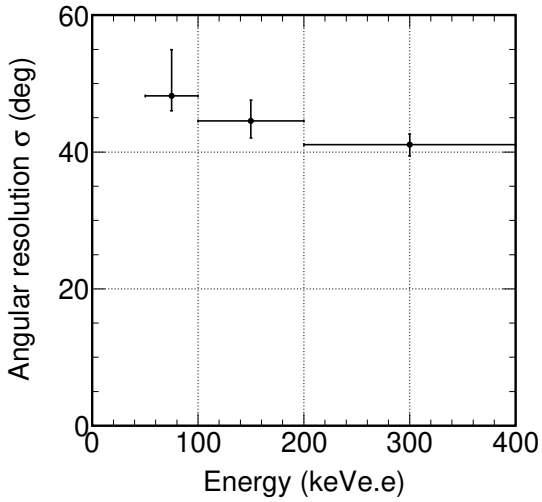

Figure 2.4.21: Obtained angular resolutions for each energy bin.

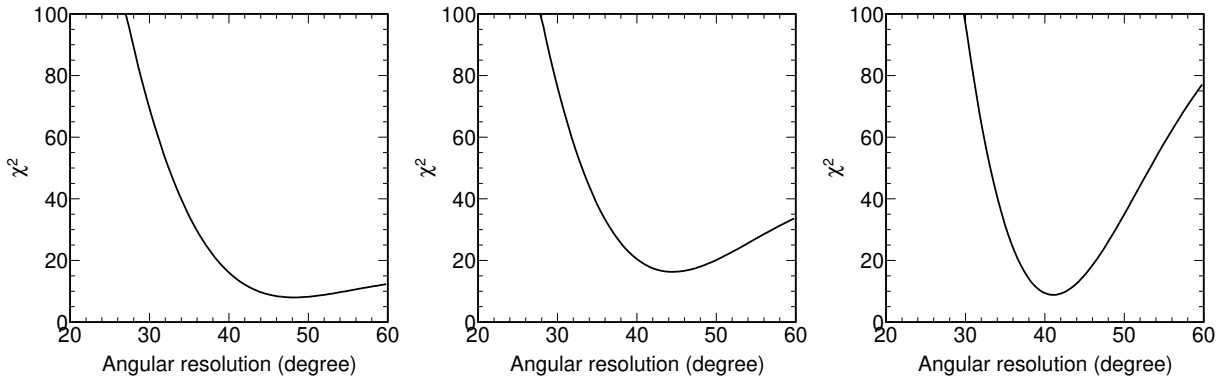

(a) 50-100 keV (b) 100-200 keV (c) 200-400 keV

Figure 2.4.22: Chi-square distributions in the energy range of (a) 50-100 keV, (b) 100-200 keV and (c) 200-400 keV.

Chapter 3

Experiment

A direction-sensitive dark matter experiment was carried out with NEWAGE-0.3b", whose sensitivity was expected to be improved adopting a newly-developed LAμ-PIC. The measurement properties and the results are described in this chapter. In Section 3.1, the dataset of the dark matter search is described. The obtained energy spectrum and that after the event selection are discussed in Section 3.2. Before the directional analysis, the systematic uncertainties are discussed in Section 3.3. Finally, the results of the directional dark matter search are discussed in Section 3.4.

3.1 Measurement

A directional dark matter search was carried in Laboratory B of Kamioka Observatory located at 2700 m water equivalent underground (36.25'N, 137.18'E). The NEWAGE-0.3b" described in the previous section was used for the measurement. The LAμ-PIC plane was placed vertically and the z-axis is aligned to the direction of S30°E. A sub-run, Run22-1 was performed from June 6^{th} 2018 to 24^{th} Aug. 2018 and another sum-run, RUN22-2 was carried out from 20^{th} Sept. 2018 to 14 $^{\text{th}}$ Nov. 2018. The target gas was CF_4 at 76 Torr (0.1 bar) and the target mass in the fiducial volume of $28 \times 24 \times 41$ cm^3 (28 L) was 10 g. The run properties are summarized in Table 3.1.1. Figure 3.1.1 shows the cumulative livetime. The total livetime was 107.6 days. In order to confirm the detector stability, various environment variables were monitored during the data-taking (see Appendix A).

Table 3.1.1: Run properties of RUN22

Period	Livetime (days)	Exposure (kg·days)
	RUN22-1	
2018 June 8 - June 12	3.6	3.8×10^{-2}
2018 June 14 - June 27	12.7	1.3×10^{-1}
2018 July 6 - July 19	12.8	1.3×10^{-1}
2018 July 20 - Aug. 8	18.1	1.9×10^{-1}
Total	47.2	4.9×10^{-1}
	RUN22-2	
2018 Sept. 21 - Oct. 2	10.5	1.1×10^{-1}
2018 Oct. 4 - Oct. 30	25.0	2.6×10^{-1}
2018 Nov. 1 - Nov. 13	11.5	1.2×10^{-1}
2018 Nov. 14 - Nov. 28	13.6	1.4×10^{-1}
Total	60.5	6.3×10^{-1}
RUN22 total	107.6	1.12

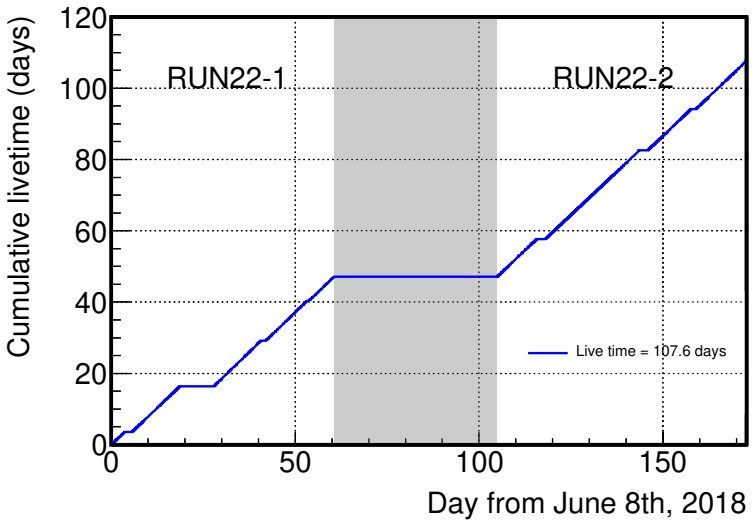

Figure 3.1.1: Cumulative livetime of the RUN22. The period of gray region indicates the gas exchange term.

The energy calibration and the detection efficiency measurement were carried out every two weeks. Figures 3.1.2 and 3.1.3 show the time variations of the gas gain and the energy resolution, respectively. The decrease of the gas gain was due to the gas deterioration. The energy scale of the data during the dark matter search was corrected considering the time-dependence of the gas gain. The energy resolution has shown no time dependency

within the error. The average and the standard deviation of the energy resolution were 13.2% and 2.3%, respectively. This uncertainty was treated as the systematic error which will be discussed in Section 3.3. The measured drift velocity is summarized in Table 3.1.2.

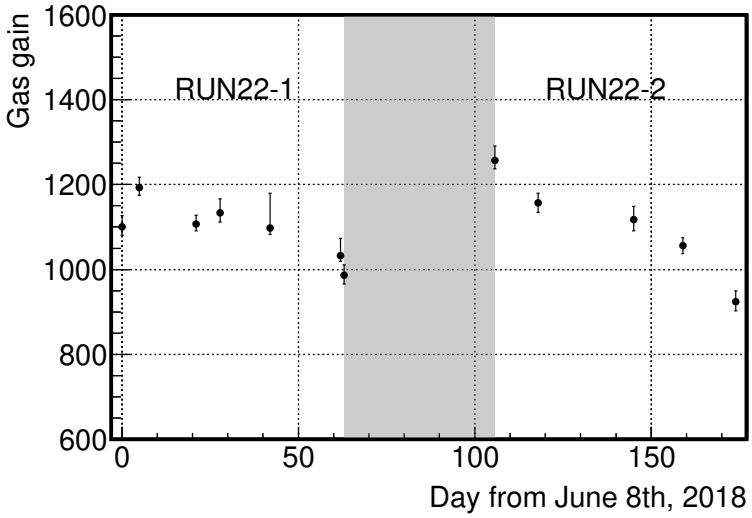

Figure 3.1.2: Time variation of the gas gain during the dark matter search. The period of gray region indicates the gas exchange term.

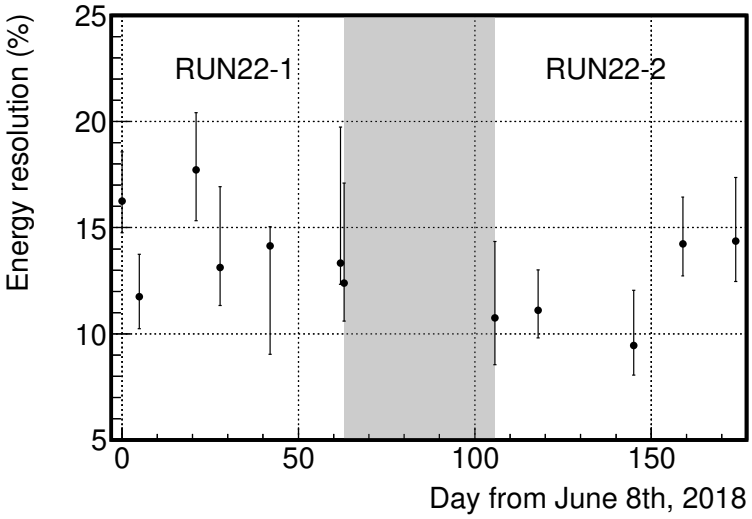

Figure 3.1.3: Time variation of the energy resolution during the dark matter search. The period of gray region indicates the gas exchange term.

Table 3.1.2: Measured drift velocities of RUN22-1 and RUN22-2.

RUN22-1	9.6 ± 0.3 cm/μs
RUN22-2	9.6 ± 0.1 cm/μs

3.2 Event selection

Event selections, described in Section 2.4.4, were applied to the measured data. The fiducial cut was applied first. Figures 3.2.1, 3.2.2 and 3.2.3 show the Length-Energy, the TOT-Energy and the Roundness-Energy distributions after the fiducial cut, respectively. A large fraction of the events had long track lengths and small TOTs, which indicated that most of the measured events were electrons. A final event sample was obtained by applying the Length-Energy, TOT-Energy and Roundness cuts. Figures 3.2.4, 3.2.5 and 3.2.6 show the Length-Energy, TOT-Energy and Roundness-Energy distributions after all event selections, respectively. The energy spectrum of the final sample are shown in Figure 3.2.7. Table 3.2.1 shows remaining number of events in the energy region of 50-60 keV after each cut.

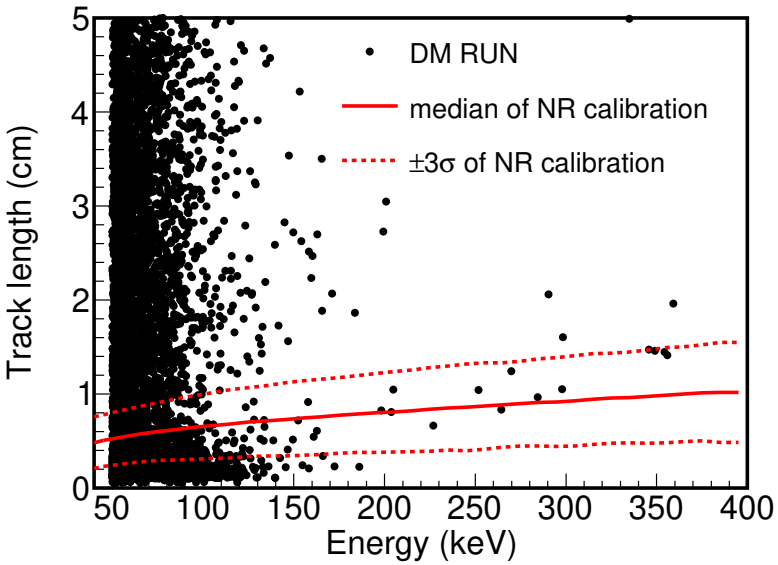

Figure 3.2.1: Length-Energy distribution after the fiducial cut.

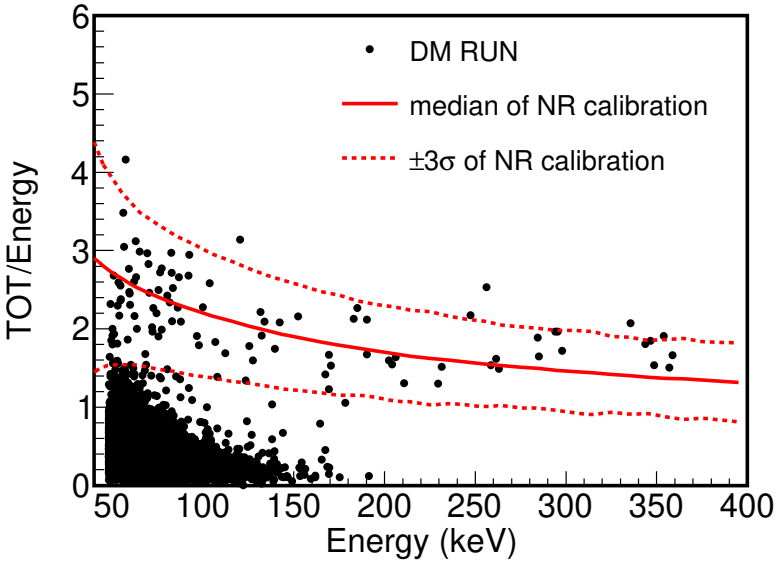

Figure 3.2.2: TOT-Energy distribution after the fiducial cut.

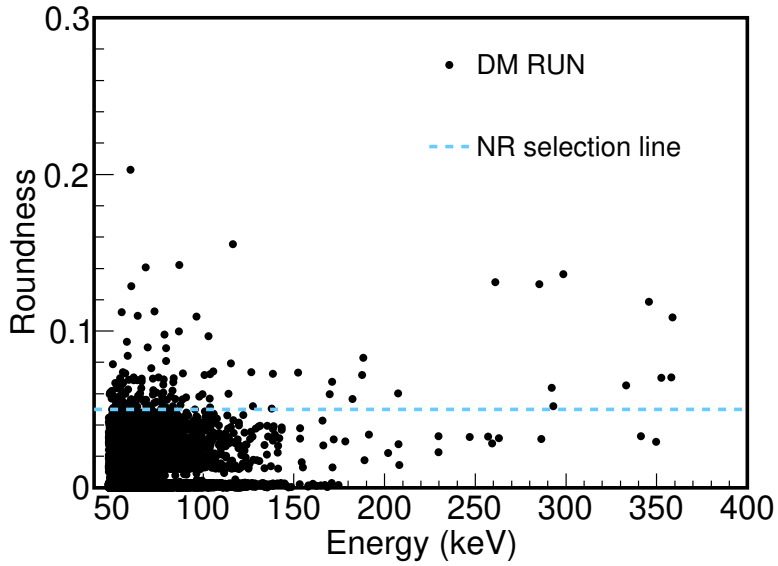

Figure 3.2.3: Roundness-Energy distribution after the fiducial cut.

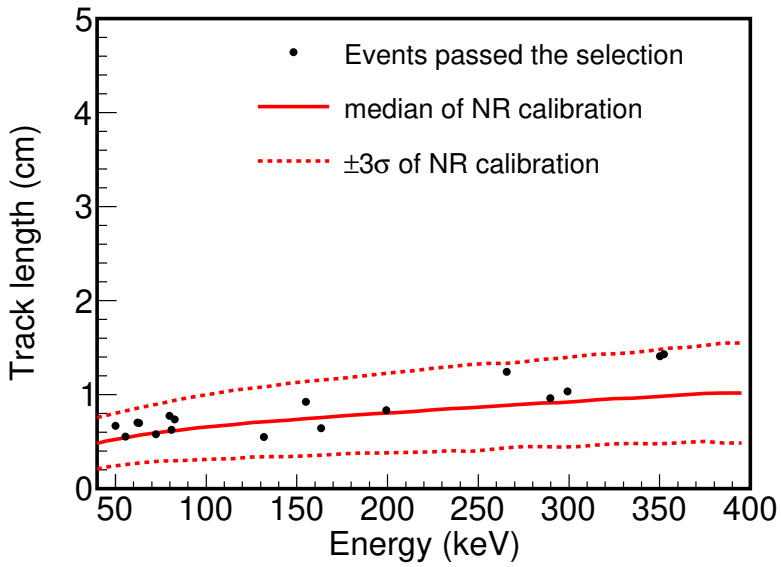

Figure 3.2.4: Length-Energy distribution after all event selections.

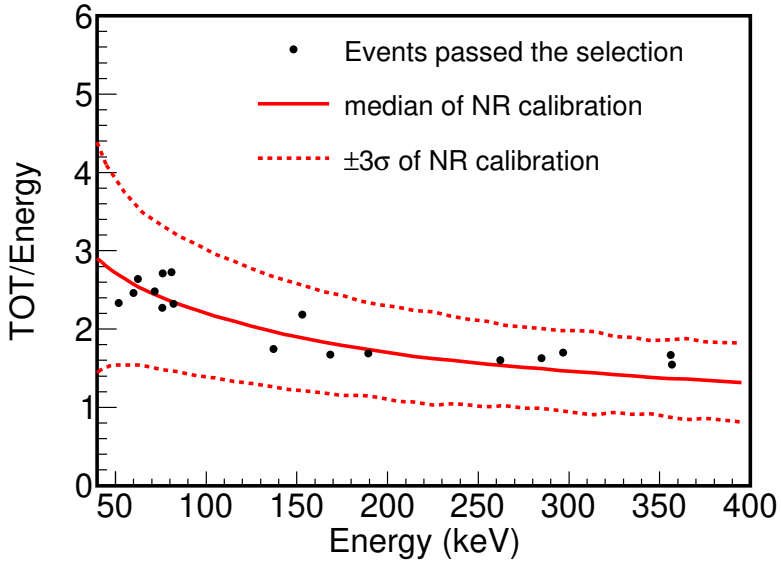

Figure 3.2.5: TOT-Energy distribution after all event selections.

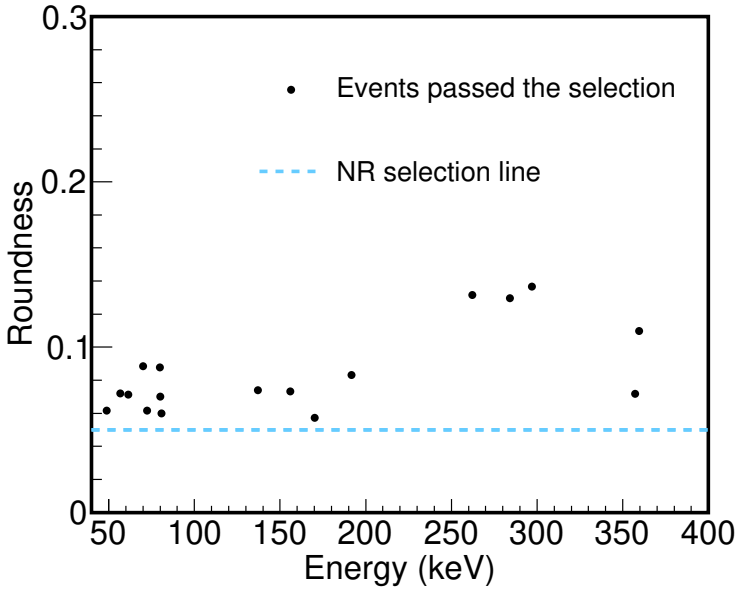

Figure 3.2.6: Roundness-Energy distribution after all event selections.

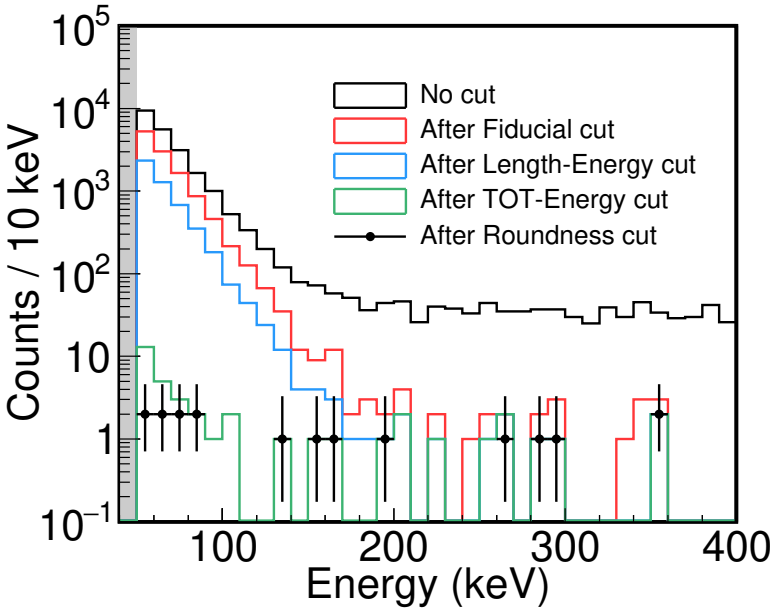

Figure 3.2.7: Energy spectra of the dark matter search at each selection step. The black, red, blue and green line are the original energy spectrum, the one after the Fiducial cut, Length-Energy cut and TOT-Energy cut, respectively. The black points with error bars are the final event sample after the Roundness cut.

Table 3.2.1: Remaining number of events in the energy region of 50-60 keV after each cut.

Cut criteria	Remaining number of events
No cut	9461
Fiducial cut	5291
Length-Energy cut	2325
TOT-Energy cut	13
Roundness cut	2

The energy spectrum unfolded with the nuclear-track detection efficiency is shown in Figure 3.2.8. The previous result of RUN14 using conventional μ-PIC is shown for reference. It is seen that the background rate was reduced by about factor 10 in the energy range of 50-100 keV from RUN14. The background study of RUN14 indicated that the main background are alpha particles radiated from the surface material of the conventional μ-PIC. Here it was demonstrated that the LAμ-PIC worked as expected to reduce the alpha-ray backgrounds. The remaining backgrounds will be discussed in Chapter 4.

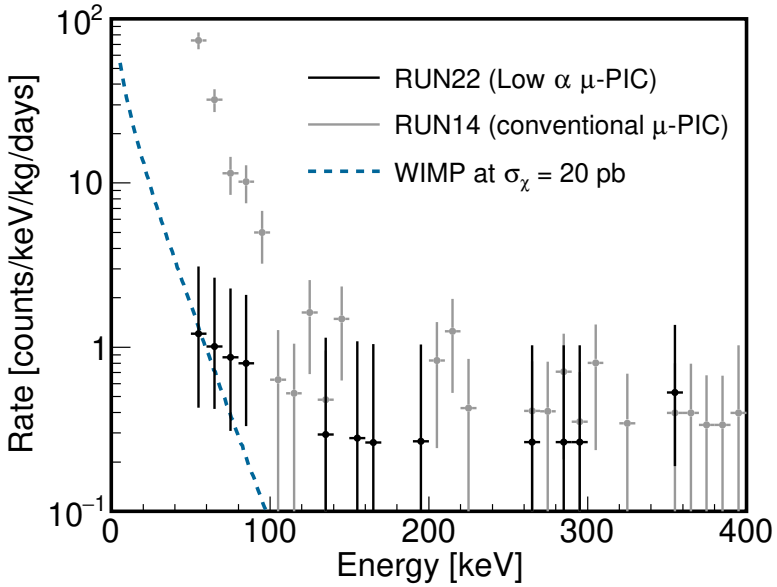

Figure 3.2.8: Final energy spectrum considering the detection efficiency. The black and gray dots with errors represent RUN22 (using the LAμ-PIC) and RUN14 (using the conventional μ-PIC), respectively. The blue dotted line shows the expected spectrum of the WIMP-nucleus scattering with the WIMP mass of m_χ = 100 GeV, the WIMP-proton cross section of σ_χ = 20 pb and the energy resolution of ϵ = 13.2%.

Figure 3.2.9 and 3.2.10 show the skymaps of the final sample on the detector coordinate

and the galactic coordinate, respectively. We calculated the $|\cos\theta_{\mathrm{cygnus}}|$ distribution for the energy region of 50-100 keV where the angle θ_{cygnus} is defined as the angle between the WIMP-wind direction and the measured direction of the recoil nucleus. Figure 3.2.11 shows the obtained $|\cos\theta_{\mathrm{cygnus}}|$ distribution binned into 2-bin for each energy range.

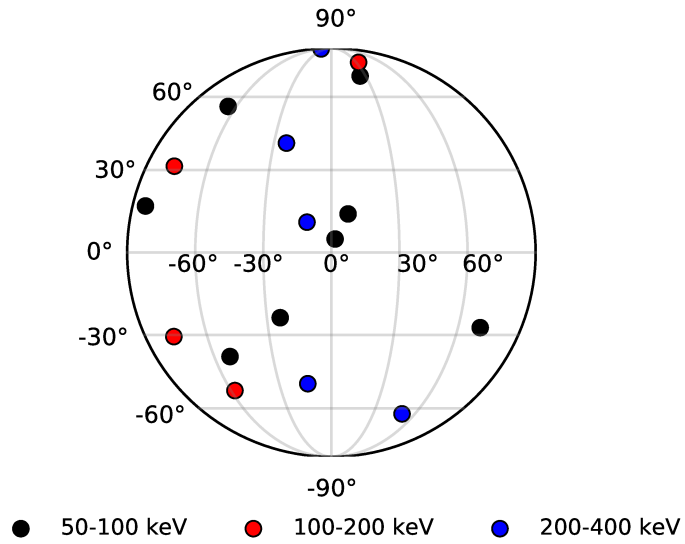

Figure 3.2.9: Skymap of the final sample on the detector coordinate. The x (y) axis is the azimuth angle ϕ_{azi} (the elevation angle θ_{ele}) defined in Figure 2.1.3. The black, red and blue points show the energy of 50-100 keV, 100-200 keV and 200-400 keV, respectively.

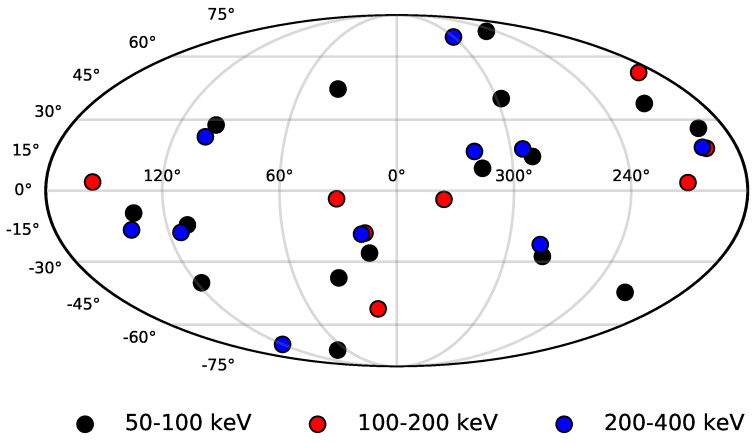

Figure 3.2.10: Skymap of the final sample on the galactic coordinate. The x (y) axis is the galactic longitude (the galactic latitude). The black, red and blue points show the energy of 50-100 keV, 100-200 keV and 200-400 keV, respectively. Reverse directions are also described due to not recognizing the head-tail of the nuclear tracks. The direction of the galactic center and the solar motion are (0,0) and (90,0), respectively.

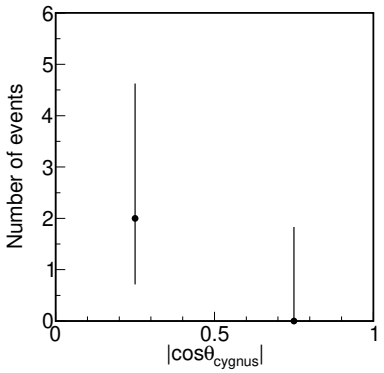

(a) 50-60 keV

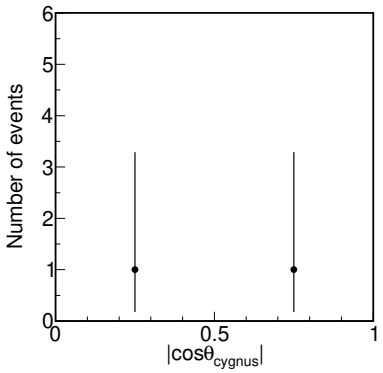

(b) 60-70 keV

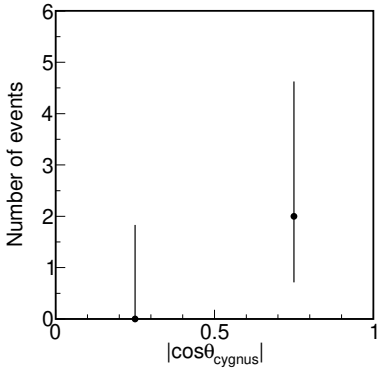

(c) 70-80 keV

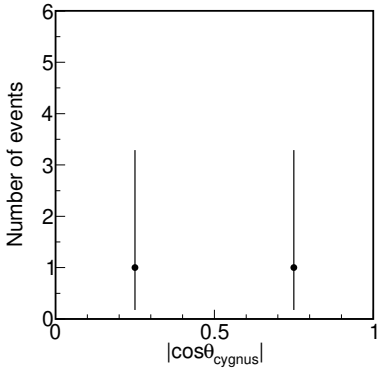

(d) 80-90 keV

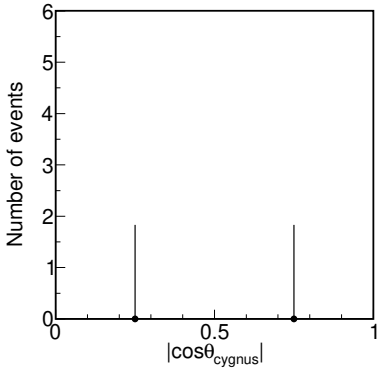

(e) 90-100 keV

Figure 3.2.11: Obtained $|\cos\theta_{\mathrm{cygnus}}|$ distribution for each energy range.

3.3 Systematic uncertainties

The measured cosθ distribution will be compared with the expected one in the directional analysis. The expected spectrum was calculated from Equation 1.4.15. Systematic errors associated with the astrophysical parameters and the detector response are discussed.

3.3.1 Systematic uncertainties from the astrophysical parameters

The observed astrophysical parameters are the local circular velocity or the laboratory velocity $V_{\rm lab}$, the escape velocity $v_{\rm esc}$ and the local WIMP density $\rho_{\rm DM}$. The canonical value of $V_{\rm lab}$ = 220 km/s, $v_{\rm esc}$ = 650 km/s and $\rho_{\rm DM}$ = 0.3 GeV/cm^3 were used in the directional analysis following the conventional direct search analysis. However, studies on these parameters indicated different values [25; 26; 28; 29; 30; 31]. The relative uncertainty of the expected rate from the observed astrophysical parameters were estimated as following. These uncertainties were not assigned in the directional analysis.

- Since the local circular velocity or the laboratory velocity $V_{\rm lab}$ depends on the model of the MW halo, it has a significant systematic uncertainty. Various models of MW halo indicate the local circular velocity from (220 ± 20) km s^{-1} to (279 ± 33) km s^{-1} [26]. The difference of the expected rate was estimated by the Monte Carlo simulation. The relative uncertainty of the expected rate was +52%.

- The recent RAVE survey has found the escape velocity to be $v_{\rm esc} = 533^{+54}_{-41}$ km s^{-1}(90% confidence level) assuming a smooth halo in equilibrium [27]. The uncertainty of the expected rate was obtained as −2.4% from the Monte Carlo simulation.

- The calculation of the local WIMP density also depends on the halo profile model. Recent works lead to the local densities in the range $\rho_{\rm DM}$ = (0.2 − 0.5) GeV cm^{-3} [28; 29; 30; 31]. The relative uncertainty of the expected rate varies −33% and +67% by the Monte Carlo simulation.

3.3.2 Systematic uncertainties from the detector response

Three sources of systematic uncertainties were considered on the detector response. Uncertainties on the energy resolution ϵ = 6.9 keV, the drift velocity $V_{\rm D}$ = 9.6 cm/μs and the angular resolution κ = 48 degree are discussed here.

- During the dark matter search, the energy resolution was monitored (see Figure 3.1.3). There was no time dependence and the standard deviation of energy resolution was 2.3%. The expected rate was estimated using Monte Carlo simulations taking account of the measured energy resolution with its uncertainty. The resulting uncertainty in the expected rate was less than 0.1%. This uncertainty was found to be negligible compared to that of the angular resolution discussed in the followings. No systematic uncertainty from this source was assigned in the directional analysis.

- The gas pressure was increased due to a leak of the vacuum vessel during the dark matter search (see Figure A.3). In order to confirm a coefficient of the fluctuation of the drift velocity, the gas pressure and the drift velocity every two weeks were monitored in a different run. The coefficient value was 8.4×10^{-2} cm/μs/Torr and gave +3.3% and -12% of the maximum uncertainty to the drift velocity. The expected $|\cos\theta_{\mathrm{cygnus}}|$ distribution was calculated by Monte Carlo simulations and the effect by the uncertainty of the drift velocity was considered. The uncertainty of the drift velocity does not change the total expected rate of 50-60 keV bin, while it affects the shape of the $|\cos\theta_{\mathrm{cygnus}}|$ distribution. The distribution was binned into 2-bin similar to the analysis procedures in Section 3.4. The systematic uncertainty of the expected rate in the $|\cos\theta_{\mathrm{cygnus}}|$ range of [0, 0.5] and [0.5, 1] are less than 0.2%. This uncertainty was found to be small compared to that of the angular resolution. No systematic uncertainty from this source was assigned in the directional analysis.

- The uncertainty associated with the angular resolution was studied. The systematic error of the angular resolution was +6.8% and −2.2% (see Figure 2.4.21). The signal $|\cos\theta_{\mathrm{cygnus}}|$ distribution was estimated using Monte Carlo simulations and a possible uncertainty of each bin was calculated. Here the distribution was binned into 2-bin similar to the analysis procedures described in Section 3.4. The resulting uncertainties of the expected rate were +6.4% and −7.8% in the $|\cos\theta_{\mathrm{cygnus}}|$ range of [0, 0.5], and +5.4% and −4.4% in the range of [0.5, 1]. This source makes the largest impact on the shape of $|\cos\theta_{\mathrm{cygnus}}|$ distribution. This systematic uncertainty was considered in the directional analysis described in Section 3.4.

Table 3.3.1: Systematic uncertainties of the expected rate for the dark matter mass m_χ = 100 GeV/c^2.

Source	Symbol	cosθ range	Relative uncertainty (%)
Laboratory velocity	V_{lab}	[0, 1]	+52
Escape velocity	v_{esc}	[0, 1]	−2.4
Local WIMP density	ρ_{DM}	[0, 1]	+67 − 33
Energy resolution	ϵ	[0, 1]	< 0.1
Drift velocity	V_{D}	[0, 0.5]	< 0.2
		[0.5, 1]	< 0.2
Angular resolution	κ	[0, 0.5]	+5.4 −2.2
		[0.5, 1]	+1.7 −4.2

3.4 Results

In order to obtain a possible anisotropic $|\cos\theta_{\mathrm{cygnus}}|$ distribution, a binned likelihood-ratio method was used [79; 80]. The minimized statistic value χ^2 was defined as,

$$\chi^2 = 2\sum_{i=0}^{n}\left[(N_i^{\mathrm{exp}} - N_i^{\mathrm{data}}) + N_i^{\mathrm{data}}\ln\left(\frac{N_i^{\mathrm{data}}}{N_i^{\mathrm{exp}}}\right)\right] + \alpha^2, \tag{3.4.1}$$

where the subscript i is the bin number of $|\cos\theta_{\mathrm{cygnus}}|$ distribution, N_i^{data} is the measured number of events and N_i^{exp} is the expected number of events. A nuisance parameter α $(= \xi/\sigma_\kappa)$ was introduced to consider the systematic error of the angular resolution σ_κ [81]. A possible angular-resolution shift is ξ.

The expected event number N_i^{exp} is given by,

$$N_i^{\mathrm{exp}} = A(\sigma_{\chi-p}) \cdot N_i^{\mathrm{MC}}(m_\chi, \epsilon, \kappa + \xi). \tag{3.4.2}$$

The quantity N_i^{MC} was obtained by a Monte Carlo simulation. It depends on the WIMP mass m_χ, the energy resolution ϵ and the angular resolution κ. The amplitude of the dark matter signal A depends on the WIMP-proton cross section $\sigma_{\chi-p}$. In the calculation of N_i^{MC}, the astrophysical parameters and nuclear parameters listed in Table 3.4.1 were used. In addition the nuclear quenching factor and the detector responses were considered. Here the detector response includes the energy resolution ϵ, the detection efficiency, the direction-dependent efficiency and the angular resolution κ described in Section 2.4.2, 2.4.5, 2.4.7 and 2.4.8.

Table 3.4.1: Astrophysical parameters, nuclear parameters, and detector responses used for the directional analysis.

WIMP velocity distribution	Maxwellian
Laboratory velocity	$V_{\mathrm{lab}} = 220$ km/sec
Escape velocity	$v_{\mathrm{esc}} = 650$ km/sec
Local halo density	$\rho_{DM} = 0.3$ GeV/c^2/cm^3
Spin factor of ^{19}F	$\lambda^2 J(J+1) = 0.647$
Energy resolution	$\epsilon = 6.9 \pm 1.1$ keV
Angular resolution at 50-100 keV	$\kappa = 48^{+6.8}_{-2.2}$ degree
Detection efficiency	Figure 2.4.13
Direction-dependent efficiency	Figure 2.4.17

The measurement data was divided into 10 keV/bin considering the energy resolution. Since each energy bin had a low statistics, the measured $|\cos\theta_{\mathrm{cygnus}}|$ were binned into 2-bin. Hence the maximum bin number n in Equation 3.4.1 is 1. Expected signal was

binned in the same way. The binned measurement data and Monte Carlo data are shown in Figure 3.2.11 and 3.4.1, respectively.

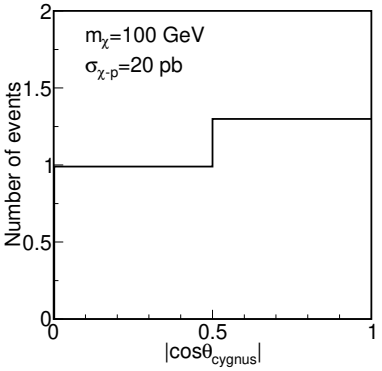

(a) 50-60 keV

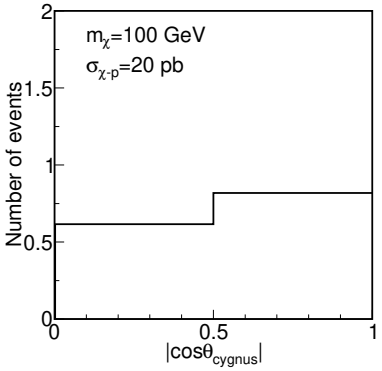

(b) 60-70 keV

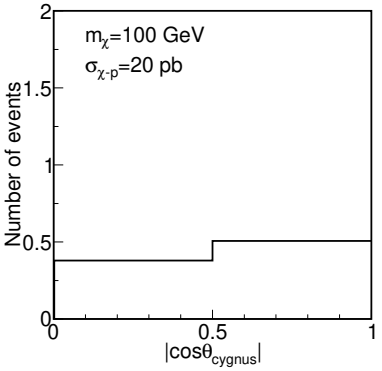

(c) 70-80 keV

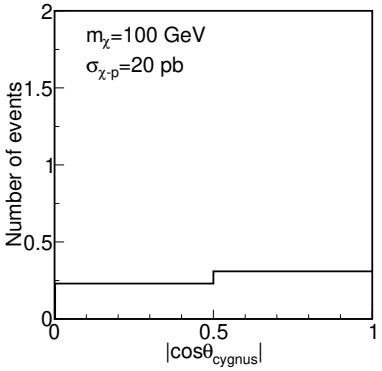

(d) 80-90 keV

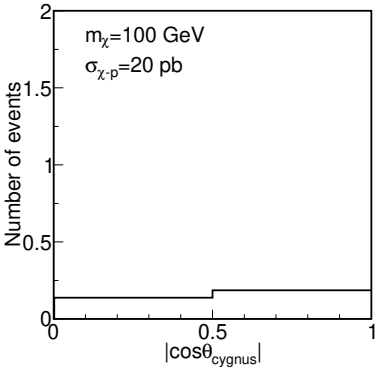

(e) 90-100 keV

Figure 3.4.1: Binned $|\cos\theta_{\rm cygnus}|$ distribution of the Monte Carlo simulation where the WIMP mass m_χ and the WIMP-proton cross section are 100 GeV and 20 pb, respectively. The energy resolution ϵ = 6.9 keV and the angular resolution κ = 48 degree, the detection efficiency and the direction-dependent efficiency were considered.

Here we first explain the analysis method with 50-60 keV bin as a region of interest for

the 100 GeV of WIMP mass. The measurement data was fitted by minimizing χ^2. The WIMP-proton cross section $\sigma_{\chi-p}$ and the nuisance parameter α were treated as fitting parameters. The calculated χ^2 values changing the WIMP-proton cross section and the angular resolution were shown in Figure 3.4.2. The minimum χ^2 value was 3.3 where $\sigma_{\chi-p}$ and α were 18.5 pb and 0.12, respectively. Figure 3.4.3 shows the measured $\cos\theta_{\mathrm{cygnus}}$ distribution in the energy region of 50-60 keV along with the simulation using best-fit values.

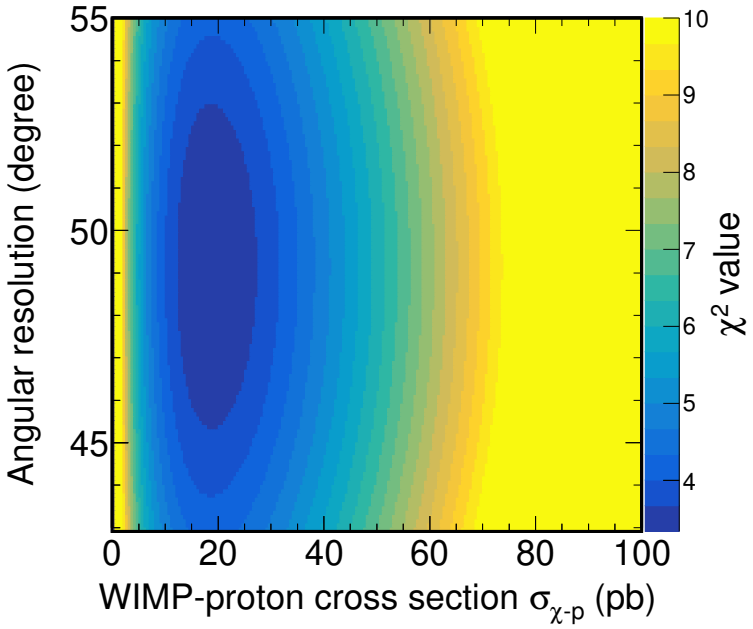

Figure 3.4.2: Calculated χ^2 values changing the WIMP-proton cross section and the angular resolution.

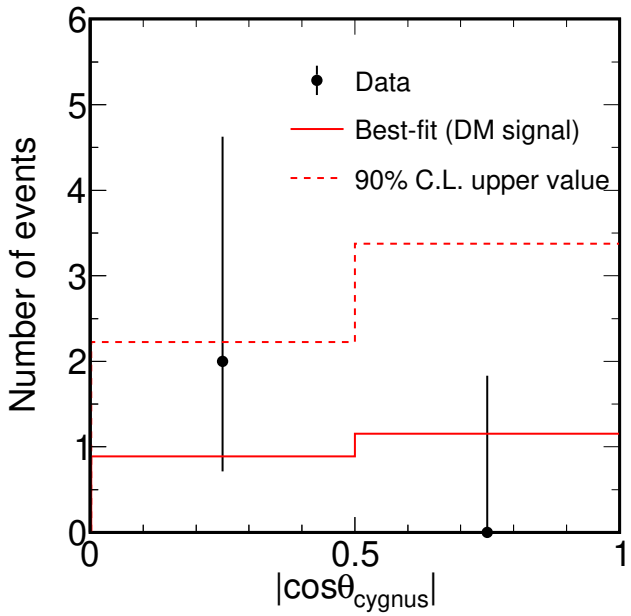

Figure 3.4.3: The $|\cos\theta_{\mathrm{cygnus}}|$ distribution in the energy range of 50-60 keV. The black points show observed data. The solid and dotted red lines are the simulated distribution using best-fit values and excluded values of 90 % confidence level, respectively.

In order to calculate the p-value, we made a χ^2 distribution of an isotropic BG model and an anisotropic WIMP model from dummy samples. One thousand dummy samples were produced by Monte Carlo simulations and χ^2 value of each dummy sample was calculated. The dummy samples were produced by the following methods:

1. Total event number of one dummy sample was randomly determined from the poisson distribution with mean=$\sum_i N_i^{\mathrm{data}}$.

2. The number of event N_i^{dummy} of the isotropic BG model was obtained by the uniform distribution of $|\cos\theta_{\mathrm{cygnus}}|$. The number of event N_i^{dummy} of the anisotropic WIMP model was obtained by the signal Monte Carlo simulation, when a possible angular-resolution shift ξ was determined from the gaussian distribution with mean=0 and sigma=σ_κ considering the systematic error of the angular resolution.

3. A χ^2 was calculated applying the same analysis where the measurement data N_i^{data} was replaced by N_i^{dummy}.

4. These processes were repeated 1000 times and the χ^2 distribution of the isotropic BG model and the anisotropic WIMP model were obtained.

The calculated χ^2 distribution of the isotropic BG model and the anisotropic WIMP model were shown in Figure 3.4.4. The black line shows the χ^2 distribution of the isotropic BG model. The red dotted line shows the χ^2 value of the measurement data. The calculated p-value was 3.3%. The blue line shows χ^2 distribution of anisotropic WIMP

model. Since these distributions are very similar to each other, we cannot claim the detection of dark matter with sufficient significance from the observed data. This is a natural result because of the large statistic error and the small expected anisotropic ratio.

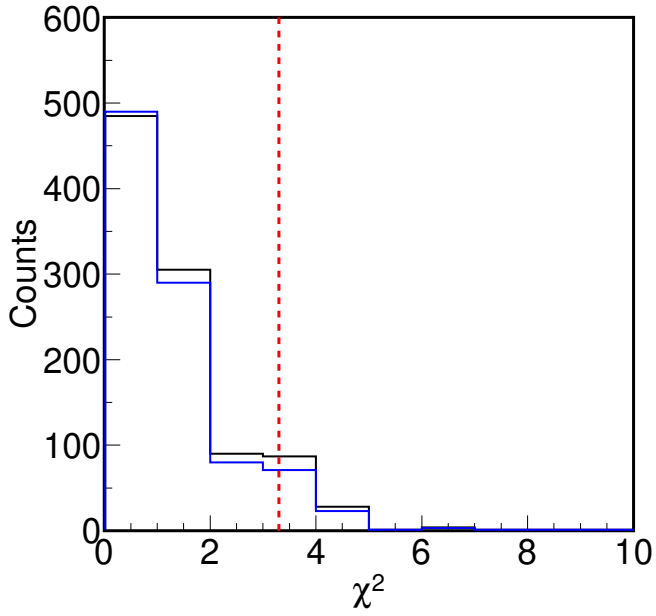

Figure 3.4.4: Calculated χ^2 distribution. The black and blue lines are isotropic BG model and anisotropic WIMP model, respectively. The red dotted line shows the measurement χ^2 value.

Since no significant amplitude was found, a 90% confidence level (C.L.) upper limit was set on the Spin-Dependent cross section. The likelihood ratio $\mathcal{L}$ defined as

$$\mathcal{L} = \exp\left(-\frac{\chi^2(\sigma_{\chi-p}) - \chi^2_{\rm min}}{2}\right), \tag{3.4.3}$$

where $\chi^2(\sigma_{\chi-p})$ and $\chi^2_{\rm min}$ are calculated χ^2 value by varying $\sigma_{\chi-p}$ and the minimum χ^2 value, respectively. The 90% C.L. upper limit of the WIMP-proton cross section $\sigma^{\rm limit}_{\chi-p}$ was obtained using the relation defined by,

$$\frac{\int_0^{\sigma^{\rm limit}_{\chi-p}} \mathcal{L} d\sigma_{\chi-p}}{\int_0^{\infty} \mathcal{L} d\sigma_{\chi-p}} = 0.9. \tag{3.4.4}$$

The calculated likelihood ratio is shown in Figure 3.4.5. The 90% C.L. upper limit on the Spin-Dependent cross section was obtained as,

$$\sigma^{\rm limit}_{\chi-p} = 50 \text{ pb at } 100 \text{ GeV}. \tag{3.4.5}$$

The calculated $\cos\theta_{\rm cygnus}$ distribution using the 90% C.L. upper value is also shown in

Figure 3.4.3 as the red dotted line along with the measurement data.

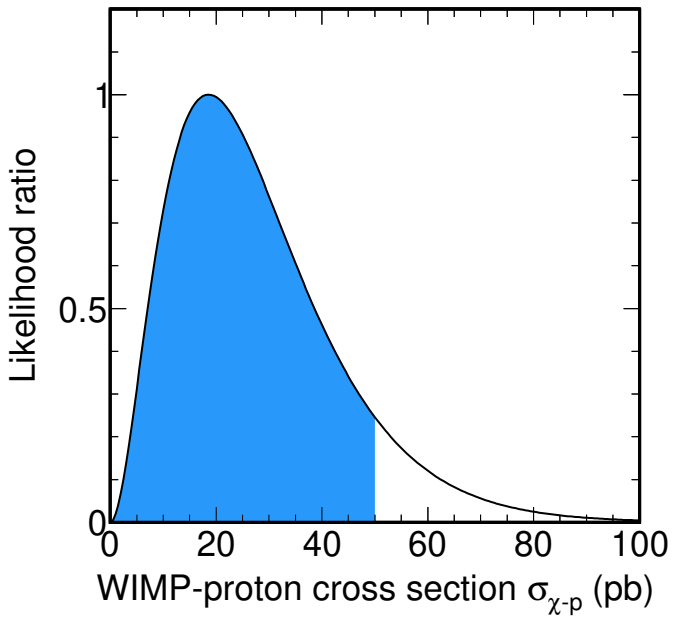

Figure 3.4.5: Likelihood ratio distribution. The blue area corresponds to 90% of the total area. The obtained 90% C.L. upper limit value of the WIMP-proton cross section $\sigma_{\chi-p}^{\mathrm{limit}}$ is 50 pb in this case.

90% C.L. upper values of the WIMP-proton cross section $\sigma_{\chi-p}^{\mathrm{limit}}$ were calculated changing the energy bin and the minimum cross-section was adopted. The most dominant energy bin contributed the upper limit was the 50-60 keV bin because of the highest expected rate (Figure 3.2.8). Figure 3.4.6 shows the 90% upper limit of the Spin-Dependent WIMP-proton cross section as a function of the WIMP mass. This result marked a new best sensitivity record of a Spin-Dependent WIMP search with the direction-sensitive method. The sensitivity was improved by about 15 times compared to the previous result of NEWAGE (RUN14). This improvement owed to the surface background reduction of the μ-PIC detector.

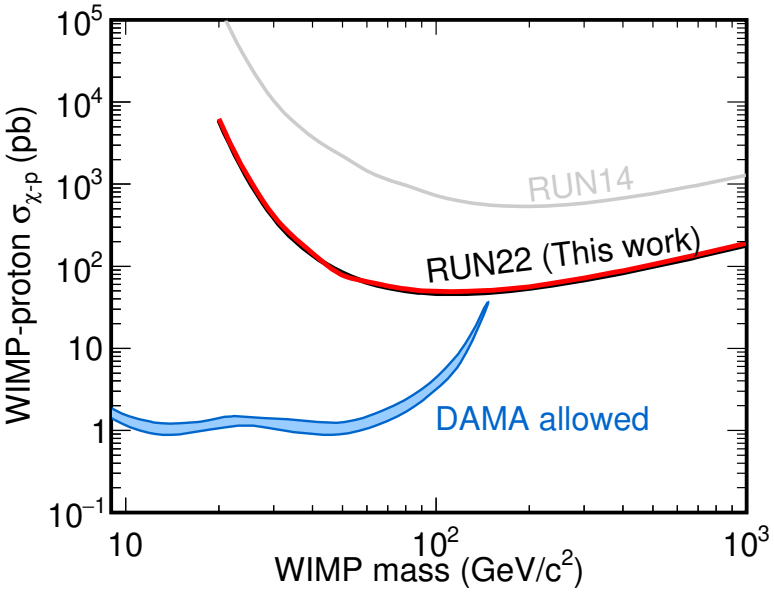

Figure 3.4.6: Upper limits at a 90% confidence level of the Spin-Dependent cross section as a function of the WIMP mass. The red thick solid line is the result of the directional method in this work. The black solid line is the result of the conventional method for reference. The gray solid line RUN14 is the limits of the previous result. Allowed region from DAMA/LIBRA experiment [62] is shown by the blue area.

Chapter 4

Discussion

The WIMP-nucleon cross section limit by the direction-sensitive method was improved by factor 15 with the measurement using the LAμ-PIC. However, more than two orders of magnitude of improvement is required in order to cover the entire DAMA region. Since the sensitivity is limited by the remaining backgrounds, it is important to study the sources of these backgrounds. In this chapter, we estimate the origin of the remaining backgrounds using Geant4 simulations. In addition, the discovery potential is discussed when these backgrounds are eliminated as future prospects.

In Section 4.1, the background candidates are introduced. In Section 4.2, contributions of cosmic-ray muons, ambient gamma-rays and neutrons as the external backgrounds are discussed. In Section 4.3, we discuss the internal backgrounds coming from the decay of radons and the LAμ-PIC surface. It should be noted that the background energy spectra of both considering Roundness cut and not considering that were calculated since we don't know the Roundness cut efficiency, completely. Finally, future prospects are discussed in Section 4.5.

4.1 Background candidates

The background candidates are classified into two categories, namely external backgrounds and internal backgrounds. External backgrounds are cosmic-ray muons, ambient gamma-rays and neutrons coming from outside of the vessel. Internal backgrounds are gamma-rays, beta-rays and alpha-rays emitted from radioactive contaminations within the detector components. Figure 4.1.1 schematically shows these background candidates.

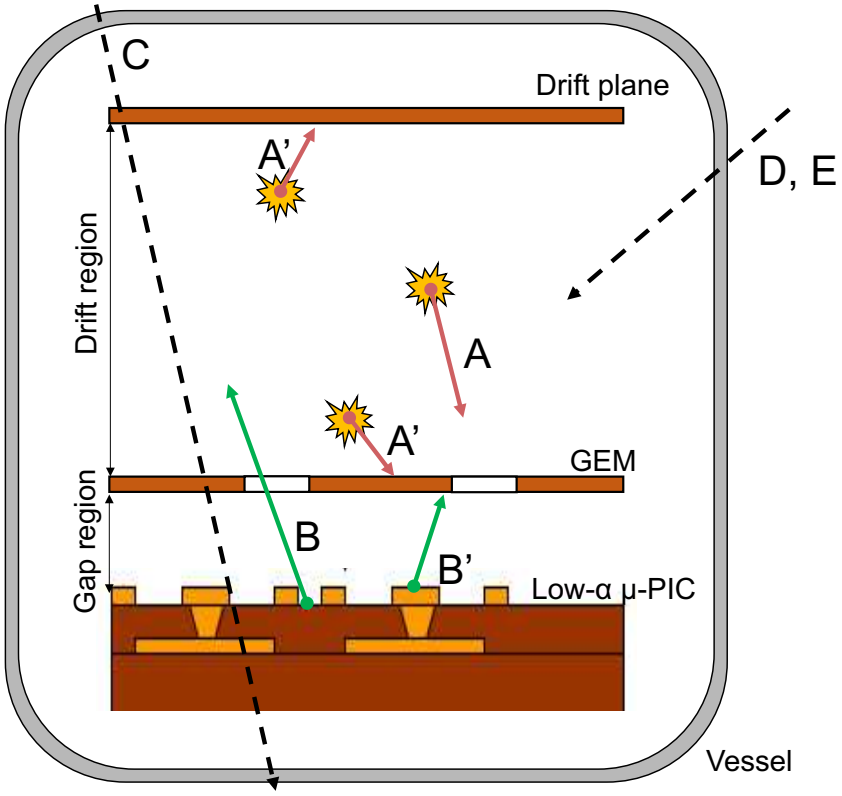

Figure 4.1.1: Candidates of external and internal backgrounds. The solid (dotted) arrow indicates internal (external) backgrounds. The symbol **A** (**A′**) is an alpha-ray emitted from decays of radons with long (short) track length. The symbol **B** (**B′**) is an alpha-ray coming from the LAμ-PIC surface with a long (short) track length. The symbol **C**, **D** and **E** are cosmic-ray muons, ambient gamma-rays and ambient neutrons coming from outside of the vessel, respectively.

4.2 External backgrounds

The important external backgrounds are ambient gamma-rays and neutrons from rocks in the mine. Although cosmic-ray muons also be one of the candidates of external backgrounds, its contribution is negligible compared with ambient gamma-rays and neutrons. The expected rate of these external backgrounds are calculated below.

4.2.1 Cosmic-ray muons

The NEWAGE-0.3b" detector is located in the Laboratory B of the Kamioka Observatory for shielding cosmic-ray muons. Since the facility is located under the peak of Mt. Ikenoyama, with 1000 m of rock, or 2700 m-water-equivalent, the cosmic-ray muons with the energy less than 1.3 TeV cannot reach the laboratory. The flux of the cosmic-ray muons at Kamioka Observatory is about $6{\times}10^{-8}$ cm^{-2}s^{-1}sr^{-1} [82]. The expected rate passing through the fiducial volume of the μ-TPC was calculated to be about 6 counts/day. Assuming that the muon rejection power is same to that of electron, the rate of detected muon is the order of 10^{-4} counts/kg/days above 50 keV. Therefore muon background is

negligible.

4.2.2 Ambient gamma-rays

Ambient gamma-rays are mainly produced by the decay of natural radioactive isotopes such as ^{40}K, U-chain and Th-chain in the rock. The decay process and the energy of emitted particles are summarized in Figure 4.2.1. The flux of ambient gamma-rays in Laboratory B was measured with a $5 \times 5 \times 1\text{cm}^3$ CsI(Tl) scintillator in 2008 [83]. From the measured spectrum, the spectrum from the decay of ^{40}K, U-chain and Th-chain was unfolded. Figure 4.2.2 shows the estimated flux from ^{40}K, U-chain and Th-chain.

Using this spectrum, we simulated the expected rate of the ambient gamma-rays. In the simulation, gamma-rays were generated on the spherical surface with a radius of 100 cm. The incident direction was weighted with a cosθ distribution in order to produce an isotropic flux. The angle θ is defined as the zenith angle on the spherical surface. The simulated results are shown in Figure 4.2.3. The expected energy spectra after all cuts (red points) and without roundness-cut (blue points) are shown. The expected rate in the energy range of 50-60 keV was $(1.4 \pm 1.4) \times 10^{-1}$ counts/keV/kg/days (summarized in Table 4.2.1).

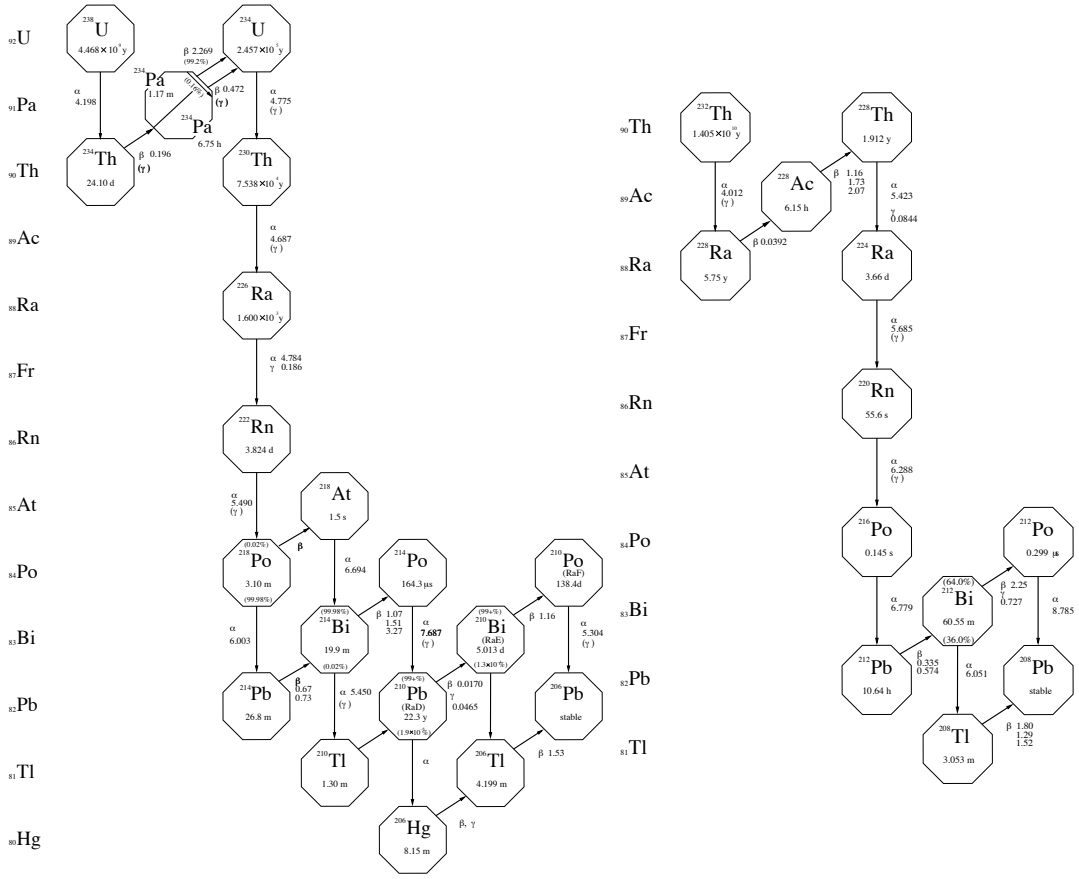

Figure 4.2.1: Decay chains of ^{238}U and ^{232}Th [84].

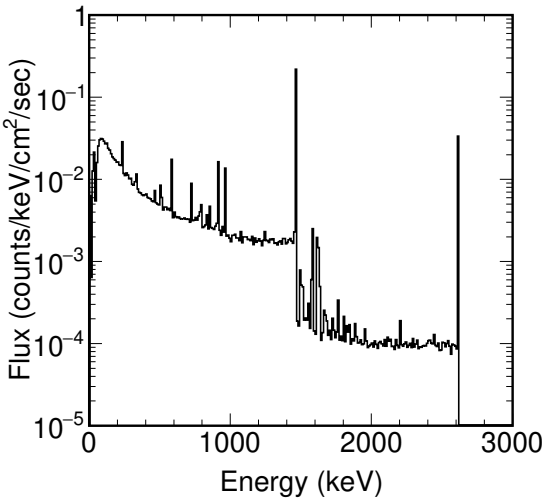

Figure 4.2.2: Estimated ambient gamma-ray flux from the decay of ^{40}K, U-chain and Th-chain [83].

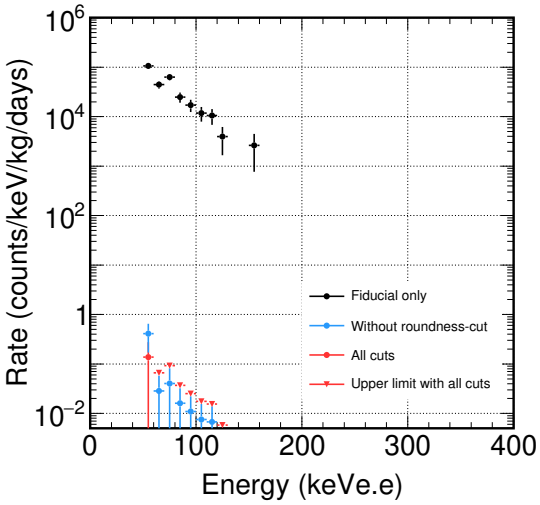

Figure 4.2.3: Expected energy spectra by the ambient gamma-rays. The black points are expected rate in the fiducial volume. The red (blue) points with error bars are the energy spectra taking account of the gamma-ray rejection power with all cuts and all but the roundness cut. The red triangle points indicate upper limits.

Table 4.2.1: Summary of the expected rate of ambient gamma-ray background. The values in brackets show errors (%).

Expected rate by ambient gamma-rays (counts/keV/kg/days) with error (%)			
	50-60 keV	60-100 keV	100-400 keV
Fiducial only	1.1×10^{5} (11)	3.7×10^{4} (9.4)	9.6×10^{2} (21)
without Roundness-cut	4.1×10^{-1} (59)	2.4×10^{-2} (56)	6.2×10^{-4} (61)
All cuts	1.4×10^{-1} (100)	$< 7.7 \times 10^{-3}$	

4.2.3 Ambient neutrons

The ambient neutrons are mainly generated by the (α, n) reactions of ^{238}U and ^{232}Th series, the spontaneous fission of ^{238}U and the spallation by the cosmic-ray muon. The ambient neutron flux in Laboratory B was measured using a ^{3}He proportional counter as described in Ref. [85]. An energy spectrum was also predicted. The simulated spectrum of ambient neutrons produced by (α, n) reactions and spontaneous fission is shown in Figure 4.2.4.

We estimated the expected rate by the ambient neutron in the fiducial volume by a Geant4 simulation. In the simulation, neutrons were generated using the same method used for the ambient gamma-rays. The obtained spectrum is shown in Figure 4.2.5. The actual expected rate is calculated by considering the nuclear-detection efficiency described in Section 2.4.5. The expected spectra after all cuts and without roundness-cut are described in Figure 4.2.5. The expected rate in the energy range of 50-60 keV is $(3.1 \pm 0.8) \times 10^{-2}$ counts/keV/kg/days (summarized in Table 4.2.2).

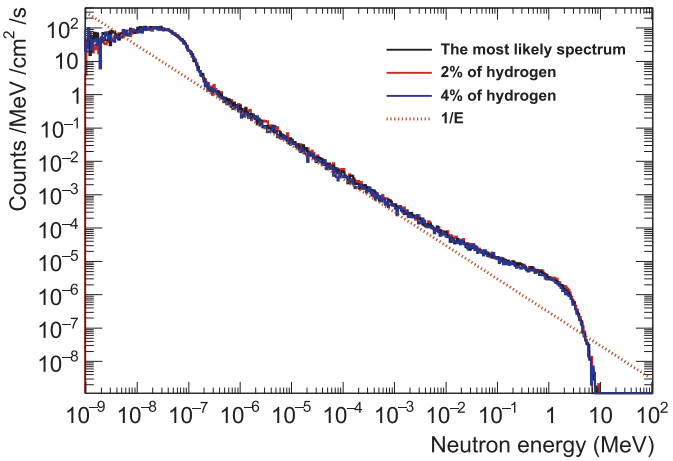

Figure 4.2.4: Simulated spectrum of ambient neutrons produced by (α, n) reactions and spontaneous fission in Laboratory B [85].

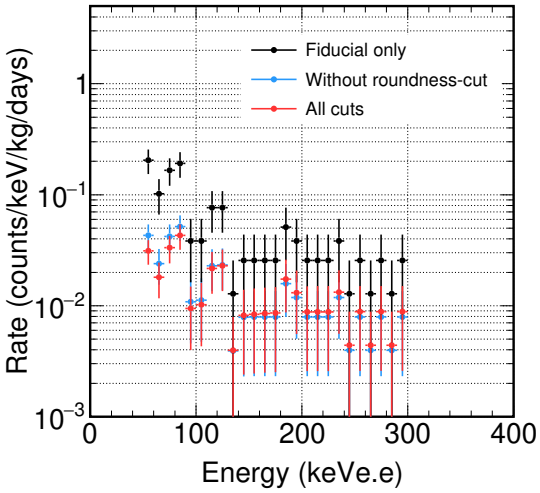

Figure 4.2.5: Expected energy spectra by ambient neutrons. The black points are expected count rate in the fiducial volume. The red (blue) points with error bars are the ones taking account of the nuclear-detection efficiency described in Section 2.4.5 with all cuts (without roundness-cut).

Table 4.2.2: Summary of the expected rate of ambient neutron background. The values in brackets show errors (%).

Expected rate of ambient neutrons (counts/keV/kg/days) with error (%)			
	50-60 keV	60-100 keV	100-400 keV
Fiducial only	2.0×10^{-1} (25)	1.2×10^{-1} (16)	2.1×10^{-2} (14)
without Roundness-cut	4.3×10^{-2} (25)	3.2×10^{-2} (16)	6.4×10^{-3} (14)
All cuts	3.1×10^{-2} (25)	2.6×10^{-2} (16)	6.7×10^{-3} (14)

4.2.4 Summary of external backgrounds

The total external backgrounds are summarized in Table 4.2.3.

Table 4.2.3: Summary of the total external backgrounds. The values in brackets show errors (%).

Expected rate of the total external background (counts/keV/kg/days) with error (%)			
	50-60 keV	60-100 keV	100-400 keV
Fiducial only	1.1×10^{5} (11)	3.7×10^{4} (9.4)	9.6×10^{2} (21)
Without roundness-cut	4.5×10^{-1} (53)	5.6×10^{-2} (26)	7.0×10^{-3} (14)
All cuts	1.7×10^{-1} (82)	2.6×10^{-2} (16)	6.7×10^{-3} (14)

4.3 Internal backgrounds

Radioactive contaminations within the detector components are well-known background sources in rare event measurements. Dominant natural radioactive isotopes contaminated in most of the materials are ^{238}U, ^{232}Th and ^{40}K. These radioactive contaminations emit γ-rays, β-rays and α-rays. In our case, γ-rays and β-rays were rejected with a rejection power of 1.3×10^{-6} as discussed in Section 2.4.6, but α-rays cannot be discriminated from nuclear recoils around 50 keV. Several decays in the U-chain and the Th-chain emit α-rays as shown in Figure 4.2.1. These radioactive isotopes can be contaminated in most of the material in the detector components such as metal, plastic and glass fiber. In addition, radons in U-chain and Th-chain emanate from the material as gas. Therefore, radon and radon progeny, which are the isotopes below radon shown in Figure 4.2.1, might exist not only in the detector components but also in the gas volume. Although α particles emitted from the U-chain and Th-chain have an initial energy of more than 4 MeV, they sometimes deposit only their partial energies in the detection volume and make background events around 50 keV. Contributions of these backgrounds to the measured energy spectrum are discussed in the following sections.

4.3.1 Radon backgrounds

Detector materials may contain some amount of ^{238}U and ^{232}Th. Radioactive noble gases of ^{222}Rn and ^{220}Rn are generated in the ^{238}U and ^{232}Th decay series, respectively. Half-lives of ^{222}Rn and ^{220}Rn are 3.82 days and 55.6 s, respectively. A gas circulation system with cooled charcoal was installed NEWAGE-0.3b" detector and it is effective for removing ^{222}Rn. On the contrary, because of the short half-life, it is not effective for ^{220}Rn. Radons and these daughter nucleus diffused in the gas volume generate alpha particles and they can be backgrounds.

During the dark matter search, the peak spectrum of alpha particles generated by radon backgrounds was observed around 6 MeV. Total measured spectrum and the time dependency of the rate are shown in Figure 4.3.1 and 4.3.2. In order to estimate the amount of ^{222}Rn and ^{220}Rn in the gas volume, we simulated the energy spectrum by these radons using a Geant4 simulation.

^{222}Rn and ^{220}Rn decay to the daughter nuclei of ^{218}Po and ^{216}Po with emissions of alpha-rays. More than 90% of the daughter nuclei are known to be positively charged [86],

and considered to drift to the drift plane where negative high voltage was applied. Since the half-life of ^{218}Po and ^{216}Po are longer than the typical drift time of several micro seconds, they are considered to stick to the drift plane and decays in the place. Thus, the probability that alpha particles from ^{218}Po and ^{216}Po emitted into the detection region of μ-TPC is halved; i.e. the other half goes into the drift plane. The daughter nucleus of ^{218}Po and ^{216}Po decay on the drift plane and the probability is halved as well. The properties of emitted alpha particles from radons are summarized in Table 4.3.1 and 4.3.2.

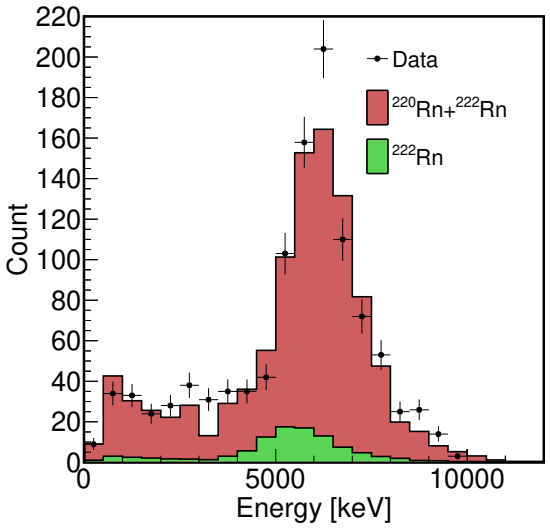

Figure 4.3.1: Observed and simulated spectra of alpha particles generated by radon decays. The black dots are the measurement data. The green histogram represents simulated spectrum of ^{222}Rn decay. The red histogram is sum of ^{222}Rn and ^{220}Rn.

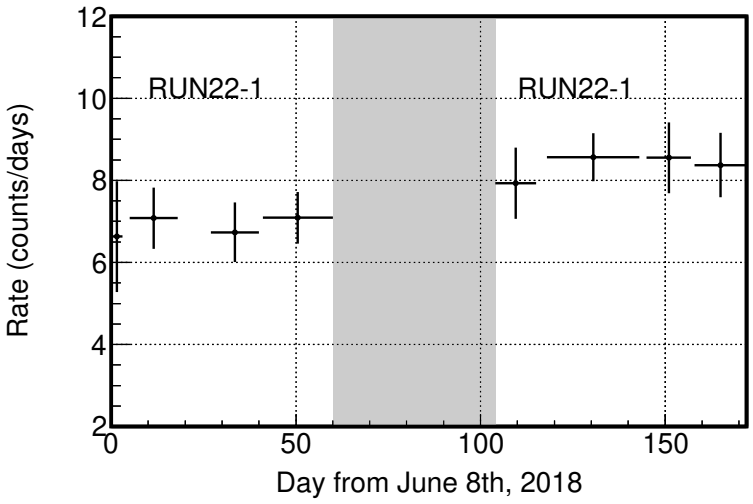

Figure 4.3.2: Time dependence of the radon background rate in the energy region of 3.5-8.5 MeV.

Table 4.3.1: Properties of emitted alpha particles from the decay chain of ^{222}Rn.

Isotope	^{222}Rn	^{218}Po	^{214}Po
Energy of alpha ray (MeV)	5.490	6.003	7.687
Branching ratio (%)	100	99.98	99.98
Probability of entering into the gas (%)	100	50	50

Table 4.3.2: Properties of emitted alpha particles from the decay chain of ^{220}Rn.

Isotope	^{220}Rn	^{216}Po	^{212}Bi	^{212}Po
Energy of alpha ray (MeV)	6.288	6.779	6.051	8.785
Branching ratio (%)	100	100	36.0	64.0
Probability of entering into the gas (%)	100	50	50	50

We simulated the energy spectrum from alpha particles generated in the decay chains of ^{222}Rn and ^{220}Rn considering the properties above. In order to estimate the amount of ^{222}Rn and ^{220}Rn, we compared the measured spectrum with simulated spectrum assuming various abundance ratio of ^{222}Rn and ^{220}Rn, and various energy resolution. The most likely spectrum is shown in Figure 4.3.1. The contents of ^{222}Rn and ^{220}Rn were $(5.3 \pm 2.1) \times 10^{-1}$ mBq/m^3 and 5.7 ± 0.3 mBq/m^3, respectively.

Moreover, we simulated the rate of radon backgrounds in the low energy region of 50-400 keV using the amounts of radon obtained above by a Geant4 simulation. The simulated spectrum of ^{222}Rn and ^{220}Rn are shown in Figures 4.3.3 and 4.3.4 along with all cuts (red points) and without roundness-cut (blue points), respectively.

The spectra with all cuts and without roundness-cut have a cut-off around 300 keV. This is because the Length-Energy cut effectively discriminates alpha-rays from carbon and fluorine nuclei at energy of more than 300 keV. Since the alpha backgrounds decaying near the center of the detection volume (**A** in Figure 4.1.1) have long track lengths, they are removed by the Length-Energy cut. The dominant events contained in the spectra with all cuts and without roundness-cut are alpha-rays from the decays around the drift plate and the GEM (**A′** in Figure 4.1.1). These events stop on the drift plate and the GEM and have short track length. Therefore they can pass through the Length-Energy cut. The roundness-cut is effective for events with a short drift length or small z. Hence the roundness-cut removes events around the GEM and the expected rate with all cuts is about half of the one without roundness-cut. The calculated background rates from radons are summarized in Table 4.3.3.

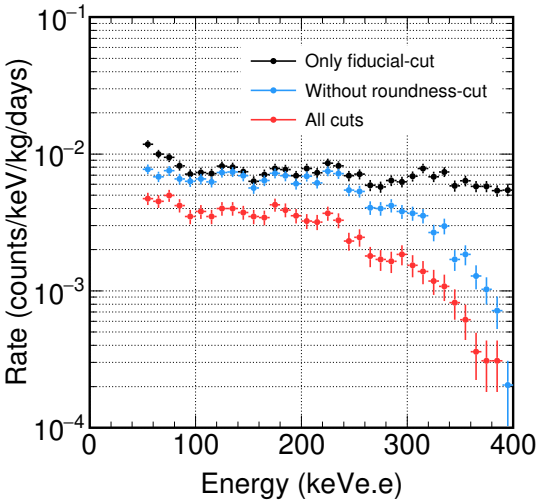

Figure 4.3.3: Expected energy spectra by ^{222}Rn. The black points are the expected rate in the fiducial volume. The red (blue) points indicate the spectrum after all cuts (without roundness-cut).

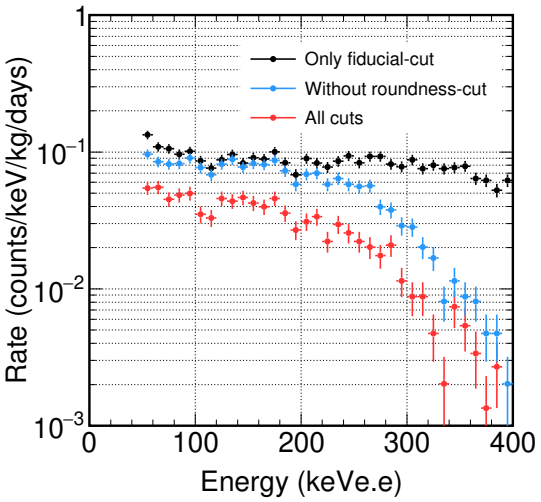

Figure 4.3.4: Expected energy spectra by ^{220}Rn. The black points are the expected rate in the fiducial volume. The red (blue) points indicate the spectrum after all cuts (without roundness-cut).

Table 4.3.3: Summary of the expected rate of ^{222}Rn and ^{220}Rn backgrounds. The values in brackets show errors (%).

Expected rate of ^{222}Rn (counts/keV/kg/days) with error (%)			
	50-60 keV	60-100 keV	100-400 keV
Fiducial only	1.2×10^{-2} (40)	8.7×10^{-3} (20)	6.9×10^{-3} (7.5)
Without roundness-cut	7.7×10^{-3} (41)	6.8×10^{-3} (20)	4.7×10^{-3} (8.3)
All cuts	4.7×10^{-3} (41)	4.3×10^{-3} (21)	2.3×10^{-3} (8.8)
Expected rate of ^{220}Rn (counts/keV/kg/days) with error (%)			
Fiducial only	1.3×10^{-1} (8.6)	1.0×10^{-1} (4.7)	8.1×10^{-2} (1.9)
without Roundness-cut	9.6×10^{-2} (9.7)	8.5×10^{-2} (5.1)	4.8×10^{-2} (2.4)
All cuts	5.5×10^{-2} (12)	5.0×10^{-2} (6.3)	2.3×10^{-2} (3.3)
Total expected rate (counts/keV/kg/days) with error (%)			
Fiducial only	1.5×10^{-1} (8.6)	1.1×10^{-1} (4.6)	8.8×10^{-2} (1.8)
without Roundness-cut	1.0×10^{-1} (9.5)	9.2×10^{-2} (5.0)	5.2×10^{-2} (2.3)
All cuts	5.9×10^{-2} (12)	5.4×10^{-2} (6.0)	2.5×10^{-2} (3.1)

4.3.2 Surface α-rays

We measured the alpha-ray emission rate of the LAμ-PIC using an UltraLo-1800 low-background α-ray counter made by XIA LLC [87]. The analysis method of the alpha rays was established by the XMASS group [88]. This detector can measure the contamination of ^{210}Pb and ^{210}Po in the sample with a high sensitivity. Also from the shape of the energy spectrum, we can determine whether the radioactive contaminations are on the surface of the sample or inside. Since alpha rays from ^{210}Po decay has 5.3 MeV, we defined 4.8 MeV $< E <$ 5.8 MeV as the surface component. The measured emission rate of the surface component was $(2.1 \pm 0.5) \times 10^{-4}$ alpha/cm^2/hr [71]. A candidate for the origin of the surface background was embedded daughter nuclei of radon decay in the air. If the material was placed in an atmosphere with a typical radon concentration for several days, this level of radioactivity could be explained [89].

Using the measured emission rate, we simulated the expected spectrum from the LAμ-PIC background. Figure 4.3.5 shows the obtained spectrum by a Geant4 simulation. The Length-Energy cut removed a large part of the events passing through GEM hole (**B** in Figure 4.1.1). Remaining backgrounds are so-called gap events between the LAμ-PIC and the GEM (**B′** in Figure 4.1.1). Since these events locate at low z, the roundness-cut removed these gap events effectively (red points). The calculated rate is summarized in Table 4.3.4.

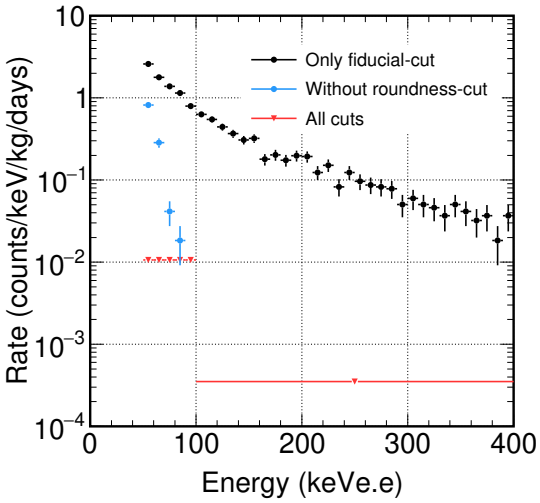

Figure 4.3.5: Expected spectra of the LAμ-PIC surface background. The black points are the expected rate in the fiducial volume. The blue points are the spectrum without roundness-cut. The red triangle points are upper limit with all cuts.

Table 4.3.4: Summary of the expected rate of the LAμ-PIC surface background. The values in brackets show errors (%).

Expected rate of the LAμ-PIC surface (counts/keV/kg/days) with error (%)			
	50-60 keV	60-100 keV	100-400 keV
Fiducial only	2.6 (24)	1.3 (13)	1.6×10^{-1} (6.8)
without Roundness-cut	8.2×10^{-1} (25)	8.6×10^{-2} (23)	$< 3.5 \times 10^{-4}$
All cuts	$< 1.1 \times 10^{-2}$	$< 2.6 \times 10^{-3}$	$< 3.5 \times 10^{-4}$

4.3.3 Summary of internal backgrounds

The total internal backgrounds are summarized in Table 4.3.5

Table 4.3.5: Summary of the expected rate of the total internal backgrounds. The values in brackets show errors (%).

Expected rate of the total internal background (counts/keV/kg/days) with error (%)			
	50-60 keV	60-100 keV	100-400 keV
Fiducial only	2.7 (23)	1.4 (12)	2.5×10^{-1} (4.4)
Without roundness-cut	9.2×10^{-1} (22)	1.8×10^{-1} (11)	5.2×10^{-2} (2.3)
All cuts	5.9×10^{-2} (12)	5.4×10^{-2} (6.0)	2.5×10^{-2} (3.1)

4.4 Summary of the background studies

Here we summarize the background simulations and discuss the main background source of the NEWAGE-0.3b" detector. In order to compare the measurement with the simulation, the results of expected rate obtained above sections are converted into the expected number of events by normalizing with the experimental livetime and the target mass in the fiducial volume. The predicted number of events in the energy region of 50-60 keV is summarized in Table 4.4.1. Results on the other energy regions are described in Figures 4.4.1 and 4.4.2. The measured number of events are in good agreement with predicted one within errors in both with and without roundness-cut. Especially, simulated spectrum without roundness-cut described in Figure 4.4.1 reproduced the shape of measured one.

The ^{222}Rn backgrounds was reduced by the gas circulation system with cooled charcoal and their contribution was found to be negligible. Ambient gamma-rays and ambient neutrons contribute some part of the backgrounds, and these backgrounds can be reduced with some shields. The important point is that the internal backgrounds of ^{220}Rn and the LAμ-PIC surface would remain and they would become dominant backgrounds. The material screening and replacing the detector components are needed.

Table 4.4.1: Summary of the predicted numbers of background events and measured numbers in the energy region of 50-60 keV.

Source	w/o roundness	w/ roundness
Ambient gamma-rays	4.6 ± 2.7	1.5 ± 1.5
Ambient neutrons	$(4.8 \pm 1.2) \times 10^{-1}$	$(3.5 \pm 0.9) \times 10^{-1}$
^{222}Rn	$(8.6 \pm 3.5) \times 10^{-2}$	$(5.3 \pm 2.2) \times 10^{-2}$
^{220}Rn	1.1 ± 0.1	$(6.1 \pm 0.7) \times 10^{-1}$
LAμ-PIC surface	9.1 ± 2.3	$< 1.2 \times 10^{-1}$
Total background	15 ± 3.5	2.5 ± 1.5
Measurement	12 ± 3.5	2.0 ± 1.4

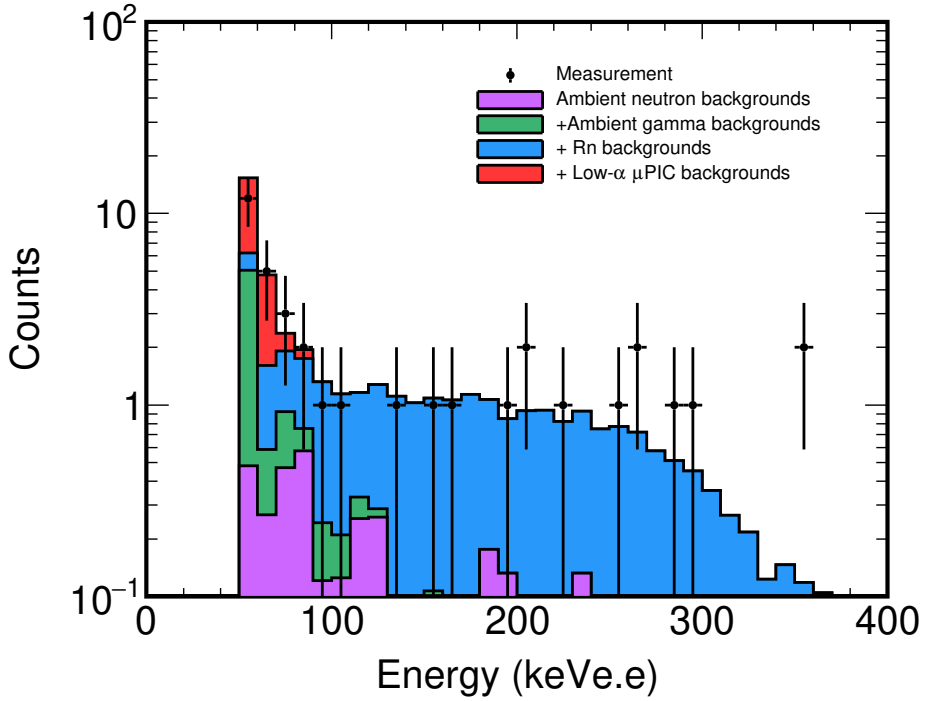

Figure 4.4.1: Predicted and measured spectra without roundness-cut. The violet histogram is contributed by the ambient neutrons. The green stacked histogram shows the ambient gamma-rays. The blue stacked histogram is contributed by the ^{222}Rn and ^{220}Rn backgrounds. The red stacked histogram is the LAμ-PIC surface backgrounds.

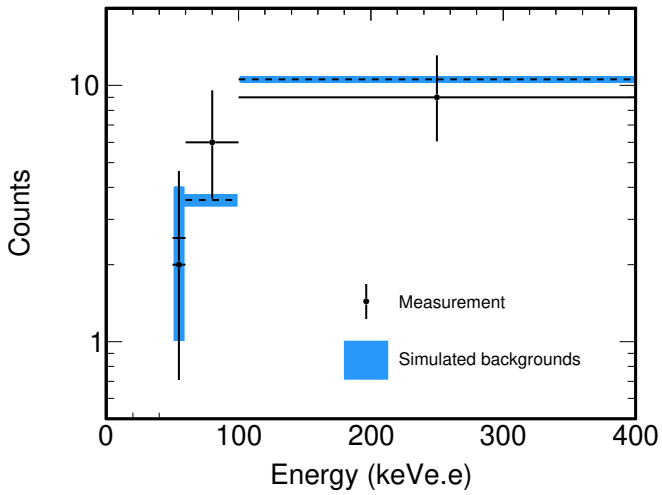

Figure 4.4.2: Measured number of events and expected one with roundness-cut in each energy-bin. The black dots are measurement data. The black dotted line and blue shaded area indicate expected numbers and errors, respectively.

4.5 Future prospects

Since several backgrounds prevented this work from the dark matter search of the DAMA region, a further background reduction is needed. In addition, the more statistics would help to claim the strong evidence of the dark matter. In this section, we estimate the rejection power of the isotropic background model when we use a large-size μ-TPC on the order of 1 m^3 and reduce the backgrounds.

The expected rate of the dark matter was calculated using the signal Monte Carlo simulation. The WIMP-proton cross section claimed by the DAMA experiment is about 3 pb for the 100 GeV dark matter mass according to Ref. [62]. The expected signal rate is known to be 0.20 counts/keV/kg/days in the energy region of 50-60 keV. In order to ensure one hundred of the signal-to-noise ratio, the background rate should be less than $O(10^{-3})$ counts/keV/kg/days.

Internal backgrounds are the radon background and the LAμ-PIC surface background. While these backgrounds have the rate of O(1) counts/keV/kg/days (see Table 4.3.5), they are known to locate at low z (around the LAμ-PIC and the GEM) and high z position (around the drift plate). Recently, a discovery of minority carriers in CS_2 + O_2 gas mixtures by the DRIFT group opened the potential of an absolute z coordinate measurement in self-triggering TPCs [90]. Moreover, an SF_6 negative ion gas which can be handled easily was found to retain the same advantage as the CS_2 + O_2 gas mixture [91]. The negative ion gas TPC enables to reduce these backgrounds using the z fiducialization.

External backgrounds are the ambient gamma-rays and neutrons. These backgrounds can be reduced by the external shields comprising of materials like lead (Pb) and water (H_2O). We estimated the background rate penetrating a water shield by using the Geant4 simulation (Figures 4.5.1 and 4.5.2). Since the water of 150 cm in thickness reduce

by two order of magnitude, the background rate of the ambient gamma-rays reaches O(10^{-3}) counts/keV/kg/days assuming the same gamma rejection power of NEWAGE-0.3b". It should be noted that this estimation was performed with a very simple geometry and the actual gamma-ray rate might be higher than this result due to the back-scatterings into the gas volume. In addition, the neutron flux would be reduced by one order of magnitude using water of 10 cm. Therefore the water of more than 150 cm such as a big cylindrical water tank, surrounding the μTPC , will acts as a passive shielding against these external backgrounds.

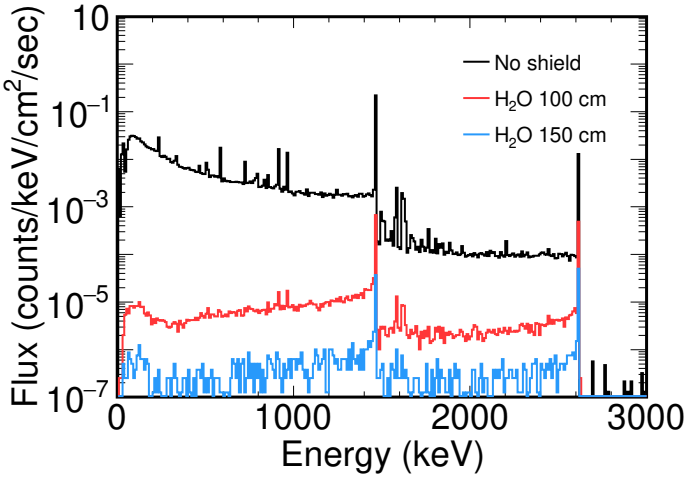

Figure 4.5.1: Energy spectra of ambient gamma-rays penetrating a H_2O shielding. The black, red, blue lines show the case for no shielding, 100 cm of Pb and 150 cm of Pb, respectively.

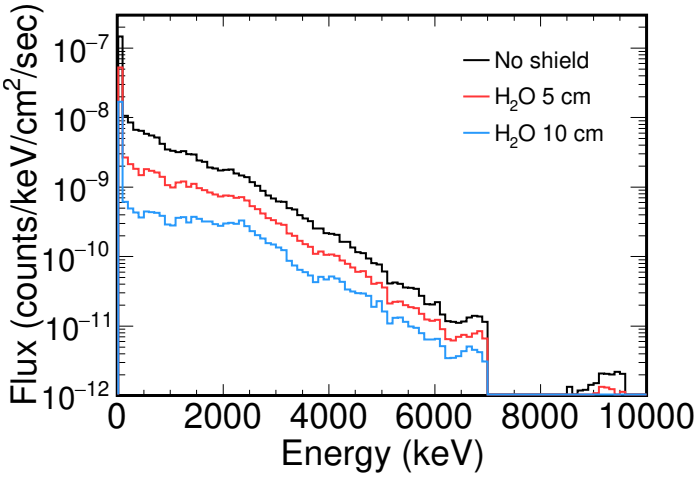

Figure 4.5.2: Energy spectra of ambient neutrons penetrating a H_2O shielding. The black, red, blue lines show the case for no shielding, 5 cm of H_2O and 10 cm of H_2O, respectively.

The p-value for rejecting the hypothesis of the isotropic background model was calculated by using a same procedure as described in Section 3.4. Here we assumed a large-size detector on the order of 1 m^3 whose specifications are summarized in Table 4.5.1. Eighteen modules of the μTPC, each with 28×28 cm^2 of the fiducial area and 44 cm of the drift length, constituted the fiducial volume of 620 L. The dark matter signal counts were expected to be about 60 in the energy region of 50-60 keV with one year's observation. Expected p-values with various angular resolutions are shown in Figure 4.5.3. It suggests that the angular resolution better than 30 degree is needed in order to reject the isotropic background model with 90% confidence level. The main cause of the deterioration of the angular resolution in the large size detector is the diffusion effect during the electron drift. However the negative ion gas TPC has a very small diffusion thanks to the negative ion drift. Considering both aspects of the background reduction and the angular resolution, the negative ion gas TPC is appropriate for the directional dark matter search in DAMA region.

Table 4.5.1: Specifications of the large size detector.

Gas medium	SF_6
Fiducial volume	620 L ($28 \times 28 \times 44$ $cm^3 \times 18$)
Pressure	20 Torr (0.026 bar)
Target mass	79 g

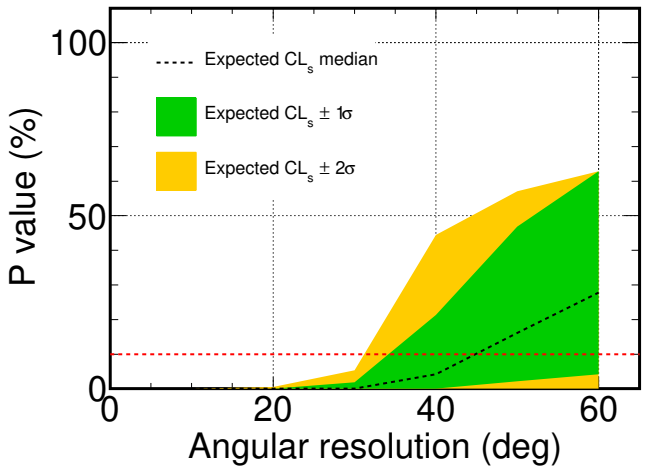

Figure 4.5.3: P-value for the rejection of the isotropic background model with various angular resolutions. The black dotted line shows the median. The green and yellow area shows $\pm 1\sigma$ and $\pm 2\sigma$, respectively.

Chapter 5

Conclusion

We developed a low background μTPC detector, NEWAGE-0.3b", for the directional dark matter search. An LAμ-PIC which is a two-dimensional tracking gaseous detector made of low radioactive materials was installed in NEWAGE-0.3b" detector in 2017. A directional dark matter search in Kamioka underground laboratory was carried out from June 2018 to November 2018. Total exposure was 1.1 kg·days and the observed events in the energy region of 50-60 keV was two. A directional analysis was performed and the significance of a WIMP signal was insufficient to claim a discovery. Therefore we derived exclusion limits on the Spin-Dependent WIMP-proton cross section with a minimum of 50 pb for 100 GeV/c^2 WIMPs at 90% confidence level. This result improved the sensitivity by about 15 times compared to the previous result and marked the best direction-sensitive limit.

Appendix A

Environment variables

In order to ensure the measurement stability, several detector-status and environment variables were monitored during the data-taking. The values are summarized in Table A.1 and the time variations are shown in Figure A.1-A.7. Although the LAμ-PIC voltage, current and the drift voltage have several spike values, these are attributed to the maintenance work of the detector. The data in that time was not be used in the dark matter search. Since the vacuum vessel had a leak, the gas pressure increased. The pressure increase rate of RUN22-1 and RUN22-2 were 0.12 Torr/days and 0.25 Torr/days, respectively.

Table A.1: Summary of the detector-status and environment variable values. The fluctuation of the gas pressure is defined by the difference of the maximum and minimum pressure. Others are defined by the standard deviation.

Parameter	Value	Fluctuation (%)	Figure
Anode voltage	470 V	< 1	A.1
Anode current	4 nA	4	A.1
Drift voltage	4.1 kV	< 1	A.2
Drift current	22 μA	3	A.2
Gas pressure	76 Torr	+15 −2	A.3
Gas-flow rate	1100 mL/min	3	A.4
Coolant temperature	230 K	< 1	A.5
Detector temperature	34 °C	2	A.6
Room temperature	34 °C	2	A.7

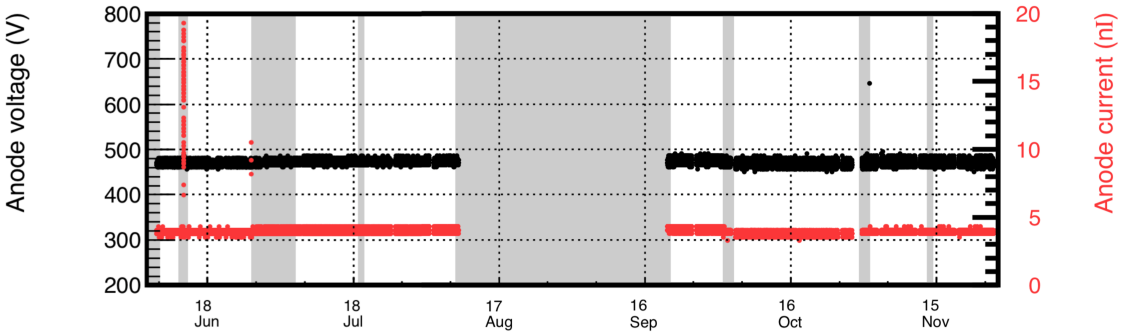

Figure A.1: Time variation of the LAμ-PIC anode voltage in RUN22. The gray area show the term of maintenance work or the calibration.

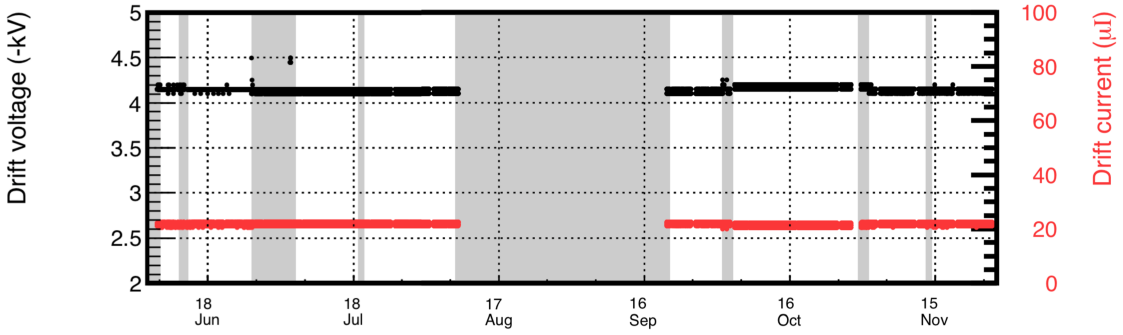

Figure A.2: Time variation of the drift voltage in RUN22. The gray area show the term of maintenance work or the calibration.

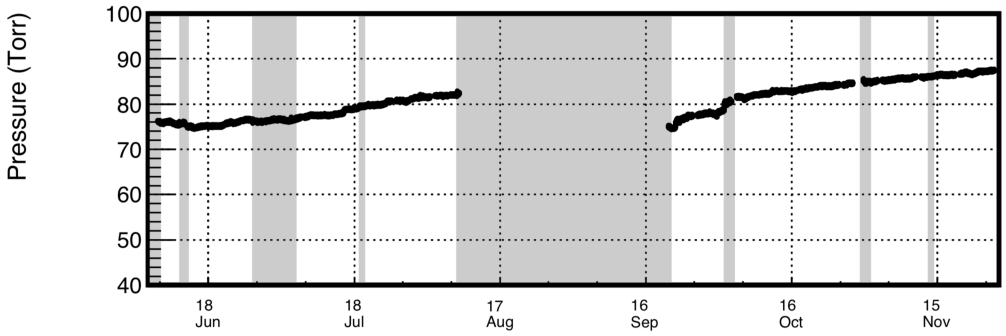

Figure A.3: Time variation of the gas pressure in RUN22. The gray area show the term of maintenance work or the calibration.

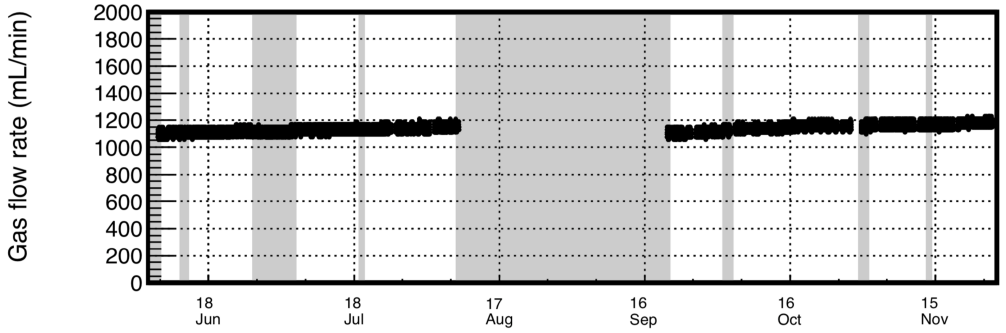

Figure A.4: Time variation of the gas-flow rate in RUN22. The gray area show the term of maintenance work or the calibration.

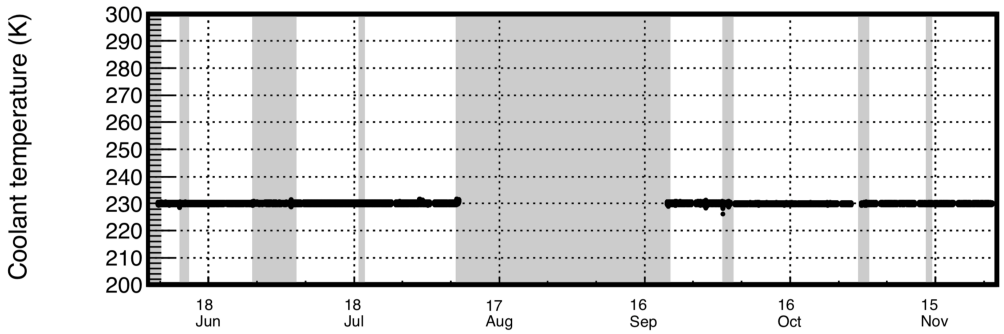

Figure A.5: Time variation of the coolant temperature in RUN22. The gray area show the term of maintenance work or the calibration.

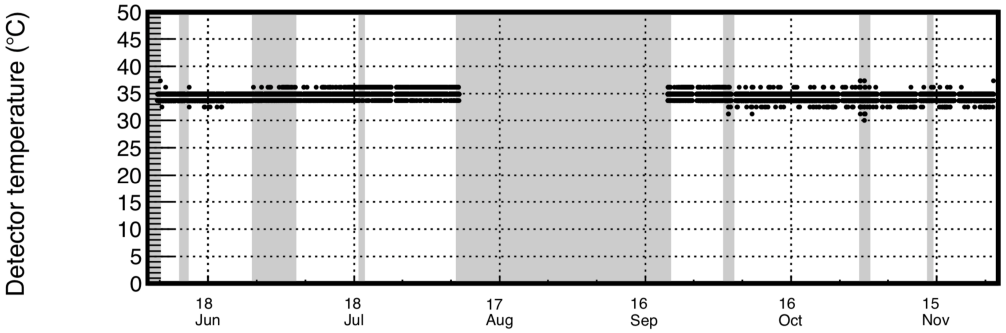

Figure A.6: Time variation of the detector temperature in RUN22. The gray area show the term of maintenance work or the calibration.

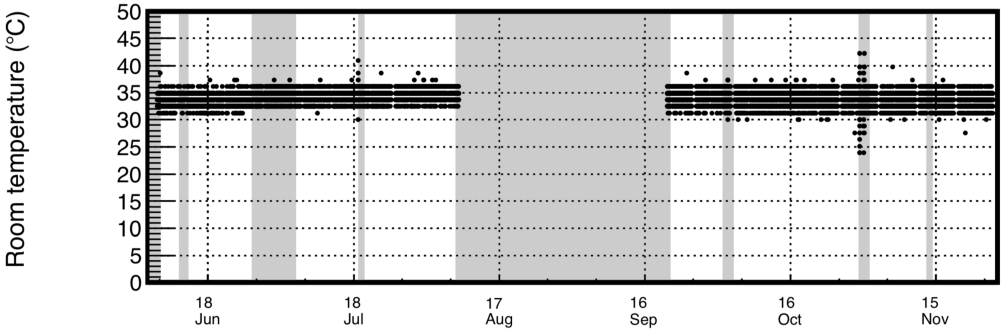

Figure A.7: Time variation of the room temperature in RUN22. The gray area show the term of maintenance work or the calibration.

Acknowledgements

博士論文を執筆するにあたって、また博士過程での研究生活において、お世話になった皆様に感謝を申し上げます。

指導教員である身内賢太朗先生からは非常に多くのことを学ばせていただきました。研究会などの議論の場での、精確で想像に逸する発言にいつも感銘を受けております。この 5 年間の研究生活で、モチベーションが下がることなく真摯に物理学と向き合えることができたのは、身内先生が作ってくださった NEWAGE という環境が刺激的であったからです。NEWAGE グループには常に新鮮な風が吹いていると感じてきました。心から感謝いたします。

NEWAGE グループの皆様に感謝いたします。中村輝石様、矢ケ部様、橋本様は同グループの先輩として指導していただきました。帝釋様、石浦様は切磋琢磨した同期です。中澤様、中村拓馬様、島田様は研究熱心な後輩であり、私が先輩でありながら助けられたことも多々ありました。東大の関谷先生には神岡の検出器の管理をしてくださっています。越智先生には検出器に関して技術指導をしていただき、また私の初めての国際会議でも大変お世話になったことを覚えております。

神岡研究所の小林先生、市村先生、安部先生、伊藤氏、DNP の本村様には次期検出器の製作の件でお世話になりました。KEK の坂下先生、岸下先生、庄司先生、田中先生には回路開発に関して多くのことを学ばせていただきました。早稲田大学の寄田先生、田中先生、木村様にはフィードスルーの製作で指導していただきました。神戸大学宇宙論研究室の早田先生、伊藤飛鳥氏、慶応大の鹿野先生、東大先端研の Dany 氏にはアクシオンに関する研究でお世話になっております。伊藤飛鳥氏はプライベートにおいてもお世話になりました。僕の名前をこれからは間違えないようお願いします。

神戸粒子物理研究室の皆様に感謝いたします。蔵重先生、山崎先生にはコロキウムで多くを学ばせていただきました。竹内先生、ラドン計を貸してくださっております。不注意で壊してしまい、その節は誠に申し訳ありませんでした。鈴木先生、実験室のスペースをお借りしております。中野先生には神戸でも神岡でも気を使っていただいてよく飲みに誘っていただきました。前田先生の奥さんはとても美人です。また事務室の横山様、吉田様には出張手続き等いつもお世話になっております。

この紙面上には書ききれないほどの研究者の方々にお会いしてきました。最後に再度お世話になった皆様に感謝を申し上げます。

Bibliography

[1] F. Zwicky, ApJ **86**, 217 (1937).

[2] V. C. Rubin, W. K. Ford Jr., and N. Thonnard, ApJ **238**, 471 (1980).

[3] V. C. Rubin, W. K. Ford Jr., and N. Thonnard, ApJ **225**, L107 (1978).

[4] A. Refregier, Annual Review of Astronomy and Astrophysics **41**, 645 (2003).

[5] R. Massey, J. Rhodes, R. Ellis, *et al.*, Nature **445**, 286 (2007).

[6] D. Clowe, M. Bradač, *et al.*, ApJ **648**, L109 (2006).

[7] C. L. Bennett, A. J. Banday, K. M. Górski, G. Hinshaw, P. Jackson, P. Keegstra, A. Kogut, G. F. Smoot, D. T. Wilkinson, and E. L. Wright, The Astrophysical Journal **464**, L1 (1996).

[8] C. L. Bennett, M. Halpern, G. Hinshaw, *et al.*, The Astrophysical Journal Supplement Series **148**, 1 (2003).

[9] Planck Collaboration, N. Aghanim, Y. Akrami, *et al.*, arXiv e-prints (2018), arXiv:1807.06209 [astro-ph.CO] .

[10] V. Springel, S. D. M. White, *et al.*, Nature **435**, 629 (2005).

[11] C. Alcock, R. A. Allsman, D. Alves, *et al.*, ApJ **471**, 774 (1996).

[12] L. Wyrzykowski, J. Skowron, S. Kozłowski, *et al.*, Monthly Notices of the Royal Astronomical Society **416**, 2949 (2011).

[13] P. Tisserand, L. Le Guillou, Afonso, *et al.*, A&A **469**, 387 (2007).

[14] S. W. Randall, M. Markevitch, D. Clowe, *et al.*, The Astrophysical Journal **679**, 1173 (2008).

[15] M. Bradac, S. W. Allen, *et al.*, The Astrophysical Journal **687**, 959 (2008).

[16] G. Jungman, M. Kamionkowski, and K. Griest, Physics Reports **267**, 195 (1996).

[17] R. D. Peccei and H. R. Quinn, Phys. Rev. Lett. **38**, 1440 (1977).

[18] A. Burrows, M. T. Ressell, and M. S. Turner, Phys. Rev. D **42**, 3297 (1990).

[19] D. A. Dicus, E. W. Kolb, V. L. Teplitz, and R. V. Wagoner, Phys. Rev. D **22**, 839 (1980).

[20] D. A. Dicus, E. W. Kolb, V. L. Teplitz, and R. V. Wagoner, Phys. Rev. D **18**, 1829 (1978).

[21] Y. Fukuda, T. Hayakawa, E. Ichihara, *et al.* (Super-Kamiokande Collaboration), Phys. Rev. Lett. **81**, 1562 (1998).

[22] A. Merle, International Journal of Modern Physics D **22**, 1330020 (2013).

[23] J. Lewin and P. Smith, Astroparticle Physics **6**, 87 (1996).

[24] P. Gondolo, Phys. Rev. D **66**, 103513 (2002).

[25] J. Bovy, C. A. Prieto, T. C. Beers, *et al.*, The Astrophysical Journal **759**, 131 (2012).

[26] P. J. McMillan and J. J. Binney, MNRAS **402**, 934 (2010).

[27] Piffl, T., Scannapieco, C., Binney, J., *et al.*, A&A **562**, A91 (2014).

[28] R. Catena and P. Ullio, Journal of Cosmology and Astroparticle Physics **2010**, 004 (2010).

[29] Weber, M. and de Boer, W., A&A **509**, A25 (2010).

[30] M. Pato, F. Iocco, and G. Bertone, Journal of Cosmology and Astroparticle Physics **2015**, 001 (2015).

[31] F. Nesti and P. Salucci, Journal of Cosmology and Astroparticle Physics **2013**, 016 (2013).

[32] P. Gondolo, Phys. Rev. D **66**, 103513 (2002).

[33] J. Ellis, A. Ferstl, and K. A. Olive, Physics Letters B **481**, 304 (2000).

[34] R. H. Helm, Phys. Rev. **104**, 1466 (1956).

[35] G. Co, V. D. Donno, M. Anguiano, and A. Lallena, **2012**, 010 (2012).

[36] D. N. Spergel, Phys. Rev. D **37**, 1353 (1988).

[37] G. Adhikari, P. Adhikari, E. B. de Souza, *et al.* (COSINE-100 Collaboration), Phys. Rev. Lett. **123**, 031302 (2019).

[38] K. Fushimi, H. Ejiri, R. Hazama, and otehrs, Journal of Physics: Conference Series **718**, 042022 (2016).

[39] E. Shields, J. Xu, and F. Calaprice, Physics Procedia **61**, 169 (2015), 13th International Conference on Topics in Astroparticle and Underground Physics, TAUP 2013.

[40] J. Amaré, S. Cebrián, I. Coarasa, *et al.*, Phys. Rev. Lett. **123**, 031301 (2019).

[41] J. Amaré, S. Cebrián, D. Cintas, I. Coarasa, E. García, M. Martínez, M. A. Oliván, Y. Ortigoza, A. Ortiz de Solórzano, J. Puimedón, A. Salinas, M. L. Sarsa, and P. Villar, arXiv e-prints (2019), arXiv:1910.13365 [astro-ph.IM] .

[42] R. Bernabei *et al.*, Nucl. Phys. At. Energy **19**, 307 (2018).

[43] R. Agnese, T. Aralis, T. Aramaki, *et al.*, Phys. Rev. Lett. **121**, 051301 (2018).

[44] R. Agnese, A. J. Anderson, T. Aramaki, *et al.* (SuperCDMS Collaboration), Phys. Rev. Lett. **116**, 071301 (2016).

[45] C. E. Aalseth, P. S. Barbeau, J. Colaresi, *et al.* (CoGeNT Collaboration), Phys. Rev. D **88**, 012002 (2013).

[46] L. Hehn *et al.*, The European Physical Journal C **76**, 548 (2016).

[47] A. H. Abdelhameed, G. Angloher, P. Bauer, *et al.* (CRESST Collaboration), arXiv e-prints (2019), arXiv:1904.00498 [astro-ph.CO] .

[48] P. A. Amaudruz, M. Baldwin, M. Batygov, *et al.* (DEAP-3600 Collaboration), Phys. Rev. Lett. **121**, 071801 (2018).

[49] P. Agnes, I. F. M. Albuquerque, T. Alexander, *et al.* (DarkSide Collaboration), Phys. Rev. Lett. **121**, 081307 (2018).

[50] K. Abe, K. Hiraide, K. Ichimura, *et al.*, Physics Letters B **759**, 272 (2016).

[51] E. Aprile, J. Aalbers, F. Agostini, *et al.* (XENON Collaboration), Phys. Rev. Lett. **121**, 111302 (2018).

[52] D. S. Akerib, S. Alsum, *et al.* (LUX Collaboration), Phys. Rev. Lett. **118**, 021303 (2017).

[53] X. Cui, A. Abdukerim, W. Chen, *et al.* (PandaX-II Collaboration), Phys. Rev. Lett. **119**, 181302 (2017).

[54] M. Szydagis, for the LUX Collaboration, and the LZ Collaboration, arXiv e-prints (2016).

[55] C. Amole, M. Ardid, I. J. Arnquist, *et al.* (PICO Collaboration), Phys. Rev. Lett. **118**, 251301 (2017).

[56] D. S. Akerib, S. Alsum, H. M. Araújo, *et al.* (LUX Collaboration), Phys. Rev. Lett. **118**, 251302 (2017).

[57] J. Xia, A. Abdukerim, W. Chen, *et al.*, Physics Letters B **792**, 193 (2019).

[58] E. Aprile, J. Aalbers, F. Agostini, *et al.* (XENON Collaboration), Phys. Rev. Lett. **122**, 141301 (2019).

[59] R. Agnese, A. J. Anderson, T. Aralis, *et al.* (SuperCDMS Collaboration), Phys. Rev. D **97**, 022002 (2018).

[60] K. Choi, K. Abe, Y. Haga, *et al.* (Super-Kamiokande Collaboration), Phys. Rev. Lett. **114**, 141301 (2015).

[61] M. G. Aartsen *et al.*, The European Physical Journal C **77**, 146 (2017).

[62] C. Savage, P. Gondolo, and K. Freese, Phys. Rev. D **70**, 123513 (2004).

[63] J. Battat *et al.*, Astroparticle Physics **91**, 65 (2017).

[64] G. Charpak *et al.*, Nuclear Instruments and Methods in Physics Research Section A: Accelerators, Spectrometers, Detectors and Associated Equipment **478**, 26 (2002), proceedings of the ninth Int.Conf. on Instrumentation.

[65] D. Santos *et al.*, Journal of Physics: Conference Series **469**, 012002 (2013).

[66] Y. Tao *et al.*, arXiv e-prints (2019), arXiv:1903.02159 [physics.ins-det] .

[67] S. Ahlen, J. Battat, *et al.*, Physics Letters B **695**, 124 (2011).

[68] N. D. Marco *et al.*, Journal of Physics: Conference Series **1056**, 012018 (2018).

[69] K. Nakamura, K. Miuch, *et al.*, Progress of Theoretical and Experimental Physics **043F01** (2015).

[70] K. Miuchi, K. Hattori, S. Kabuki, *et al.*, Physics Letters B **654**, 58 (2007).

[71] T. Hashimoto, Doctor Thesis, Kobe University (2018).

[72] K. Nakamura, Doctor Thesis, Kyoto University (2014).

[73] Takada A *et al.*, Nuclear Instruments and Methods in Physics Research Section A: Accelerators, Spectrometers, Detectors and Associated Equipment **573**, 195 (2007).

[74] F. Sauli, Nuclear Instruments and Methods in Physics Research Section A: Accelerators, Spectrometers, Detectors and Associated Equipment **805**, 2 (2016), special Issue in memory of Glenn F. Knoll.

[75] S. Biagi, Nuclear Instruments and Methods in Physics Research Section A: Accelerators, Spectrometers, Detectors and Associated Equipment **283**, 716 (1989).

[76] J. F. Ziegler, M. Ziegler, and J. Biersack, Nuclear Instruments and Methods in Physics Research Section B: Beam Interactions with Materials and Atoms **268**, 1818 (2010), 19th International Conference on Ion Beam Analysis.

[77] G. F. Reinking, L. G. Christophorou, and S. R. Hunter, Journal of Applied Physics **60**, 499 (1986).

[78] O. Sasaki and M. Yoshida, 1998 IEEE Nuclear Science Symposium and Medical Imaging Conference **1**, 440 (1998).

[79] G. J. Feldman and R. D. Cousins, Phys. Rev. D **57**, 3873 (1998).

[80] J. Conrad, O. Botner, A. Hallgren, and otehrs, Phys. Rev. D **67**, 012002 (2003).

[81] G. L. Fogli, E. Lisi, A. Marrone, *et al.*, Phys. Rev. D **66**, 053010 (2002).

[82] S. Fukuda, Y. Fukuda, T. Hayakawa, *et al.*, Nuclear Instruments and Methods in Physics Research Section A: Accelerators, Spectrometers, Detectors and Associated Equipment **501**, 418 (2003).

[83] H. Nishimura, Doctor Thesis, Kyoto University (2009).

[84] R. P. D. B. 11th Edition Japan Radioisotope Association(JRIA), .

[85] K. Mizukoshi, R. Taishaku, K. Hosokawa, K. Kobayashi, K. Miuchi, T. Naka, A. Takeda, M. Tanaka, Y. Wada, K. Yorita, and S. Yoshida, Progress of Theoretical and Experimental Physics **2018** (2018), 10.1093/ptep/pty133, 123C01.

[86] H. Nishimura, K. Miuchi, K. Hattori, S. Iwaki, C. Ida, S. Kabuki, H. Kubo, S. Kurosawa, H. Sekiya, A. Takada, M. Takahashi, A. Takeda, T. Tanimori, K. Tsuchiya, and K. Ueno, Astroparticle Physics **31**, 185 (2009).

[87] M. Z. Nakib, J. Cooley, V. E. Guiseppe, *et al.*, AIP Conference Proceedings **1549**, 78 (2013).

[88] K. Abe, K. Hiraide, K. Ichimura, *et al.*, Nuclear Instruments and Methods in Physics Research Section A: Accelerators, Spectrometers, Detectors and Associated Equipment **884**, 157 (2018).

[89] N. Smith, J. Lewin, and P. Smith, Physics Letters B **485**, 9 (2000).

[90] J. Battat *et al.*, Physics of the Dark Universe **9-10**, 1 (2015).

[91] N. Phan, R. Lafler, R. Lauer, E. Lee, D. Loomba, J. Matthews, and E. Miller, J. Instrum. **12**, P02012 (2017).